THESIS FOR THE DEGREE OF DOCTOR OF PHILOSOPHY

Solid-Supported Gold Nanorods for Antibacterial Applications

MAJA LIDSTRÖM UUSITALO

Department of Chemistry and Chemical Engineering

CHALMERS UNIVERSITY OF TECHNOLOGY

Gothenburg, Sweden 2025

Solid-Supported Gold Nanorods for Antibacterial Applications
MAJA LIDSTRÖM UUSITALO
ISBN 978-91-8103-325-0

© MAJA LIDSTRÖM UUSITALO, 2025.

Doktorsavhandlingar vid Chalmers tekniska högskola
Ny serie nr 5782
ISSN 0346-718X
https://doi.org/10.63959/chalmers.dt/5782

Department of Chemistry and Chemical Engineering
Chalmers University of Technology
SE-412 96 Gothenburg
Sweden
Telephone + 46 (0)31-772 1000

Cover: An illustration visualising solid-supported gold nanorods under illumination with near-infrared light.

Chalmers Digitaltryck
Gothenburg, Sweden 2025

Solid-Supported Gold Nanorods for Antibacterial Applications

MAJA LIDSTRÖM UUSITALO
Department of Chemistry and Chemical Engineering
Chalmers University of Technology

Abstract

Biomaterials are essential in modern medicine, ensuring the quality of life of the individual by providing functions for diagnostic, therapeutic, and prosthetic purposes. However, when the surface of a biomaterial is colonised by bacteria, hard-to-treat infections can arise. The severity of biomaterial-associated infections (BAIs) stems from the ability of biofilm-growing bacteria to evade our bodies' immune response and their high tolerance to antibiotics. The increasing incidence of antimicrobial resistant bacteria and the insufficient development rate of new antimicrobial agents are further limiting the options available for combatting these infections. In response to the pressing need for new approaches to combat BAIs, the development of antibacterial modification strategies for biomaterials has emerged as a promising alternative. This thesis explores materials based on solid-supported gold nanorods and their application as an antibacterial modification strategy utilising the nanoparticles' photothermal heating. Material preparation protocols were developed for the surface-attachment of gold nanorods on glass and titanium, as well as for the preparation of gold nanorod gradient surfaces. The photothermal properties of the solid-supported gold nanorods were studied as a function of near-infrared (NIR) light intensity and nanoparticle surface coverage. An *in vitro* method for studying the antibacterial activity of the solid-supported gold nanorods under NIR irradiation was developed. The antibacterial activity evaluation was focused on the influence of the support material, the dependency on the NIR light intensity, and the effect in combination with an antimicrobial peptide (AMP).

The material preparation protocols facilitated surface-attachment of gold nanorods in a well-dispersed manner, with retained plasmon resonance characteristics on glass. By monitoring the lattice thermal expansion of the solid-supported gold nanorods with *in situ* X-ray diffraction, and supporting the findings with Vis-NIR spectroscopy and electron microscopy characterisation, a relationship between the NIR light intensity, the gold nanorod temperature, and the onset of heating-induced morphology transformations was established. Furthermore, studying the gold nanorod gradient surfaces provided insight into how the optical and photothermal properties were affected by the nanoparticle surface coverage. The antibacterial activity of the solid-supported gold nanorods was influenced by the support material, and on glass, a NIR light intensity dependent bactericidal effect caused by the photothermal heating of the nanorods was attained. Additionally, an enhanced antibacterial efficacy was demonstrated when combining the solid-supported gold nanorods with an AMP. The findings of this thesis elucidate the characteristics of solid-supported gold nanorods, highlight ways of tuning their properties, and show the potential of using these materials for antibacterial applications.

Keywords: gold nanorods, thermoplasmonics, photothermal therapy, biomaterial-associated infections

List of publications

I. **Photothermal Properties of Solid-Supported Gold Nanorods**
Maja Uusitalo[‡], Michal Strach[‡], Gustav Eriksson, Tetiana Dmytrenko, John Andersson, Andreas Dahlin, Mats Hulander, and Martin Andersson
Nano Letters. 2024, 24 (40), 12529–12535.

II. **Gold Nanorod Gradient Surfaces**
Maja Lidström Uusitalo, Michal Strach, Mats Hulander, and Martin Andersson
Submitted for publication.

III. **Gold Nanorods as Photothermal Antibacterial Materials**
Maja Uusitalo, Gustav Eriksson, Mats Hulander, and Martin Andersson
ACS Applied Nano Materials. 2025, 8 (7), 3661–3671.

IV. **Antibacterial Activity of Solid-Supported Gold Nanorods Combined with Antimicrobial Peptides**
Maja Lidström Uusitalo, Alva Nilsson, Ann-Britt Schäfer, Gustav Eriksson, Mats Hulander, Michaela Wenzel, and Martin Andersson
Manuscript.

[‡] The authors contributed equally to this work

My contribution to the publications

I. Shared main author. Responsible for synthesis, sample preparation, sample characterisation (Vis-NIR spectroscopy, SEM), and modelling. Co-wrote the first draft of the manuscript.

II. Main author. Responsible for all experimental work and characterisation except XRD studies. Responsible for modelling and most data analysis. Wrote the first draft of the manuscript.

III. Main author. Responsible for all experimental work and characterisation except TEM and XPS. Responsible for data analysis and wrote the first draft of the manuscript.

IV. Main author. Responsible for sample preparation and characterisation (Vis-NIR spectroscopy, SEM, thermal imaging). Supervised and participated in the *in vitro* antibacterial activity studies. Co-wrote the first draft of the manuscript.

Abbreviations

3-MPS	(3-Mercaptopropyl)trimethoxysilane
AMP	Antimicrobial peptide
AuNR	Gold nanorod
BAI	Biomaterial-associated infection
BCP	Bacterial cytological profiling
CFU	Colony forming unit
CTAB	Hexadecyltrimethylammonium bromide
Glass-AuNR	Gold nanorods supported on glass
LSPR	Localised surface plasmon resonance
MoA	Mode of action
NIR	Near-infrared
PBS	Phosphate-buffered saline
PPTT	Plasmonic photothermal therapy
PTT	Photothermal therapy
SEM	Scanning electron microscopy
TEM	Transmission electron microscopy
Ti-AuNR	Gold nanorods supported on titanium
TSB	Trypic soy broth
Vis-NIR	Visible-near-infrared
XPS	X-ray photoelectron spectroscopy
XRD	X-ray diffraction

Table of contents

Abstract I
List of publications III
1. Introduction 1
1.1 Purpose and objectives 2
2. Background 5
2.1 Gold nanoparticles for biomedical applications 5
2.1.1 Size and shape control 7
2.1.2 Solid-supported gold nanoparticles 8
2.1.2.1 Factors influencing the properties 8
2.1.2.2 Gold nanoparticle gradient surfaces 9
2.1.3 Nanothermometry of gold nanoparticles 9
2.1.4 Plasmonic photothermal therapy 10
2.2 Antibacterial modifications of biomaterials 11
2.2.1 Overview of modification strategies 12
2.2.2 Multifunctional strategies 12
2.3 Bacterial cytological profiling 14
3. Methodology 15
3.1 Material preparation 15
3.1.1 Gold nanorod synthesis 15
3.1.2 Surface-attachment of gold nanorods 16
3.1.3 Gold nanorod gradient surfaces 17
3.2 Material characterisation 18
3.2.1 Electrophoretic light scattering 18
3.2.2 Transmission electron microscopy 18
3.2.3 Scanning electron microscopy 19
3.2.4 Vis-NIR spectroscopy 20
3.2.5 X-ray photoelectron spectroscopy 20
3.2.6 Thermal imaging 20
3.2.7 Optical microscopy 21
3.3 Modelling heating of plasmonic nanoparticle arrays 21
3.4 *In situ* X-ray diffraction 22
3.4.1 Furnace heating and texture analysis 23
3.4.2 Near-infrared laser heating 23
3.5 *In vitro* antibacterial activity 25
3.6 Bacterial cytological profiling 26
4. Results and discussion 27

4.1 Material characterisation 27
4.1.1 Gold nanorods 27
4.1.2 Solid-supported gold nanorods 29
4.1.3 Gold nanorod gradient surfaces 31
4.2 Evaluation of photothermal properties 34
4.2.1 Thermal imaging 34
4.2.2 *In situ* X-ray diffraction 36
4.2.2.1 Furnace heating and texture analysis 36
4.2.2.2 Near-infrared laser heating 38
4.3 *In vitro* antibacterial activity 43
4.3.1 Antibacterial activity in combination with an antimicrobial peptide 46
4.3.2 Solid-supported gold nanorod – bacteria interaction 47
4.4 Bacterial cytological profiling 49
5. Concluding remarks 53
5.1 Future perspectives 54
Acknowledgements 56
References 57

1. Introduction

The human body has a remarkable ability to maintain its function and recover from various injuries and illnesses. However, every now and then, our bodies' innate abilities are not enough, and we need assistance in maintaining or recovering our well-being. Over the last decades, advancements within medicine have provided us with treatment strategies for physical injuries and illnesses that formerly were inconceivable. A substantial part of the advancements can be attributed to the development and use of biomaterials. A biomaterial is defined as "a material designed to take a form that can direct, through interactions with living systems, the course of any therapeutic or diagnostic procedure".[1] In other words, they are materials that are used to replace, repair, or augment any tissue, organ or biological function, with the purpose of maintaining or improving the quality of life of the individual. The use of biomaterials thus covers a range of applications, including joint prosthesis, urinary catheters, and dental implants.

The global life expectancy is currently increasing, owing to several contributing factors including improved living standards and better access to healthcare,[2] and we are faced with an ageing population wherein chronic diseases pose a significant problem.[3] These demographic changes, along with technological advancements, have resulted in a predicted increase in the demand for biomaterials over the upcoming decades.[4–6] The importance of biomaterials for ensuring our quality of life can therefore not be understated. Still, the practical implementation of biomaterials is accompanied by certain challenges, with the most prominent complication being biomaterial-associated infections (BAIs). The surface of a biomaterial serves as a potentially suitable environment for bacterial colonisation, and when adhered bacteria proliferate and eventually form a biofilm, this results in hard-to-treat infections with severe clinical consequences. The severity of BAIs originates from the ability of biofilm-growing bacteria to evade the immune response and their high tolerance to conventional antibacterial agents like antibiotics.[7] The current strategies for combatting these infections include systemic administration of antibiotics and, depending on the severity of the infection as well as the placement of the biomaterial, surgical debridement and removal of the implanted material.

With an increasing occurrence of antimicrobial resistant bacteria and an insufficient development rate of new effective antibacterial agents to target them,[8–10] our options for prevention and treatment of BAIs are becoming restricted. We are hence faced with a growing demand for biomaterials to ensure the quality of life of the ageing population, and at the same time, our options for fighting the infections associated with these materials are becoming limited. To address this challenge, we need alternative strategies for combatting BAIs. One potential alternative is the development of antibacterial modification strategies, which provide the biomaterial itself with antibacterial properties. This can be achieved by making anti-adhesive surfaces that prevent initial bacterial colonisation, or by creating drug-eluting or contact-killing surfaces which actively eradicate bacteria.[11]

The unique properties of nanomaterials have been of great importance in the development of antibacterial modifications of biomaterials. For example, the introduction of nanotopography on a material surface can prevent bacterial adhesion, or even induce cell death by damaging the bacterial cell envelope. Out of the different nanomaterials that have been studied for this purpose, nanoparticles constitute one of the classes which have garnered most attention. There is a range of nanoparticles made from metals, metal oxides, carbon or polymers that exhibit inherent antibacterial activity or can function as delivery systems for antibacterial agents.[11,12] Additionally, certain nanoparticles exhibit photoinduced antibacterial activity, like plasmonic metal nanoparticles (gold, silver, platinum) where their light-induced heating can be used to thermally damage bacterial cells. To harness the functionality of nanoparticles in the development of antibacterial biomaterials, they can either be dispersed throughout the bulk of the material, or be supported on the material surface.

In this thesis, materials based on solid-supported gold nanorods are explored, aiming to address the challenge of combatting BAIs through an antibacterial modification strategy utilising near-infrared (NIR) light-induced heating of gold nanorods. By studying how the photothermal properties of these materials are influenced by light intensity and nanoparticle surface coverage, this research gives an understanding of the materials' behaviour essential for their practical implementation. The thesis also explores the antibacterial activity of the solid-supported gold nanorods, studying how it is affected by the support material and the NIR light intensity, as well as the combined effect with an antimicrobial peptide.

1.1 Purpose and objectives

The overall purpose of this thesis was to develop and characterise materials based on solid-supported gold nanorods and to explore how their photothermal properties can be utilised for antibacterial applications, aiming to address the challenge of combatting biomaterial-associated infections. For this purpose, the objectives of the thesis were divided into three main parts: (i) developing reproducible and tuneable material preparation protocols for solid-supported gold nanorods and characterising the prepared materials' properties, (ii) evaluating the photothermal properties of the solid-supported gold nanorods, and (iii) assessing the antibacterial activity of the materials upon excitation with NIR (808 nm) light. To address the objectives, four studies were conducted on which this thesis is based.

- In **Paper I**, the objective was to evaluate the photothermal properties of solid-supported gold nanorods on glass with *in situ* X-ray diffraction, to establish a relationship between the temperature of the nanoparticles and the NIR light intensity. This work also investigated heating-induced morphological transformations of the gold nanorods.
- In **Paper II**, the objective was to develop a method for the preparation of gold nanorod gradient surfaces, which served as a platform to study how the optical and photothermal properties of the solid-supported gold nanorods were influenced by the nanoparticle surface coverage.
- In **Paper III**, the objective was to assess the NIR light-intensity dependent antibacterial activity of solid-supported gold nanorods on two different support materials, titanium and glass. This work serves as a proof-of-concept study of the antibacterial activity of the solid-supported gold nanorods, and highlights differences in the origin of the antibacterial effect depending on the support material.
- In **Paper IV**, the objective was to assess the antibacterial activity and mode of action of gold nanorods supported on glass combined with an antimicrobial peptide in suspension. This work also investigates the material-bacteria interaction with electron microscopy.

2. Background

2.1 Gold nanoparticles for biomedical applications

Gold nanoparticles have garnered scientific attention ever since the mid-1800s when Michael Faraday began studying the interaction between metal particles and light.[13] It is, however, over the last decades that the unique optical and chemical properties of gold nanoparticles have been applied in a range of research fields, including sensing, catalysis, drug delivery, imaging, and photothermal therapy.[14] As the dimensions of a material are reduced to the nanoscale of 1-100 nm, properties arise that are not present in the bulk counterpart. These properties originate from the small size and high surface-to-volume ratio, resulting in spatial confinement of the material's electronic motions. Gold and other plasmonic nanoparticles are particularly utilised owing to their interesting optical properties, caused by the unique light-matter interactions in these materials. When a gold nanoparticle is exposed to the oscillating electric field of light, a collective oscillation of the conduction band electrons with respect to the positive gold lattice will occur. This process has a resonance at a specific frequency of light and is known as the localised surface plasmon resonance (LSPR) oscillation.[15] The generation of LSPR oscillations of the conduction band electrons effectively confine resonant photons to the small size of the particle, and this plasmonic confinement strongly enhances all radiative processes, like light extinction and fluorescence.[16] After plasmon excitation, the collective electron oscillation will be subjected to a series of damping processes that eventually lead to the plasmon's decay. Damping which occurs through radiative processes results in photon emission. Non-radiative damping occurs through a series of photophysical processes, starting with a phase loss of the excited electrons and ending up with cooling of the metal lattice by passing the heat via phonon-phonon relaxation to the surrounding medium.[16] Upon exposure to resonant light, the gold nanoparticles can therefore function as efficient photothermal agents.

The resonance frequency of gold nanoparticles is determined by the size and shape, as well as by extrinsic factors like the dielectric constant of the surrounding medium, and when assembled, the interparticle spacing and relative orientation.[16] A spherical gold nanoparticle has one resonance frequency owing to the symmetrical shape, and in an aqueous environment this frequency is in the visible spectral region around 500 nm (Figure 1). Transitioning from a sphere to an anisotropic rod-shape will instead give rise to two resonance frequencies, associated with the two characteristic dimensions of the gold nanorod: a transverse owing to oscillations along the width of the particle, and a longitudinal owing to oscillations along the length (Figure 1). The longitudinal LSPR frequency is dependent on the aspect ratio (length / width) of the gold nanorod, where increasing the aspect ratio shifts the frequency from the visible to the near-infrared (NIR) spectral region. In the NIR range of 750-900 nm, known as the first biological window, tissue penetration of light is optimal due to the low absorption of water and heamoglobin.[17,18] Gold nanorods are frequently utilised in biomedical applications owing to their tuneable optical properties throughout the biological window, which enable extracorporeal plasmon excitation and heat generation.

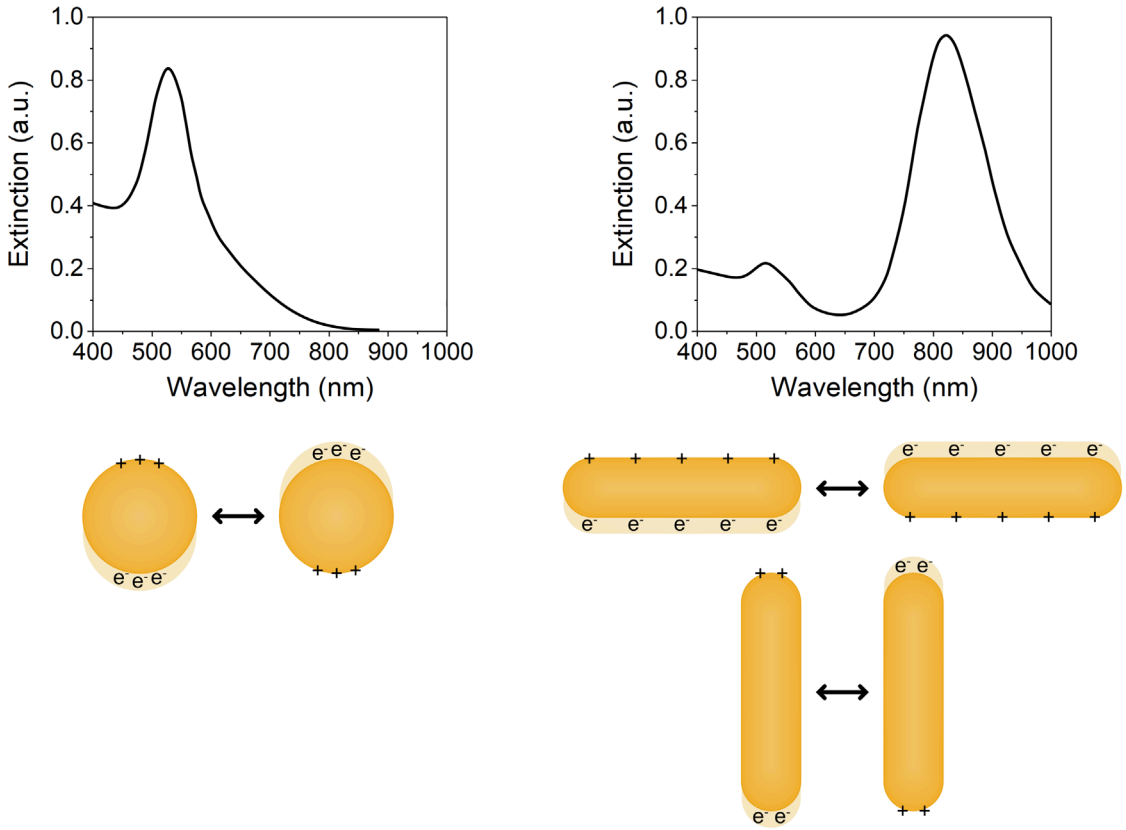


Figure 1. Illustration of the Vis-NIR extinction spectra and localised surface plasmon resonance oscillations of a gold nanosphere (left) and a gold nanorod (right).

2.1.1 Size and shape control

Significant effort has been spent on developing synthesis procedures for gold nanoparticles, allowing for accurate control of the size and shape, and therethrough their optical properties. Gold nanoparticles are commonly synthesised via bottom-up, wet-chemical procedures which enable precise control of the size and shape, are scalable, and give high yield while maintaining low size-dispersity. The synthesis of spherical gold nanoparticles dates to Faraday during the mid-1800s,[13] but nowadays modified versions of the Turkevich method from the 1950s[19] are most common. The Turkevich method uses an aqueous solution of gold (III) chloride trihydrate ($HAuCl_4$) which is reduced by citrate under boiling,[20] wherein the citrate works both as the reducing agent and as the stabilising ligand capping the formed gold nanospheres. When transitioning to synthesising an anisotropic shape, like a gold nanorod, the shape-control is achieved by preferential reduction of gold ions onto specific crystal facets of the nanoparticle, tuning the growth rates and causing the particle to grow faster along a certain direction.

Gold nanorods are commonly synthesised via a seed-mediated approach, owing to the ease of controlling particle size and the high quality and yield of the obtained nanoparticles. The synthesis, which occurs in the presence of hexadecyltrimethylammonium bromide (CTAB) and silver, originates from a method published by Jana *et al.* in 2001,[21] and was modified by Nikoobakht and El-Sayed in 2003.[22] It is a two-step, water-based procedure where (i) a seed suspension is prepared by reducing $HAuCl_4$ in the presence of CTAB with sodium borohydride, and (ii) the gold seed particles are added to a growth solution containing Au^+ ions, obtained from reduction of $HAuCl_4$ with ascorbic acid, CTAB and silver nitrate. The use of a weak reducing agent like ascorbic acid is critical as it ensures that the reduction of Au^+ to Au^0 only occurs on the seed particles, which act as catalysts for the reduction,[23] causing the seeds to grow until they form single crystalline gold nanorods. CTAB has an important shape-directing role, essential for the transition from the initial spherical seed to the anisotropic rod-shape, and acts as the capping ligand ensuring colloidal stability through a combination of electrostatic and steric stabilisation. The silver ions facilitate rod-formation and are important in controlling the aspect ratio of the nanorods. In this thesis, a version of the seed-mediated synthesis with CTAB and silver nitrate, adapted from a protocol described by Scarabelli *et al.*,[23] has been used to synthesise gold nanorods with longitudinal resonance frequencies in the NIR region, spanning 825-850 nm.

The growth mechanism of single-crystalline gold nanorods is a complex and well-discussed topic. In brief, during the initial seed particle growth, distinct {110} and {100} facets are formed. The CTAB molecules bind preferentially to the {110} side facet. Ag^+ is reduced to Ag^0 at the particle surface through underpotential deposition and the deposition of silver occurs at a higher rate on the {110} side facet compared to the {100} end facet.[16] CTAB binding and a higher rate of silver deposition on the {110} facets slow down the growth on the sides of the particles, and preferential growth along the [110] direction and formation of a rod shape occurs.

2.1.2 Solid-supported gold nanoparticles

To harness the unique properties of gold nanoparticles, many applications require the particles to be supported on a solid material surface. Solid-supported gold nanoparticles have been employed in various application areas, including sensing,[24] catalysis,[25] investigations of cell-adhesion,[26] and development of antibacterial materials.[27] To fabricate these types of materials, the surface-attachment of gold nanoparticles to a solid support is an essential process. The surface-attachment of gold nanoparticles is generally achieved through chemisorption, but alternative strategies, like growing the nanoparticles directly on the support through *in situ* reduction or relying on physisorption through drop casting, can also be employed.

When surface-attaching gold nanoparticles through chemisorption, the substrate surface is modified with functional groups to which the nanoparticles are subsequently attached. As thiol groups form strong, quasi-covalent bonds to gold, surface-functionalisation with a thiol-containing compound like a mercaptosilane is a common strategy. Alternatively, since gold nanoparticles in suspension generally are stabilised with charged ligands, modifying the substrate to obtain the opposite charge will allow for electrostatic attachment. Electrostatic attachment can be achieved with amine groups, e.g. using aminopropyltrimethoxysilane (APTES), for citrate-stabilised gold nanospheres,[28,29] or with an anionic polymer like polystyrene sulfonate (PSS) for CTAB-stabilised gold nanorods.[30] In this thesis, gold nanorod surface-attachment was primarily achieved utilising electrostatic interactions between the cationic, CTAB-stabilised particles, and an anionic glass or titanium surface.

When relying on chemisorption, the gold nanoparticle adsorption to the surface will be a random process. Owing to the surface charge introduced by the stabilising ligands on the nanoparticles, the distance between neighbouring particles will be determined by their mutual electrostatic repulsion. The range of the electrostatic repulsion is governed by the thickness of the electrostatic double layer surrounding the particles, as described by DLVO theory.[31] To overcome this limitation in packing density, the ion concentration in the nanoparticle suspension can be tuned, where an increase in ionic strength will lead to a reduction of the Debye screening length.

2.1.2.1 Factors influencing the properties

The properties of materials based on solid-supported gold nanoparticles are, in addition to the nanoparticles' innate characteristics, determined by the properties of the surrounding medium, including the type of support material, and the inter-nanoparticle interactions. The influence from the support material stems from its dielectric constant, ε_m. The real part of the dielectric constant, $\mathrm{Re}(\varepsilon_m)$, describes a material's ability to store electrical energy, and for a plasmonic system this governs the resonance frequency. The imaginary part, $\mathrm{Im}(\varepsilon_m)$, represents losses in the system (damping). For a non-absorbing environment, where $\varepsilon_m = \mathrm{Re}(\varepsilon_m)$, an increase in the dielectric constant will result in a red-shift of the resonance frequency.[14] For example, the resonance frequency of gold nanoparticles supported on glass (a non-absorbing support) will red-shift if the material is transferred from being surrounded by air to being immersed in water. For an absorbing environment, in addition to the resonance shift governed by $\mathrm{Re}(\varepsilon_m)$, the losses

associated with Im(ε_m) can also greatly affect the system,[14] causing phenomena like substrate-induced damping.

For gold nanoparticles assembled on a solid support, the interparticle interactions become important in defining the material's optical properties. The plasmons on individual gold nanoparticles can influence each other depending on the distance between them and their relative orientation, a phenomenon known as plasmon coupling. In a simple case of a dimer of nanospheres, excitation along the dimer axis will cause a red-shift in the LSPR frequency, whereas excitation perpendicular to the axis will induce a blue-shift.[14] For a dimer of gold nanorods, the anisotropic particle shape gives rise to a range of plasmon coupling modes, which, depending on the nanorods' relative orientation, can cause the LSPR to either red- or blue-shift.[32] In addition to influencing the optical properties, assembling gold nanoparticles on a solid support will also influence the photothermal characteristics. In an array of plasmonic nanoparticles under illumination with resonant light, the temperature a nanoparticle experiences will come from two contributions, (i) a self-contribution caused by heating of that nanoparticle, and (ii) a collective temperature increase caused by the heating from neighbouring nanoparticles.[33] In such a system, two distinct heating regimes can be discerned, where the temperature increase is either confined to the vicinity of each nanoparticle, or delocalised with a uniform temperature throughout the assembly.

2.1.2.2 Gold nanoparticle gradient surfaces

As the properties of solid-supported gold nanoparticles are influenced by the interparticle interactions, the ability to control nanoparticle surface-attachment is central in the material development and optimization. For this purpose, nanoparticle gradient surfaces hold great potential. In these materials, nanoparticles are attached in a number density gradient along a support, enabling property evaluation and optimization on a single sample. Moreover, nanoparticle gradient surfaces show promise as platforms for combinatorial and screening studies. Gold nanoparticle gradient surfaces have been manufactured through a range of methodologies. The strategies include bipolar electrochemistry,[34] creating a chemical gradient on the support surface to which the nanoparticles are attached,[35,36] and controlling chemisorption to the surface by making a gradient in ionic strength in the gold nanoparticle suspension.[37] In addition, dip-coating has been used to create nanoparticle gradient surfaces with silica nanoparticles, utilising adsorption kinetics to tune the number density along the support.[38] In **Paper II** of this thesis, a method similar to the dip-coating approach has been developed to prepare gold nanorod gradient surfaces, relying on nanoparticle adsorption kinetics to control the surface coverage, and the prepared materials' optical and photothermal properties were evaluated

2.1.3 Nanothermometry of gold nanoparticles

The photothermal properties of gold nanoparticles are of relevance for biomedical applications, with potential use for a range of therapeutic purposes. Of particular interest is their application in photothermal therapy, where the heat emitted from the nanoparticles upon excitation with resonant light is used to treat a medical condition.[39,40] When utilizing the photothermal

properties of gold nanoparticles, the temperature that the particles reach upon excitation is a critical parameter for successful implementation. Determining the temperature of gold nanoparticles is, however, a non-trivial task as the heat that the particles generate is spatially confined to the nanoscale. To overcome this challenge, a range of methodologies have been developed for assessing the heating of plasmonic nanoparticles.[41] Most of the methods are indirect and assess the temperature from a change in properties of the surrounding medium, for example by monitoring changes in refractive index or viscosity,[42,43] by using fluorescent probe molecules or upconverting nanoparticles,[44–46] or by observing the phase transition of a lipid bilayer.[47,48] The indirect nature of these techniques means that only the temperature in close vicinity of the nanoparticles can be assessed, and, moreover, the spatial resolution of the methods that rely on optical detection is limited by the diffraction limit of visible light.[41]

An alternative approach that can directly determine the temperature increase of gold nanoparticles monitors the crystal lattice expansion that occurs upon heating of the particles. X-ray diffraction can be used to follow shifts and shape changes of the Bragg peaks from the crystalline gold nanoparticles under illumination with resonant light, allowing accurate determination of their temperature as well as assessment of potential structural changes in the particles. This concept has been employed at synchrotron facilities to study gold nanospheres in water and on silicon substrates,[49,50] revealing valuable insight into how the temperature varies with light intensity as well as pre-melting and recrystallisation of the particles. In **Paper I** and **Paper II**, a similar *in situ* XRD methodology has been used to study the photothermal properties of the solid-supported gold nanorods under NIR irradiation.

2.1.4 Plasmonic photothermal therapy

In photothermal therapy (PTT), local heating stemming from the excitation of a photothermal agent with resonant light is used to treat a medical condition, for example by inducing thermal damage to tumour tissue in cancer therapy. Photothermal agents that have been employed for this purpose include natural chromophores in tissue and photoabsorbing dyes.[40] As natural chromophores exhibit relatively low absorption efficiency and dye molecules undergo photobleaching, nanomaterials such as carbon nanotubes, polymer nanoparticles, and plasmonic metal nanoparticles, have emerged as promising alternatives to overcome these limitations.[51] When considering *in vivo* applications, photothermal agents with excitation frequencies in the NIR spectral region which facilitate extracorporeal excitation are of particular interest. Here, the use of NIR-resonant gold nanoparticles, like gold nanorods, is beneficial owing to their tuneable optical properties, enhanced absorption cross section, ease of preparation, and ready (bio)functionalisation.[40] Additionally, gold nanoparticles have been shown to exhibit relatively low toxicity potential.[52–54] For gold nanorods specifically, the CTAB used in the synthesis is toxic at sub-micromolar concentrations, and studies have highlighted the importance of distinguishing between toxicity induced by the nanorods and by the free CTAB molecules in the suspension.[55] By overcoating the CTAB ligand on the nanorods with a polyelectrolyte, or exchanging the ligand with more biocompatible molecules, the biocompatibility can be enhanced.[56]

Gold nanorods have most prominently been researched in plasmonic photothermal therapy (PPTT) of different types of cancer cells,[57,58] but also for targeting bacterial cells to treat infections.[59,60] When employed in PPTT applications relying on systemic administration of the gold nanorods in suspension, the particles are commonly functionalised to improve stability and to achieve specific targeting in the biological environment. Functionalisation with polyethylene glycol (PEG) is common as it prevents nanoparticle aggregation, enhances biocompatibility, and works as a passive targeting method wherein the PEG-ylated nanoparticles accumulate in tumour tissue due to the enhanced permeability and retention effect.[40] Active targeting for cancer therapy can be achieved by functionalising the gold nanorods with ligands specific to biomarkers on the targeted cell type, such as antibodies or folic acid.[40] This active targeting approach has also been utilised against bacterial infections, where ligands specific to moieties on the bacterial cell envelope were used.[59,60]

Despite the efforts to enhance nanoparticle stability and targeting specificity through various functionalisation methods, there are still challenges with systemic administration of gold nanorods for PPTT. Passive targeting through the enhanced permeability and retention effect is inefficient, with only a small fraction of the administered nanoparticles reaching the target, and active targeting by functionalisation with specific ligands is often negated by the formation of a protein corona *in vivo*.[39] For combatting biomaterial-associated infections, a more promising strategy is utilising the photothermal properties of gold nanorods in the development of antibacterial material modifications. Attaching gold nanorods to a material surface ensures their stability, and a light-activated antibacterial effect at the site of bacterial colonisation can be realised.

2.2 Antibacterial modifications of biomaterials

Biomaterial-associated infections are notoriously hard to treat owing to the ability of biofilm-growing bacteria to evade the immune response and their high tolerance to conventional antibiotics. Bacteria in biofilms are enclosed in a self-produced, protective biopolymer matrix consisting of polysaccharides, DNA, and proteins. The protective matrix and the regularly low metabolic activity of biofilm-growing bacteria are the origin of the observed high tolerance to antibiotics, occasionally requiring up to 1000-fold higher concentrations compared to planktonic bacteria.[7] The development of antibacterial modifications of biomaterials can circumvent this issue by providing a locally high antibacterial activity at the biomaterial surface, with the additional benefit of preventing exposing the healthy microbiota to antibacterial agents. Nonetheless, developing a modification strategy that can achieve a prominent, broad-spectrum antibacterial activity, while not hindering the local immune response or harming the surrounding tissue, is a challenging task. Considering the demanding requirements, it becomes obvious that there is no universal modification strategy and that each biomaterial application requires individual adaptation.

2.2.1 Overview of modification strategies

Reflecting the diverse requirements for antibacterial modification strategies of biomaterials, a variety of approaches have been developed. These approaches can broadly be divided into anti-adhesive (or anti-fouling) surfaces, antimicrobial-releasing materials, contact-killing surfaces, or a combination of the above.[61] Anti-adhesive surface modifications aim to prevent initial bacterial colonisation and can be realised with polymer or polymer brush coatings, as well as by the introduction of micro- or nanostructures that tune the surface topography.[11] For antimicrobial-releasing materials, the antibacterial agent can, depending on the material properties, be loaded into the bulk or incorporated into a coating. The release of various antibacterial agents has been studied, including conventional antibiotics, antimicrobial peptides (AMPs), and metal ions (silver, copper, zinc). Contact-killing surfaces have been achieved by the immobilisation of antibacterial agents like AMPs and quaternary amines,[11] as well as through nanotopography features that cause physical damage to the bacterial cell wall.[12] An illustration of these general modification strategies is shown in Figure 2.

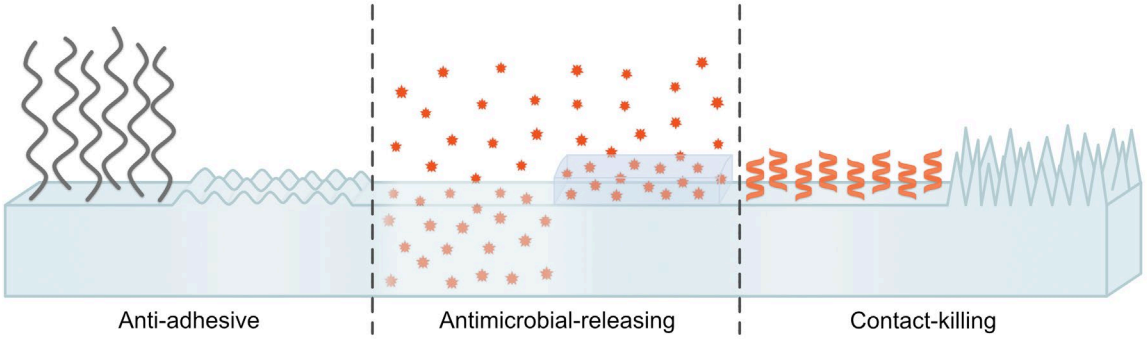


Figure 2. Schematic illustration of the general approaches employed to develop antibacterial modifications of biomaterials.

As previously mentioned, modification strategies utilising the NIR light-activated plasmonic heating of gold nanorods have also been studied for the purpose of combatting BAIs. The photothermal antibacterial activity of solid-supported gold nanorods on a range of support materials has been demonstrated, including glass,[62,63] titanium,[64] polyurethane,[27,65] polypropylene,[66] and polyacetonitrile.[67] The bactericidal effect has been studied primarily for low NIR light intensities as a function of irradiation time, with gold nanorod loadings ranging from a couple of hundred nanoparticles per μm^2 to multilayers completely coating the material surface. To further explore the antibacterial activity of materials based on solid-supported gold nanorods, **Paper III** of this thesis studied well-defined monolayers of nanorods on glass and titanium, evaluating the antibacterial effect as a function of NIR light intensity and examining the influence of the support material.

2.2.2 Multifunctional strategies

To effectively develop material modifications that can combat BAIs, the use of multifunctional approaches combining several antibacterial strategies could be of great importance, ensuring a robust and versatile effect. One multifunctional strategy is combining different classes of

antibacterial modifications, for example by creating an anti-adhesive and contact-killing surface, such as using polymer brushes functionalised with antimicrobial peptides.[68,69] As biomaterials are commonly used in concurrence with administration of antimicrobial agents, including as preoperative antibiotic prophylaxis and as treatment of implant-associated infections,[70,71] investigating the effect of antibacterial material modifications in the presence of antimicrobials in suspension is another potential strategy. For the antibacterial effect of solid-supported gold nanorods this is of particular interest as photothermal heating has been shown to enhance the efficacy of certain antimicrobials.[72–74]

In **Paper IV**, the antibacterial activity of the solid-supported gold nanorods on glass combined with an antimicrobial peptide in suspension was investigated. As many conventional antibiotics are losing their efficacy due to the increased occurrence and spread of antimicrobial resistant pathogens, AMPs have emerged as a promising alternative class of antimicrobial compounds. AMPs are an important part of the immune response of most multicellular organisms, with key structural features including a small size, amphipathic character, ability to form secondary structures and, importantly, net cationic charge.[75] The net cationic charge of these peptides allows them to selectively target bacterial cells through electrostatic interactions with anionic moieties in the bacterial cell envelope,[76] whereafter the hydrophobic domains of the peptides can interact with the phospholipid bilayer, which often leads to disruption of the membrane integrity. The antibacterial activity of AMPs is, however, not limited to the membrane-disruptive mode of action (MoA), with studies showing that the peptides can cross the bacterial membrane and act internally by targeting for example cell division, DNA or RNA synthesis, protein synthesis and protein folding.[75] Additionally, when combining AMPs with the photothermal heating of gold nanorods, enhanced antibacterial activity has been demonstrated.[73,77–79]

In this thesis, the cationic AMP RRPRPRPRPWWWW-NH_2 (RRP9W4N) was studied, structure shown in Figure 3. This AMP has formerly been utilized by our research group for covalent attachment onto hydrogel sheets and particles, creating materials with broad-spectrum antibacterial activity.[80–84] In addition to studying the antibacterial activity of the solid-supported gold nanorods combined with the RRP9W4N AMP, the MoA of the combined system was also investigated in **Paper IV**, using bacterial cytological profiling.

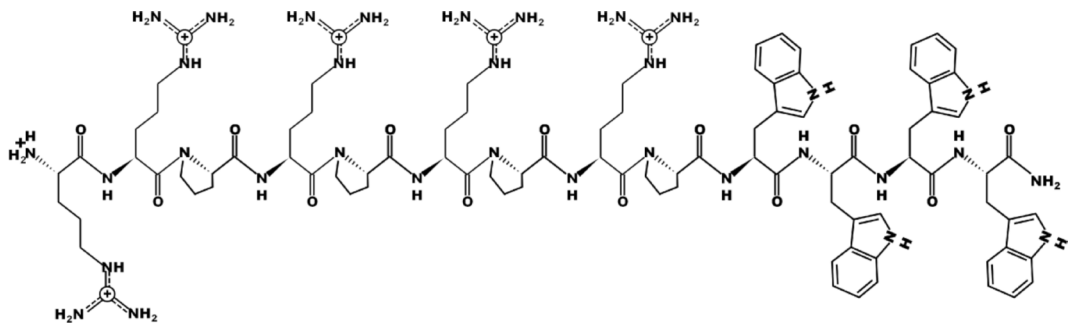


Figure 3. Chemical structure of the RRP9W4N AMP (RRPRPRPRPWWWW-NH_2).

2.3 Bacterial cytological profiling

Bacterial cytological profiling (BCP) is a fluorescence light microscopy-based technique for mode of action analysis of antimicrobial compounds. The technique offers a rapid overview of possible cellular targets and can be used for a range of bacterial species. BCP is a phenotypic assay that utilises fluorescent membrane and DNA staining dyes, commonly in combination with phase contrast microscopy, to study how bacteria respond to an antimicrobial agent.[85,86] There exists a multitude of fluorescent dyes that can be used for this purpose, targeting specific cellular components or functions. Amongst the most common are DNA dyes, like 4′,6-diamidino-2-phenylindole (DAPI), which enable monitoring of the nucleoid morphology, and membrane dyes, like NileRed or FM4-64, that can be used to study membrane morphology and phase separation. In **Paper IV** of the thesis, BCP was used to study the mode of action of the solid-supported gold nanorods and the RRP9W4N AMP, both individually and in combination.

3. Methodology

This chapter gives an overview of the material preparation procedures and the characterisation techniques included in the thesis. The following is a description of the *in situ* X-ray diffraction methodology used to evaluate the photothermal properties of the solid-supported gold nanorods in **Paper I** and **Paper II**. Lastly, an overview of the *in vitro* antibacterial activity evaluation from **Paper III** and **Paper IV**, and the bacterial cytological profiling from **Paper IV** are given. The near-infrared laser used throughout the thesis had a central wavelength of 808 ± 3 nm (DS3-51523-50W, BWT Beijing Ltd.), and different configurations were used where the collimator unit was adapted to achieve beam spot sizes suitable for a particular experimental setup. All the materials and experimental procedures are described in detail in the papers appended to the thesis.

3.1 Material preparation

3.1.1 Gold nanorod synthesis

Gold nanorods (AuNRs) were synthesised using a seed-mediated procedure adapted from a protocol by Scarabelli *et al.*[23] Initially, small (typically < 2 nm) gold seeds were prepared in a 30 °C water bath by mixing 4.7 ml of 100 mM CTAB solution with 25 µl of 50 mM $HAuCl_4$ until homogeneous. The Au^{3+} was reduced by addition of 300 µl freshly prepared 10 mM sodium borohydride solution, forming the small gold nuclei to be used as seed particles. A growth solution was prepared in a 30 °C water bath by mixing 60 ml 100 mM CTAB solution with 1.14 ml 1 M hydrochloric acid and 600 µl $HAuCl_4$ solution. Subsequently, 720 µl silver nitrate solution and 600 µl ascorbic acid were added. The concentrations of silver nitrate and ascorbic acid were varied between 8-11 mM and 90-110 mM, respectively, to tune the aspect ratio of the nanorods. Upon addition of ascorbic acid, the Au^{3+} ions will be reduced to Au^{+}, indicated by the transition of the colour of the growth solution from yellow to transparent.

Lastly, 144 µl of the seed suspension was added to the growth solution, mixed thoroughly, and left undisturbed at 30 °C for approximately 2 h. The synthesis procedure is schematically illustrated in Figure 4. The synthesised AuNRs were purified from the reaction mixture by three consecutive centrifugation steps with redispersion in ultrapure water between each. The stock AuNR suspensions were stored at 4 °C protected from light.

The main type of AuNR used throughout the thesis had a longitudinal resonance peak around 830-840 nm and an average aspect ratio of 3.9. In **Paper I**, another population of AuNRs was also studied, with an average aspect ratio of 4.4. To distinguish the two populations of nanorods in this paper, they are referred to as AuNR 3.9 and AuNR 4.4. Two different populations of nanorods were also studied in **Paper IV**, with longitudinal resonance peaks at 840 nm and 870 nm. In this paper, the two populations are referred to as AuNR840 and AuNR870.

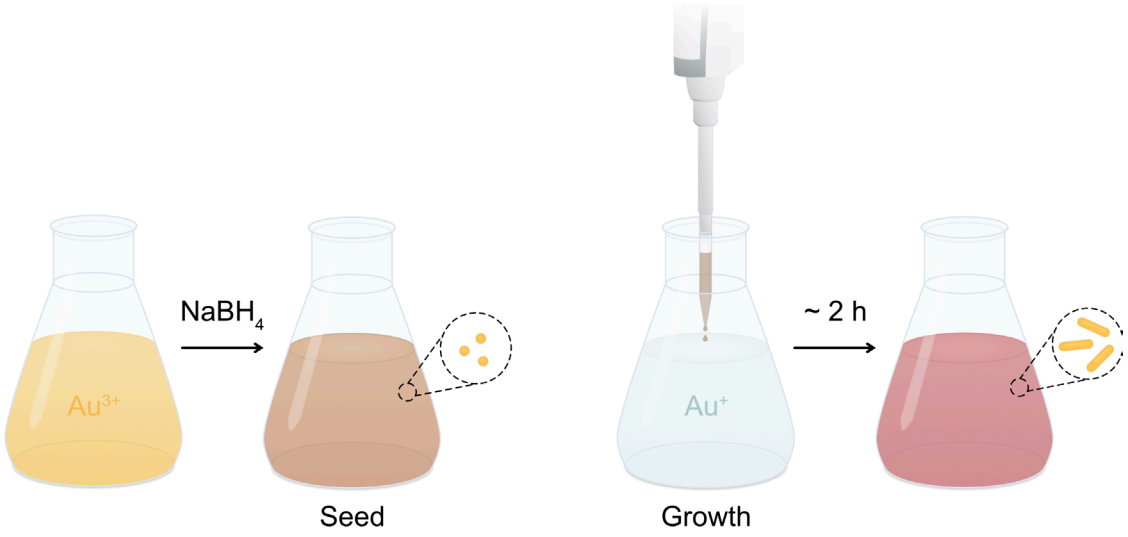


Figure 4. Schematic illustration of the seed-mediated gold nanorod synthesis.

3.1.2 Surface-attachment of gold nanorods

In this thesis, two different support materials were utilised. The main support was glass (or fused silica) which was chosen owing to the suitable optical properties (transparent to NIR light). In **Paper III** and **Paper IV**, titanium substrates were also employed, as a common material used for biomaterial applications, e.g. in orthopaedic implants. Throughout the thesis, the gold nanorods supported on glass and titanium will be referred to as Glass-AuNR and Ti-AuNR, respectively.

The AuNR surface-attachment utilised electrostatic interactions between the cationic, CTAB-stabilised AuNRs and an anionic support surface. Glass and titanium substrates were rinsed in 95% ethanol (EtOH) followed by ultrapure water, before being dried in a flow of nitrogen gas. The glass substrates were immersed in 65-67% nitric acid overnight (18-19 h), whereafter they were thoroughly rinsed with ultrapure water and then immersed in an AuNR suspension. The titanium substrates were UV/O_3-treated for 15 min and then immersed in an AuNR suspension. By varying the concentration of the AuNR suspension and the immersion time, the surface

coverage of nanorods on the support was tuned. The concentration of the AuNR suspensions (weight of gold per volume, µg ml^{-1}) was estimated from the absorbance at 400 nm, according to a correlation described by Scarabelli *et al.*[23] Once the AuNR immersion was completed, the suspension was exchanged to ultrapure water, whereafter the substrates were extracted, immersed in 99.5% EtOH and then allowed to air dry.

3.1.3 Gold nanorod gradient surfaces

The preparation of the gold nanorod gradient surfaces in **Paper II** utilised nanoparticle adsorption kinetics to control the surface coverage of AuNRs over the support, by gradually withdrawing the AuNR suspension from the support surface. Fused silica substrates (9 mm x 20 mm x 0.3 mm) were cleaned by immersion in nitric acid, as described in section 3.1.2. After rinsing with ultrapure water, the substrates were rinsed with 95% EtOH and then immersed in a 1 mM solution of (3-mercaptopropyl)trimethoxysilane (3-MPS) in EtOH for 1 h. After functionalisation with 3-MPS, which facilitated AuNR attachment through gold-thiol bonds, the substrates were rinsed with EtOH followed by ultrapure water before being used immediately in the gradient preparation procedure.

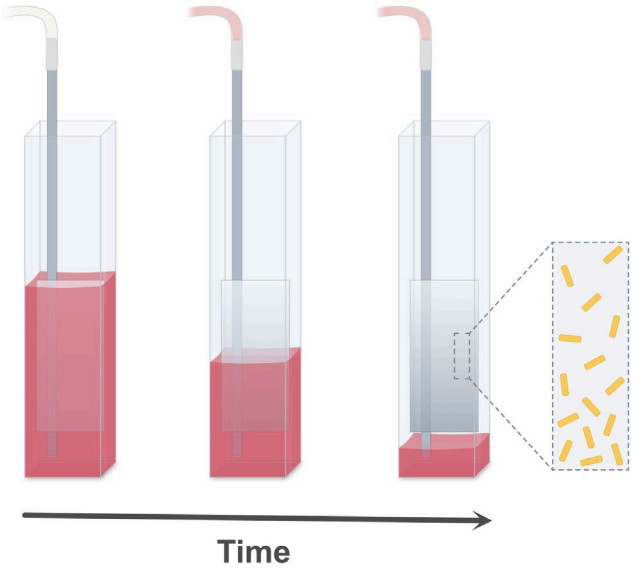


Figure 5. Schematic illustration of the setup used for the gold nanorod gradient surface preparation. A 3-MPS functionalised fused silica substrates was immersed vertically in a gold nanorod suspension, which was withdrawn at a fixed rate through a syringe needle connected to a programmable syringe pump, resulting in an increasing surface coverage of gold nanorods from top to bottom of the substrate.

The gradient surfaces were prepared in single-use cuvettes with a 10 mm path length. The 3-MPS functionalised substrates were immersed vertically 20 mm into the AuNR suspension, ensuring the entire substrate was covered and an approximately 5 mm gap was left at the bottom of the cuvette. The suspension was withdrawn from the bottom of the cuvette at a fixed rate, 0.15 or 0.30 mm min^{-1}, using a syringe needle connected to a programmable syringe pump. A schematic illustration of the setup is shown in Figure 5. In this setup, a gradient was fabricated where the surface coverage of gold nanorods increased from the top to the bottom of the

substrate. The withdrawal rate determined how long the different sections of the substrate were exposed to the AuNR suspension and was thus used to tune the gradient dynamics, with a higher withdrawal rate resulting in an overall lower surface coverage of AuNRs.

3.2 Material characterisation

3.2.1 Electrophoretic light scattering

The surface charge of the gold nanorods was estimated by measuring the electrophoretic mobility of the particles. In electrophoretic light scattering (ELS), an electric field is applied to the liquid sample, causing the charged particles in the liquid to move towards the oppositely charged electrode. Coherent incident light illuminates the moving particles and due to their movement, the frequency of the light scattered by the particles will differ from the frequency of the incident light, owing to the Doppler effect.[87] From the frequency shift, the electrophoretic mobility is calculated, and using the Smoluchowski approximation (for polar systems) the Zeta potential of the particles can be calculated from the electrophoretic mobility. ELS was measured on a Litesizer DLS 500 (Anton Paar). The AuNR suspension was diluted with ultrapure water to an estimated concentration of 15 µg ml^{-1}. The ELS measurements were performed at 25 °C and repeated three times.

3.2.2 Transmission electron microscopy

Transmission electron microscopy (TEM) was used in this thesis to determine the dimensions and crystal structure of the gold nanorods. TEM is a high-resolution electron microscopy technique that typically can resolve distances down to 0.1-0.3 nm, enabling the resolution of atomic spacing in crystalline materials. A thin sample (< 100 nm) is exposed to a high-energy electron beam (generally 100-300 kV) and characteristic signals, including secondary electrons, back-scattered electrons, and characteristic X-rays, are generated through electron-matter interactions.[88] In TEM, the signals that are transmitted through the sample are detected and used for imaging. In this thesis, bright-field imaging, where contrast is generated by the relative number of transmitted electrons, was used to evaluate morphology and phase contrast of the samples.

In **Paper I** and **Paper III**, TEM samples were prepared on copper grids with an ultrathin carbon film supported on a lacey carbon film from Ted Pella. The copper grids were UV/O_3-treated prior to the deposition of a 5 µl droplet of AuNR suspension with an approximate gold concentration of 25 µg ml^{-1}. Excess suspension was removed by blotting the grid with filter paper. Characterisation was performed on a FEI Titan 80-300 TEM, operated in TEM mode at 300 kV acceleration voltage. TEM micrographs were analysed in GATAN Microscopy Suite 3 and Fiji (ImageJ).[89] The length, width and aspect ratio of the gold nanorods were determined from measuring 400 particles.

In **Paper IV**, TEM investigations of the interaction between supported gold nanorods on titanium and *Staphylococcus aureus* were conducted. Prior to studying the bacterial samples with electron microscopy, they were fixated in 4% formaldehyde overnight (18-19 h) at 4 °C.

The samples were then stepwise dehydrated in an ethanol concentration gradient before being immersed in a 50 vol% hexamethyldisilazane (HMDS) in ethanol. Lastly, the samples were immersed in pure HMDS (99%), before the HMDS was removed and the samples allowed to air dry. The samples were sputter coated with a 100 nm protective chromium layer and TEM specimens were prepared according to conventional focused ion beam scanning electron microscopy (FIB-SEM) lift-out protocol,[90] using a Versa 3D with a mono-isotopic Ga (69 amu) ion source. A SEM micrograph of a typical TEM specimen from the FIB-SEM during the final thinning step using ion beam milling is shown in Figure 6, with the bacterial cells visible as the dark, rounds spots at the top of the lift-out. The TEM specimens were analysed with a FEI Titan 80-300 operated at 300 KV and imaged in brightfield TEM-mode.

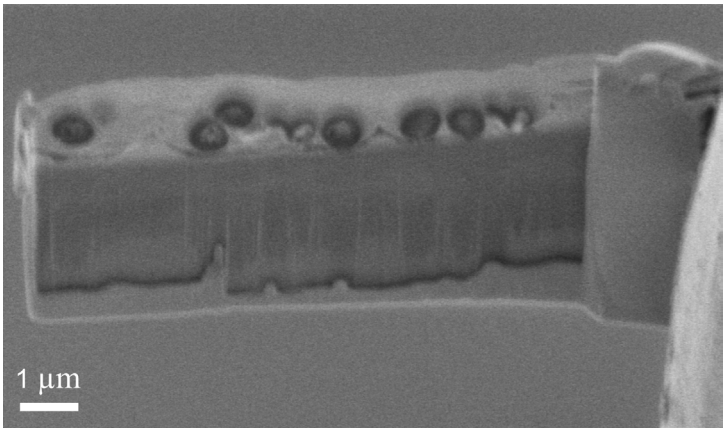


Figure 6. Micrograph of a TEM specimen prepared with FIB-SEM, during the final thinning step. The *S. aureus* cells are visible as the dark round spots at the top of the lift-out, resting on the titanium substrate functionalised with gold nanorods.

3.2.3 Scanning electron microscopy

Scanning electron microscopy (SEM) was used to image the solid-supported gold nanorods and to study the material-bacteria interaction on the samples. In SEM, an electron beam, generally with acceleration voltage in the range of 1-30 kV, is focused by electromagnetic lenses and raster scanned over an area of the specimen surface. At each position, characteristic signals including secondary electrons, back-scattered electrons, and characteristic X-rays, are detected and from the relative number of electrons collected at each position, a contrast-based micrograph is generated.[91] In this thesis, secondary electron detection was used owing to the high sensitivity to surface features, providing topographic information. The solid-supported gold nanorods were imaged in secondary electron mode with acceleration voltages of 2-5 kV. From the micrographs, the surface coverage of gold nanorods was determined as the projected area covered by particles, in percent. SEM was also used to study the material-bacterial interaction on the samples in **Paper III** and **Paper IV**. The bacterial samples were fixated as described in section 3.2.2, and sputter coated with ~5 nm gold prior to SEM characterisation.

3.2.4 Vis-NIR spectroscopy

Vis-NIR spectroscopy has been extensively used throughout the thesis to characterise the optical properties of the gold nanorods in suspension and supported on glass. Vis-NIR spectroscopy studies how a material interacts with light in the visible to near-infrared spectral region, in this thesis specifically 400-1100 nm. By measuring the light absorption or light extinction (the sum of absorption and scattering) as a function of wavelength, information about the nanorods' plasmon resonance frequency, concentration or surface density, and interparticle interactions, can be obtained. Depending on the sample, two different Vis-NIR spectroscopy setups were employed. Vis-NIR absorption spectroscopy was primarily used to characterise the LSPR properties of the AuNR suspensions, and of the AuNRs supported on glass both in air and immersed in water. For this purpose, either a Multiscan GO Microplate Spectrophotometer, or a Hewlett Packard 8453 spectrophotometer was used. Vis-NIR extinction spectroscopy was employed in **Paper I** to experimentally determine the extinction cross sections of the solid-supported AuNRs. In **Paper II**, Vis-NIR extinction spectroscopy was used to evaluate the optical properties of the gold nanorod gradient surfaces, by recording extinction spectra every 2 mm along the samples. Extinction spectroscopy was performed on a home-built microscopy/transmission setup equipped with a halogen lamp (Newport) and a 10x air objective (NA 0.25) or a 4x air objective (NA 0.10) illuminating the sample. The transmitted light was detected with a photodiode array spectrometer (B&WTEK).

3.2.5 X-ray photoelectron spectroscopy

In **Paper III**, the surface chemical composition of the solid-supported AuNRs was evaluated with X-ray photoelectron spectroscopy (XPS). In XPS, the sample is exposed to monochromatic X-rays, and the kinetic energies of emitted characteristic photoelectrons are detected, which give information about the electronic states of the atoms. XPS is a surface-sensitive technique owing to the limited depth at which a photoelectron can be generated and escape the sample without undergoing inelastic scattering, typically 10 nm or less.[92] XPS was performed using a Versaprobe III spectrometer (PHI) with monochromated Al Kα radiation, and a 100 µm x 100 µm spot size on the samples was probed by the X-ray beam. The AuNRs supported on glass and on titanium, untreated and after the UV/O_3-treatment conducted to sterilise the samples prior to *in vitro* antibacterial activity evaluation, were studied. Emphasis was placed on the amount of gold and silver, giving information about the nanorods, and the amount of carbon, as an indicator of the removal of CTAB from the supported AuNRs after UV/O_3-treatment.

3.2.6 Thermal imaging

Thermal imaging was conducted using a testo 871s to evaluate the macroscopic heating of the solid-supported gold nanorods under NIR (808 nm) irradiation. In **Paper II**, the heating of both types of gradients, prepared with withdrawal rates of 0.15 and 0.30 mm min^{-1}, under irradiation at 0.6 W cm^{-2} was assessed. The gradient samples were placed onto a glass coverslip suspended on a support stage with an opening beneath, ensuring that only the gradients were exposed to the NIR laser beam. Thermal images were recorded during irradiation. In **Paper III**, the heating of the Glass-AuNR and Ti-AuNR were evaluated. The samples were placed onto agar plates

with the gold nanorods facing the agar and subsequently irradiated through the bottom of the agar plates. Thermal images were recorded before and after 30 s NIR irradiation at different laser intensities. Bare glass and titanium substrates were used as controls.

3.2.7 Optical microscopy

Optical microscopy was used for the bacterial cytological profiling in **Paper IV**, wherein phase-contrast microscopy in combination with fluorescent dyes was utilised in the mode of action study. In phase-contrast microscopy, phase shifts in light, caused by varying optical density in the specimen, are converted into brightness variations in the micrograph. This technique can produce high-contrast images of transparent specimens and was used to monitor morphological changes in the bacterial cells as well as cell lysis, which is visible as a phase density loss. Phase-contrast was combined with fluorescence microscopy, wherein the excitation of fluorophores in the specimen by specific wavelengths of light leads to emission of lower energy wavelengths, which are detected, creating an image of the fluorescently stained structures. The bacterial cytological profiling in **Paper IV** utilised four different fluorescent membrane or DNA staining dyes: DAPI (4′,6-diamidino-2-phenylindole), SYTOX™ Green, FM™ 4-64 (*N*-(3-Triethylammoniumpropyl)-4-(6-(4-(Diethylamino) Phenyl) Hexatrienyl) Pyridinium Dibromide), and $DiSC_3$5 (3,3'-Dipropylthiadicarbocyanine iodide).

DAPI stains DNA and SytoxGreen is a nucleic acid stain that cannot penetrated intact cell membranes, but easily crosses compromised membranes, and as such it can be used as an indicator of formation of large membrane pores. FM 4-64 is a membrane dye used to monitor membrane morphology, for example the occurrence of membrane foci, which can be caused by depolarization or membrane phase separation. $DiSC_3$5 is a voltage-sensitive dye that accumulates in polarised membranes and in the accumulated state its fluorescence self-quenches. Upon depolarisation the dye is released, resulting in de-quenching and an increase in fluorescence intensity.[85,93]

3.3 Modelling heating of plasmonic nanoparticle arrays

In **Paper I**, the experimental findings from the *in situ* XRD studies were compared with a theoretical model of the heating of plasmonic nanoparticle arrays. For a regular 2D array of plasmonic nanoparticles under illumination, the temperature increase in the centre of the array (ΔT_0) will be the sum of two contributing factors: (i) the self-temperature increase of a nanoparticle (ΔT_0^s), and (ii) the external temperature increase from the surrounding nanoparticles (ΔT_0^{ext}). In **Paper I**, the relative contribution of ΔT_0^s and ΔT_0^{ext} for the solid-supported AuNRs was compared through the dimensionless parameter ζ_2 (Equation 1).[33]

$$\zeta_2 = \frac{p^2}{3DR} \tag{1}$$

Where p is the periodicity of the nanoparticle lattice, D the diameter of the heated area, and R the nanoparticle radius (for an anisotropic particle an equivalent radius). For a system where ΔT_0^s is dominant, $\zeta_2 >> 1$, the nanoparticle temperature increase is independent of neighbouring

particles, remaining localised around each individual nanoparticle. When ΔT_0^{ext} is dominant, $\zeta_2 << 1$, collective heating governs, and the temperature increase is delocalised with a homogeneous temperature distribution over the entire array.

To predict the temperature increase as a function of laser intensity for the solid-supported AuNRs, the following model was used. The temperature increase of a 2D, infinite, square nanoparticle array under uniform circular irradiation can be estimated from[33]

$$\Delta T_0 = \Delta T_0^s + \Delta T_0^{ext} = \frac{\sigma_{abs} I}{4\pi \overline{K} R} + \frac{\sigma_{abs} I D}{4 \overline{K} p^2} \left(1 - \frac{2\sqrt{p^2}}{\sqrt{\pi} D} \right) \quad (2)$$

Where σ_{abs} is the absorption cross section of the nanoparticles, I the irradiance, $\overline{K}$ the average thermal conductivity of the substrate and the medium, and p the periodicity of the square lattice. The absorption cross sections of the gold nanorods were estimated in two ways: from theoretical calculations based on the nanoparticles' average dimensions and from experimental extinction spectroscopy data. The periodicities of the solid-supported AuNRs were determined through image analysis of average nearest neighbour distances in SEM micrographs.

3.4 *In situ* X-ray diffraction

In **Paper I** and **Paper II**, *in situ* X-ray diffraction (XRD) was the main technique used to study the photothermal properties of the solid-supported gold nanorods on glass under NIR irradiation. In XRD, an X-ray beam is directed at the sample, and the incident X-rays are scattered by the regularly arranged atoms in the sample. The X-rays scattered from the different atomic planes interfere with each other and at specific angles the path lengths of the interfering X-rays are an integer multiple of the X-ray wavelength, leading to constructive interference.[94] The condition for constructive interference is described by Bragg's law.

$$n\lambda = 2d \sin\theta \quad (3)$$

Where n is an integer, λ the wavelength of the X-rays, d the spacing between the crystal planes, and θ the Bragg angle (angle between the incident X-rays and the atomic planes). The constructively interfering X-rays produce unique diffraction peaks, and by detecting the intensity of the scattered beam through a range of 2θ-angles (angle between the incident and scattered beam), the diffraction peaks in the resulting diffractogram provide information about crystal structure and chemical composition of the sample. In this thesis, the temperature of the solid-supported AuNRs was determined from shifts of their diffraction peaks, caused by heating of the nanoparticles under NIR irradiation. Plasmonic heating of the AuNRs will cause the gold in the nanoparticles to thermally expand, resulting in an increase in the interplanar spacing d of the crystal lattice. As the interplanar spacing increases, the Bragg angle θ will decrease (Equation 3), and as such the diffraction peaks will shift to lower 2θ-angles. From determining the thermal expansion coefficient of the AuNRs, the diffraction peak shifts were used to assess their temperature.

3.4.1 Furnace heating and texture analysis

In **Paper I**, furnace heating experiments were performed to determine the thermal expansion coefficient of the AuNRs and to study how conventional heating affected the morphology of the solid-supported nanoparticles. The main series of experiments were performed on a D8 Advance diffractometer (Bruker) using a copper (Cu) X-ray source, a position-sensitive detector, and a variable slit set to 6 mm sample length. For the furnace experiments, the instrument was equipped with a XRK900 heating chamber (Anton-Paar) and the samples were placed on a Macor ceramic support inside the chamber. Temperature calibration was carried out using magnesium oxide powder deposited on the same glass substrate as the AuNRs, and sample displacement caused by thermal dilatation was determined based on a series of Z-scans using the same temperature ramp. The data from the AuNR measurements were corrected according to the sample displacement and temperature readout error. The (200) diffraction peak from the solid-supported AuNRs was monitored with 10-20 min scans in the 2θ range of 42-46°. The heating ramps were set to 1°/s and the samples were equilibrated for 30 min at each set temperature before the measurement.

A complementary series of measurements was performed on a SaxsLab Mat:Nordic system with a Rigaku 003 microfocusing Cu X-ray source and two Dectris detectors: Pilatus 300 K R (orthogonal to the beam) and 100 K (on a goniometer circle centred at the sample position). The configuration had lower peak position accuracy, but enhanced signal-to-noise ratio, owing to the focusing X-ray source and large 2D detector, and higher temperature accuracy. A Linkam HFSX350 heating stage was used, magnesium oxide powder was used for temperature calibration, and the experiment were performed with the beam path under vacuum. To fulfil the Bragg condition for the (200) peak, the heating stage was mounted at a 22° angle to the incident X-ray beam. The sample to detector distance was calibrated using LaB6 powder and data were integrated using SAXSGUI software. For this configuration, correcting for the significant thermal dilatation of the sample stage was not possible, and as such lattice parameter determination was not conducted. The results were only used to monitor changes in diffraction peak shapes as a function of temperature, focusing on the increase in peak intensity. Additionally, texture analysis of the AuNRs supported on glass was performed with a D8 Discover (Bruker) equipped with a Cu X-ray source, a compact Eulerian cradle (Phi, Z, Chi), and an Eiger 2D photon counting detector. The samples were aligned in the X-ray beam and diffraction patterns recorded with varying Phi and Chi, up to 80°.

3.4.2 Near-infrared laser heating

In **Paper I**, two populations of gold nanorods were studied, with average aspect ratios of 3.9 (AuNR 3.9) and 4.4 (AuNR 4.4). Glass substrates were used as support, and three different types of solid-supported gold nanorod samples were prepared: (i) AuNR 3.9 with a surface coverage of 11% (AuNR 3.9 11%), (ii) AuNR 3.9 with a surface coverage of 13% (AuNR 3.9 13%), and (iii) AuNR 4.4 with a surface coverage of 11% (AuNR 4.4 11%). The three sample types were studied to investigate the influence of nanorod morphology and collective heating effects on the photothermal properties. The *in situ* NIR laser heating experiments were performed with the same D8 Discover diffractometer as used in the texture analysis, with the

NIR laser placed inside the enclosure of the instrument. The support stage was designed to ensure the NIR beam was not heating any other elements in the vicinity of the sample. The sample was placed on two 0.5 mm glass capillaries and aligned with the X-ray beam. The NIR laser's collimator was placed 10 cm away from the sample at a 90° angle, ensuring the entire sample was illuminated with comparable flux between experiments. An illustration of the experimental configuration is shown in Figure 7.

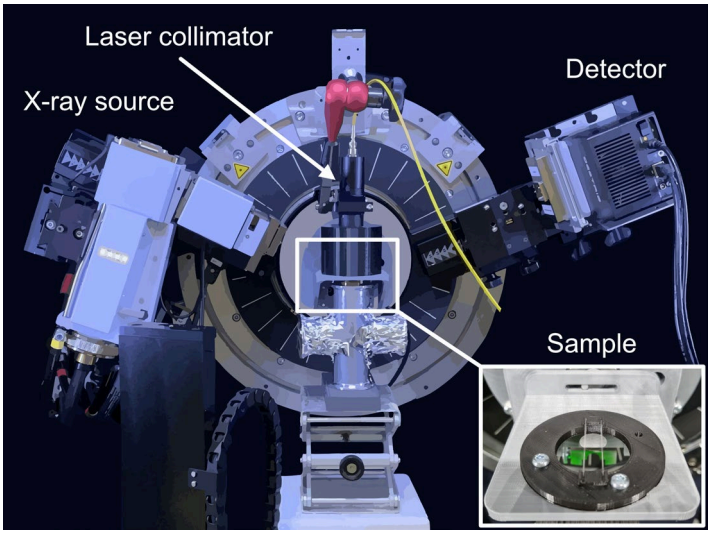


Figure 7. Illustration of the experimental setup used for the *in situ* XRD NIR laser experiments in **Paper I**. The inserted picture shows a sample placed on the support stage comprised of two glass capillaries, ensuring only the sample was heated by the NIR laser beam. Reused with permission from reference (95), licensed under CC-BY 4.0.

In **Paper II**, the photothermal properties of the gold nanorod gradient surfaces were evaluated with *in situ* XRD. The experiments were performed on the same SaxsLab Mat:Nordic instrument as used in the furnace heating experiments. However, for this configuration, part of the X-ray beam was evacuated during the measurements to reduce air scattering and increase signal quality, whereas the sample was kept under dry nitrogen atmosphere. The incident angle was set to 22° and the detector was positioned at 44° to obtain maximum signal from the solid-supported nanorods that are oriented with reference to the substrate, as demonstrated in **Paper I**. A gold nanorod gradient prepared with a withdrawal rate of 0.15 mm min^{-1} was positioned at an incident angle of 22° with reference to the X-ray beam, using a capillary mount, and the NIR laser collimator was placed at a 15 mm distance from the sample surface, producing a laser spot size of approximately 2 mm in diameter. The X-ray beam was set to 2 mm x 2 mm, which with the sample tilted at 22° corresponded to a probed area of 2 mm along the length of the gradient, and 5.3 mm along the width. Measurements were performed at four positions along the gradient: 9, 12, 15 and 18 mm. At each position, XRD patterns were recorded at room temperature and under consecutive NIR irradiation at increasing intensity: 28, 56, 84, and 112 W cm^{-2}. To ensure sufficient signal-to-noise ratio at each position, the exposure times were adjusted to 600 s, 420 s, 300 s, and 180 s for position 9, 12, 15, and 18 mm, respectively. The acquired data were processed using SAXSGUI software, and peak intensity as well as lattice parameters were determined by fitting the (200) diffraction peak using TOPAS v6 (Bruker).

3.5 *In vitro* antibacterial activity

The antibacterial activity of the solid-supported gold nanorods, on glass and titanium, under NIR irradiation was evaluated with an *in vitro* agar plate model. In **Paper III**, the antibacterial activity was evaluated against *Staphylococcus aureus* (CCUG 10778), a Gram-positive bacterium commonly found in BAIs,[96] and *Escherichia coli* (CCUG 29300T), a Gram-negative bacterium frequent in catheter-associated urinary tract infections.[97] In **Paper IV** only *S. aureus* was studied. For long-term storage, the bacteria were kept at -80 °C. *S. aureus* or *E. coli* was inoculated in tryptic soy broth (TSB) and incubated at 37 °C until an approximate concentration of 10^8 colony forming units (CFU)/ml, determined by measuring the optical density (OD). The bacterial suspension was diluted with phosphate buffered saline (PBS) to a concentration of 10^4-10^5 CFU/ml. The bacterial concentration was optimized to the experimental protocol and adapted according to the bacterial strain used. For the AMP-treated samples in **Paper IV**, a bacterial suspension was prepared in the equivalent manner, with the supplement of 3.125 µM of the RRP9W4N AMP (RRPRPRPRPWWWW-NH2, M_W = 1930 g mol^{-1}, purity > 90%, GenScript). The bacterial suspensions were then streaked onto agar plates using cotton swabs.

All samples used in the antibacterial activity evaluation were sterilised by exposure to UV light for 5 min in an UV/O_3-cleaner. Bare glass and titanium substrates were used as controls. The samples were placed onto the agar plates, with the gold nanorods facing the bacteria/agar. They were subsequently irradiated with the NIR laser for 30 s, and at varying intensity. An illustration of the experimental setup is shown in Figure 8. The agar plates were incubated at 37 °C for 16 h, whereafter the number of colonies on each sample were counted. To avoid bacteria growing in from the perimeter of the samples influencing the quantification, colonies on the outmost 1 mm of the samples were excluded. The antibacterial efficacy (in percent) was calculated according to Equation 4.

$$\frac{A - B}{B} \times 100 \tag{4}$$

Where A is the number of colonies per unit area, CFU cm^{-2}, of the control group and B the number of colonies per unit area of the test group. For the *in vitro* antibacterial activity evaluation, all samples were run in triplicates, and the experiments were performed three times (n = 9). Data were expressed as average CFU cm^{-2} values, with standard deviation used to indicate the distribution around the mean. Pairwise two-sample *t*-test assuming unequal variance was used to determine significant differences between sample groups. Significant differences in bar charts are indicated with letters, where two groups with the same letter denote that there is no statistically significant difference between the means, and two groups with different letters denote that there is a statistically significant difference between the means.

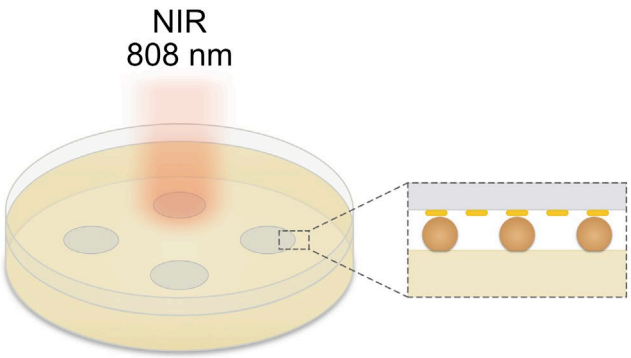


Figure 8. An illustration of the agar plate model used for the *in vitro* antibacterial activity evaluation.

3.6 Bacterial cytological profiling

For the mode of action studies using bacterial cytological profiling in **Paper IV**, the samples were prepared through a modified version of the agar plate model as described for the *in vitro* antibacterial activity evaluation. *S. aureus* (CCUG 10778) was inoculated in TSB and incubated at 37 °C until OD 0.6. From this inoculum, three bacterial suspensions were prepared by dilution with PBS to a final OD of 0.3: one untreated (negative control), one with 3.125 µM RRP9W4N AMP, and one with 10 µM nisin (positive control). Nisin is a pore-forming lantibiotic and was used as a positive control in the assay. The three bacterial suspensions were incubated for 10 min and then spread onto separate agar plates. The solid-supported AuNR samples were placed onto the plates, with the nanorods facing the bacteria. Half of the samples were irradiated with the NIR laser at 4.7 W cm^{-2} for 30 s, whereafter all samples were removed from the plates. From the area beneath each sample, circular agar punches were cut out and used to transfer the bacterial cells to 1.2% agarose patches containing 10% MHB, DAPI (0.2 µg ml^{-1}), SytoxGreen (40 nM), FM4-64 (0.2 µg ml^{-1}), and $DiSC_35$ (0.1 µM).

The agarose patches were thereafter sealed with poly-L-dopamine-coated coverslips and immediately imaged using a Nikon Eclipse Ti2 equipped with a photometrics PRIME BSI camera, a CFI Plan Apochromat DM lambda 100x oil objective (N.A. 1.45, W.D. 0.13 mm), a Lumencor Sola SE II FISH 365 light source, and an Okolab temperature chamber set to 37 °C. The NIS elements AR software version 5.21.03 was used to obtain images. The BCP experiments were performed in three independent biological replicates (two for nisin). Fluorescence intensity parameters were analyzed by using the ImageJ plugin MicrobeJ.[98] Cells were detected in the phase contrast by using the fit shape detection in connection with the circle settings. The area was adjusted to 0.5 to max, all other parameters remained at default settings. Statistical significance was determined with a one-way nested ANOVA.

4. Results and discussion

4.1 Material characterisation

4.1.1 Gold nanorods

The gold nanorods used in the different studies were synthesised with silver nitrate and ascorbic acid concentrations between 8-11 mM and 90-110 mM, respectively. By adjusting the concentration of silver nitrate and ascorbic acid, the aspect ratios of the gold nanorods were tuned, achieving populations with longitudinal resonance peaks between 830-870 nm. In Figure 9, Vis-NIR spectroscopy and TEM characterisation data for the gold nanorods studied in **Paper I** are shown. The dimensions of these two AuNR populations were determined from TEM micrographs, by measuring 400 particles of each type, with results shown in Table 1. The average aspect ratios were determined to be 3.9 and 4.4. The gold nanorods with aspect ratio 3.9 (AuNR 3.9) had a longitudinal LSPR peak at 830 nm, and for the nanorods with aspect ratio 4.4 (AuNR 4.4) the peak was red-shifted to 850 nm (Figure 9A). The high relative intensity of the longitudinal resonance peak compared to the transverse indicates a high shape purity of the synthesised AuNRs.[99] TEM analysis (Figure 9B and 7C) revealed that the AuNR 3.9 exhibited a more dumbbell-shaped morphology compared to the straighter AuNR 4.4. In the growth process of gold nanorods, this dumbbell-shape has been noted at an earlier stage, before reshaping into straight nanorods later in the synthesis.[23,100] The observed morphological differences were therefore attributed to the nanoparticle growth being arrested at different stages of the growth process.

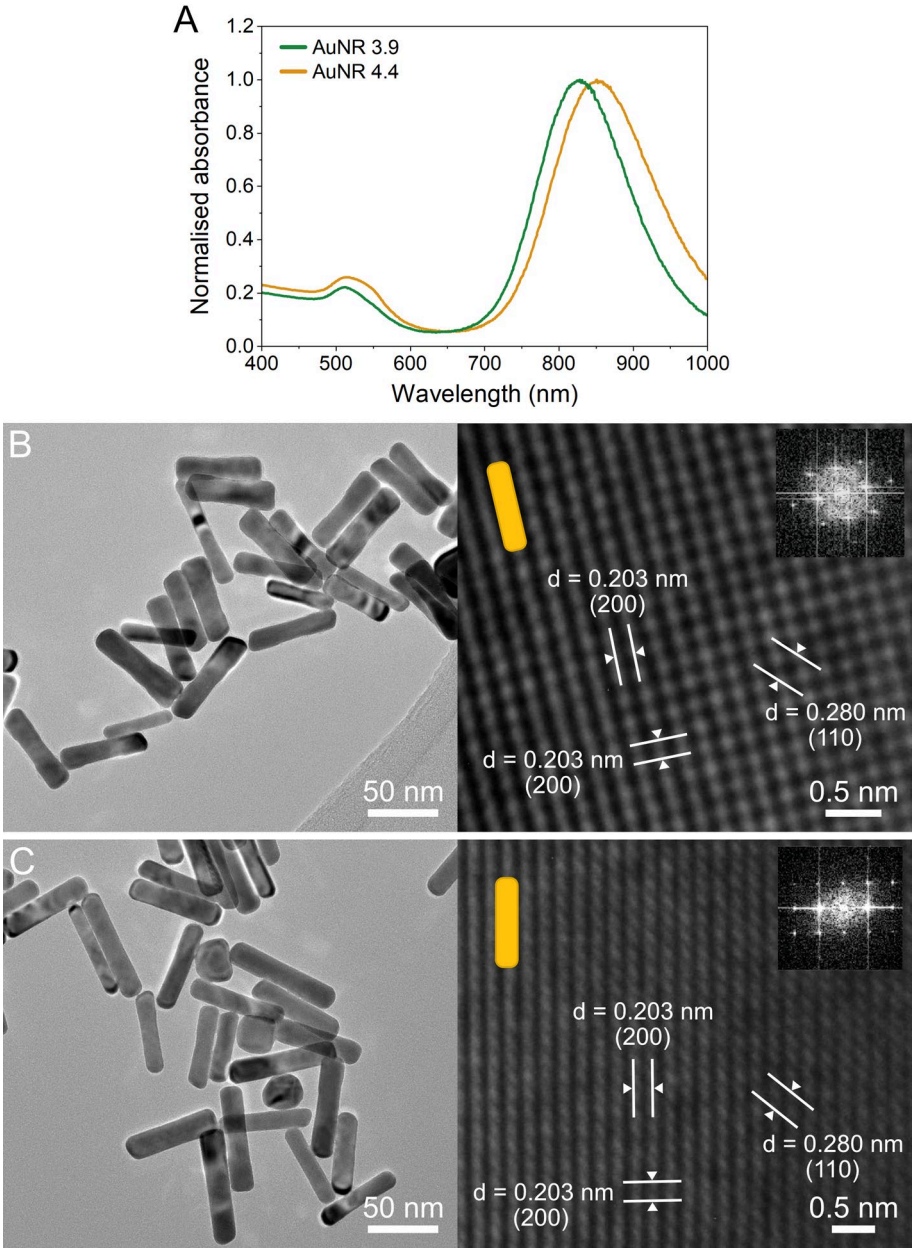


Figure 9. Characterisation of gold nanorods. (A) Normalised Vis-NIR absorption spectra of two different populations of AuNRs, with average aspect ratios of 3.9 and 4.4, respectively. Overview and high-resolution TEM micrographs of (B) the 3.9 aspect ratio AuNRs, and (C) the 4.4 aspect ratio AuNRs. The high-resolution TEM micrographs include FFT inserts and have the gold lattice spacings indicated. Adapted with permission from reference (95), licensed under CC-BY 4.0.

In the high-resolution TEM micrographs in Figure 9, the gold nanorods' face centred cubic, single-crystalline structure can be observed. The spacing of the lattice fringes agrees with the (200) crystal planes in gold (0.203 nm), in parallel with and perpendicular to the growth direction of the nanorods. Spacings in reasonable agreement with the (110) crystal planes (0.287 nm) could also be noted. The crystal structure of the gold nanorods aligns with literature regarding gold nanorods synthesised in the presence of silver.[101]

Table 1. Gold nanorod dimensions in terms of length, width, and aspect ratio (length/width), determined from image analysis of TEM micrographs, measuring 400 particles of each population. The dimensions are presented as average ± standard deviation.

	Length (nm)	Width (nm)	Aspect ratio
AuNR 3.9	67.2 ± 6.9	17.6 ± 2.1	3.9 ± 0.5
AuNR 4.4	66.0 ± 9.7	15.1 ± 2.1	4.4 ± 0.7

The surface charge of the gold nanorods was assessed with electrophoretic light scattering in **Paper III**. The electrophoretic mobility of the nanorods was determined as 4.1 µm·cm/Vs, and from the electrophoretic mobility the zeta potential was calculated to be 52.9 mV, using the Smoluchowski approximation. For the CTAB-stabilised gold nanorods, a positive zeta potential is expected, owing to the quaternary ammonium head group of the stabilising ligand. Additionally, the magnitude of the zeta potential indicates a sufficient colloidal stability.

4.1.2 Solid-supported gold nanorods

The primary surface-attachment method used to fabricate the solid-supported gold nanorod materials relied on electrostatic interactions between the cationic nanoparticles and an anionic support surface (glass or titanium). In Figure 10, some typical characterisation of the solid-supported AuNRs is shown. The optical properties of the AuNRs on glass (Glass-AuNR) were studied by recording the Vis-NIR absorption spectra with the sample in air as well as immersed in water (Figure 10A). The presence of the characteristic transverse and longitudinal resonance peaks showed that the AuNRs retained their plasmonic properties once supported on glass. For the Glass-AuNR in air the longitudinal resonance peak appeared at 750 nm, whereas in water the peak was at 840 nm. This almost 100 nm shift in the peak position is caused by the difference in refractive index surrounding the solid-supported AuNRs, transitioning from the glass-air interface to the glass-water interface.

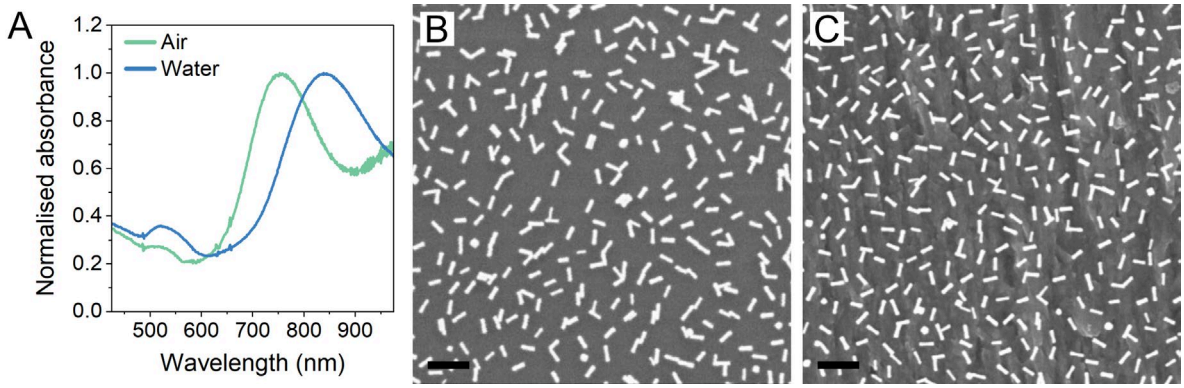


Figure 10. Characterisation of solid-supported gold nanorods. (A) Vis-NIR absorption spectra of Glass-AuNR, measured in air and with the sample immersed in water, highlighting the LSPR peak shift caused by the difference in refractive index of the medium surrounding the AuNRs. SEM micrographs of (A) Glass-AuNR and (B) Ti-AuNR. Scale bars are 200 nm.

SEM micrographs of the AuNRs supported on glass and titanium are shown in Figure 10B and 10C, respectively. The electrostatic surface-attachment procedures yielded even and well-defined coverage of AuNRs on both materials, with the nanoparticles attached individually or in small clusters. The surface coverages studied in this thesis, determined by image analysis of SEM micrographs as the projected area covered by nanorods, ranged between 10-15%. The surface-attachment of gold nanorods has commonly been achieved by initial cleaning or pre-treatment of the substrate, followed by functionalisation with linking molecules such as 3-MPS,[27,63,65] APTES followed by PSS,[64] or ethylene diamine,[66] prior to AuNR immobilisation. The procedures developed in **Paper III** showed that AuNR surface-attachment can be achieved in a reproducible manner on glass and titanium, without the requirement of linking agents. For biomaterial applications, it is desirable to retain the innate surface chemistry of the material as it commonly is designed to interact favourable with the biological environment in which it will be used. As such, avoiding the use of linking agents in the AuNR surface-attachment procedure is favourable, with the additional benefit of simplifying the material preparation protocol.

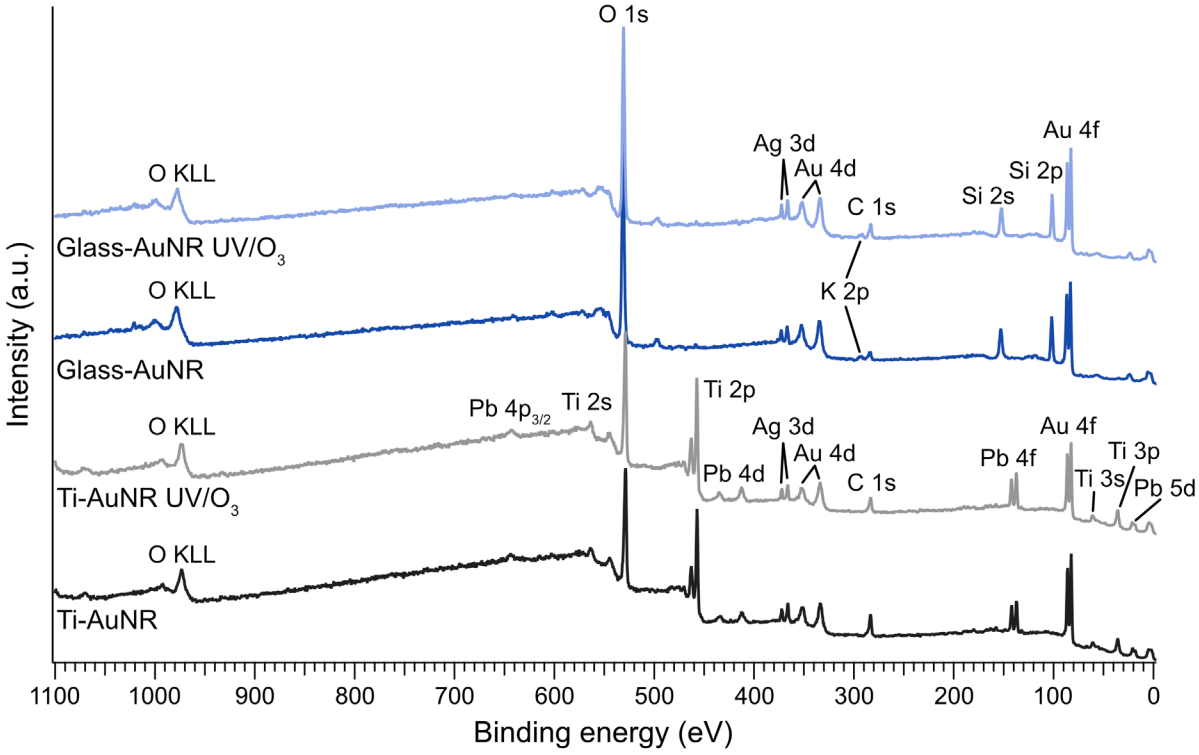


Figure 11. X-ray photoelectron spectroscopy (XPS) survey spectra of untreated and UV/O_3-treated Glass-AuNR and Ti-AuNR, showing the surface elemental composition of the samples. Adapted with permission from reference (102), licensed under CC-BY 4.0.

To characterise the surface elemental composition of the Glass-AuNR and Ti-AuNR, XPS analysis was performed in **Paper III**. Survey spectra of the untreated and UV/O_3-treated Glass-AuNR and Ti-AuNR samples are shown in Figure 11, and the quantified elemental composition is shown in Table 2. The XPS investigations confirmed that the AuNRs constituted a minor fraction of the materials' surfaces. This finding, also apparent from the SEM characterisation, was indicated by the low atomic concentration of gold and silver present. That the surface-attachment of AuNRs resulted in only minor alteration of the surface chemical composition of

the substrate shows the potential of this material modification as a strategy that minimised the impact on the innate surface chemistry of the biomaterial. Additionally, XPS revealed that the UV/O_3-treatment resulted in a decrease in the carbon content of the samples (Table 2), indicating removal of CTAB from the solid-supported AuNRs, an important step towards promoting biocompatibility.

Table 2. Surface chemical composition in atomic percent, determined with XPS, for untreated and UV/O_3-treated Glass-AuNR and Ti-AuNR.

	Atomic concentration %						
	C 1s	O 1s	Si 2p	Ti 2p	Br 3d	Ag 3d	Au 4f
Glass-AuNR	10.6	62.0	22.5		0.31	0.82	3.75
Glass-AuNR UV/O_3	7.1	64.3	23.8		0.29	0.80	3.75
Ti-AuNR	23.5	53.7		17.2	0.37	0.97	4.31
Ti-AuNR UV/O_3	16.1	59.4		19.7	0.29	0.87	3.75

4.1.3 Gold nanorod gradient surfaces

The properties of solid-supported gold nanorods are influenced by their arrangement on the support and the interparticle interactions, thus, controlling the nanoparticle surface-attachment is essential in material development and optimization. In **Paper II**, a method for the preparation of gold nanorod gradient surfaces was developed, enabling evaluation and optimisation of the material properties as a function of nanorod surface coverage. The gold nanorod gradient surfaces were prepared by vertically immersing a 3-MPS functionalised fused silica substrate (9 mm x 20 mm) in a gold nanorod suspension and then withdrawing the suspension at a fixed rate. In this setup, nanoparticle adsorption kinetics were utilised for controlling the surface coverage of AuNRs on the support, yielding a gradient surface where the coverage increased from the top to the bottom of the substrate (Figure 5). Two different withdrawal rates were employed, 0.15 and 0.30 mm min^{-1}, to tune the gradient dynamics, wherein a higher withdrawal rate generated a gradient with an overall lower surface coverage.

To assess how the AuNR surface coverage varied with the distance along the substrate, SEM micrographs were acquired every millimetre along the length of the gradients. In Figure 12A and 12B, composite images of one 0.15 mm min^{-1} and one 0.30 mm min^{-1} gradient are shown, respectively. In the composite images, an increase in the number density of AuNRs can be noted, from the top part of the substrate (left in Figure 12), that was exposed to the nanorod suspension for the shortest amount of time, to the bottom part (right in Figure 12), that was exposed for the longest time. At the low-coverage end of the gradients, the AuNRs were attached almost solely as individual particles, whereas at the high-coverage end some clustering could be noted.

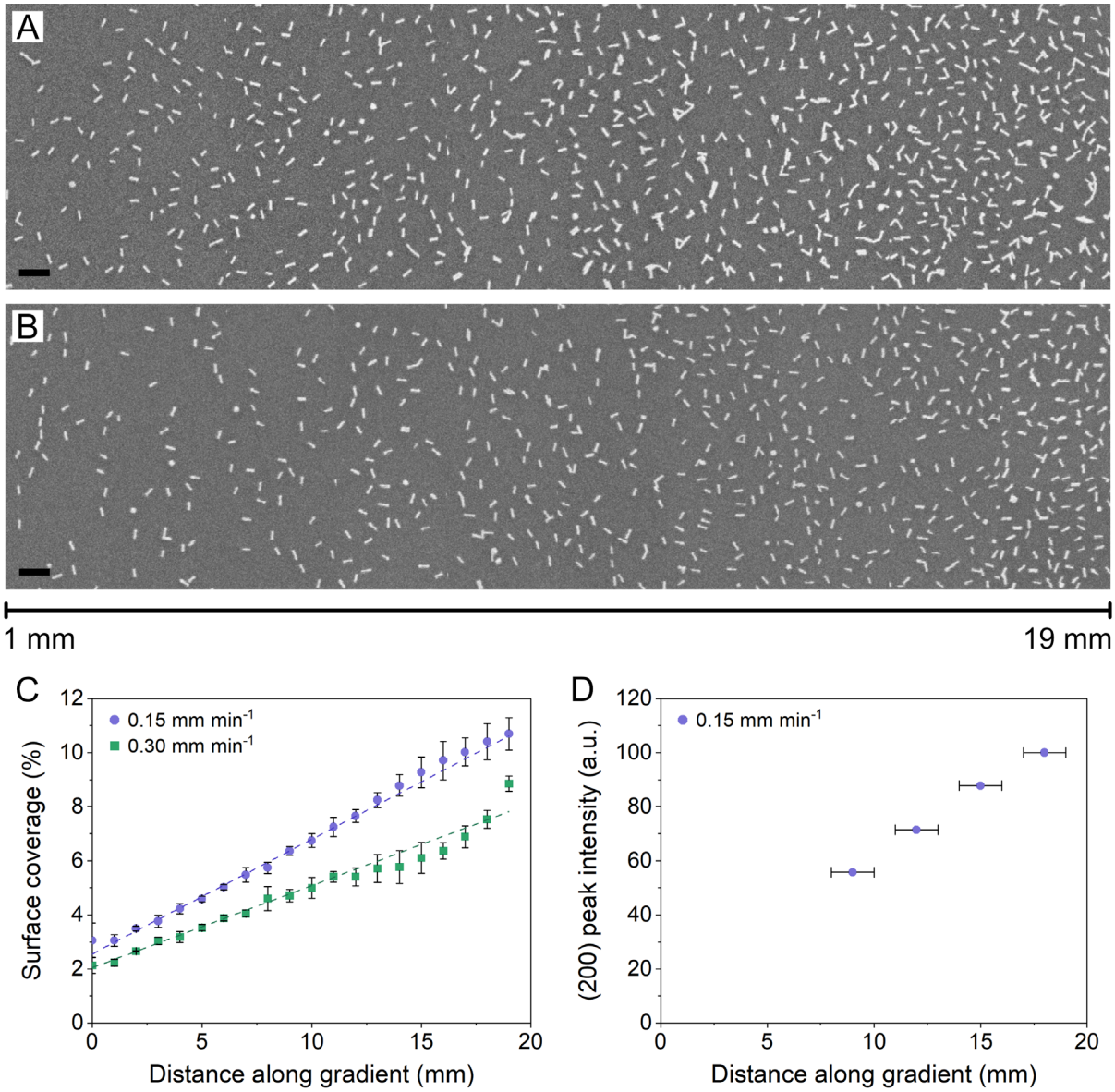


Figure 12. Characterisation of gold nanorod gradient surfaces. Composite images of SEM micrographs acquired every 1 mm along the length of the gradient for (A) one sample prepared with a withdrawal rate of 0.15 mm min^{-1}, and (B) one sample prepared with a withdrawal rate of 0.30 mm min^{-1}. The scale bars are 200 nm. (C) Surface coverage of gold nanorods (projected area) in percent as a function of distance along the gradient in millimetres for the 0.15 and 0.30 mm min^{-1} gradients (n = 4). Error bars indicate standard deviations and the dashed lines linear regressions fitted to the experimental data: $y = 0.424x + 2.55$ ($R^2 = 0.995$) for 0.15 mm min^{-1} and $y = 0.304x + 2.04$ ($R^2 = 0.986$) for 0.30 mm min^{-1}. (D) Intensity of the (200) diffraction peak as a function of distance along one 0.15 mm min^{-1} gradient. The horizontal bars indicate the 2 mm region probed by the X-ray beam.

The surface coverage of AuNRs as a function of distance along the gradients was determined by image analysis of SEM micrographs, as the projected area covered by nanoparticles (in percent). In Figure 12C, the average surface coverage of four individual samples (n = 4) each of the 0.15 mm min^{-1} and the 0.30 mm min^{-1} as a function of distance is shown. The error bars denote the standard deviation and the dashed lines the linear regressions fitted to the

experimental data. The surface coverage exhibited a linear increase with the distance along the gradients for both withdrawal rates. For the 0.15 mm min^{-1} samples, the surface coverage ranged between 3% to 11%, and for the 0.30 mm min^{-1} the range was 2% to 9%. The difference in surface coverage between the 0.15 mm min^{-1} and 0.30 mm min^{-1} samples shows how the gradient dynamics could be tuned by adjusting the withdrawal rate of the AuNR suspension, allowing for ease of control over the overall surface coverage of nanoparticles in the preparation process. By collecting XRD patterns along the gradient, the surface coverage could also be related to the scattering intensity of the (200) diffraction peak. Over the 9-18 mm range of a 0.15 mm min^{-1} gradient, diffraction patterns were acquired every 3 mm using identical exposure settings. The diffraction peaks were fitted and the scattering intensity at each measured area as a function of the position is shown in Figure 12D. The (200) peak intensity exhibited a linear increase with the distance along the gradient, agreeing with the increase in surface coverage determined by image analysis of SEM micrographs.

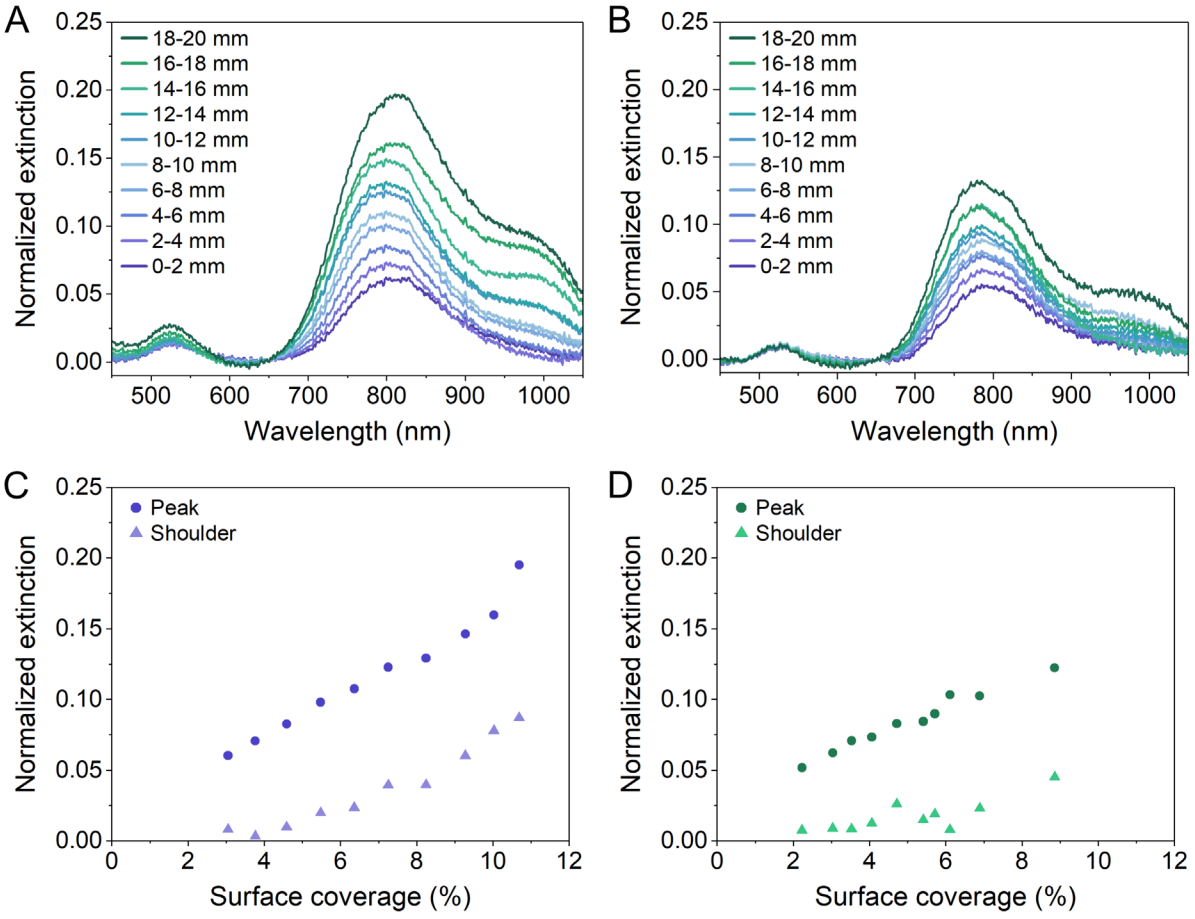


Figure 13. Normalised extinction spectra acquired at 2 mm intervals along the gradient for (A) a 0.15 mm min^{-1} sample, and (B) a 0.30 mm min^{-1} sample. Extinction peak intensity (average extinction between 800-820 nm) and shoulder intensity (average extinction between 990-1010 nm) as a function of surface coverage of gold nanorods for (C) a 0.15 mm min^{-1} gradient, and (D) a 0.30 mm min^{-1} gradient.

The gold nanorod gradient surfaces' optical properties were studied by acquiring extinction spectra in air at 2 mm intervals along the samples. Representative spectra, baseline normalised to 650 nm, for a 0.15 mm min^{-1} and a 0.30 mm min^{-1} sample are shown in Figure 13A and 13B, respectively. The extinction intensity of the longitudinal resonance peak, centred around 800 nm, increased with the distance along the gradient for both withdrawal rates. Figure 13C and 13D show the longitudinal peak intensity, determined as the average extinction between 800-820 nm, as a function of surface coverage of AuNRs for the 0.15 mm min^{-1} and the 0.30 mm min^{-1} samples, respectively. For both sample types, the peak intensity exhibited an approximately linear increase with surface coverage.

Further into the NIR region, around 1000 nm, the appearance of a shoulder on the longitudinal peak could be observed as the surface coverage of AuNRs increased. The shoulder intensity, determined as the average extinction between 990-1010 nm, as a function of surface coverage are shown in Figure 13C and 13D for the 0.15 mm min^{-1} and the 0.30 mm min^{-1} gradients, respectively. At surface coverages above 8%, an increase in the shoulder intensity could be noted. The increase in shoulder intensity that accompanied the increase in surface coverage was attributed to plasmon coupling between neighbouring AuNRs. A higher surface coverage correlates with a decreased interparticle distance and a larger amount of clustered nanorods, which will induce plasmon coupling between the particles, explaining the observed changes in optical properties.[32] The gold nanorod gradient surfaces could therefore serve as a platform to assess the influence of plasmon coupling as a function of nanorod surface density.

4.2 Evaluation of photothermal properties

4.2.1 Thermal imaging

The macroscopic heating of the solid-supported gold nanorod materials was evaluated with thermal imaging. In **Paper II**, the heating of the gold nanorod gradient surfaces was assessed by monitoring the temperature of the samples under NIR (808 nm) irradiation at 0.6 W cm^{-2}. The samples were resting on glass slides suspended in air, thermal images recorded after 10 s and 50 s irradiation are shown in Figure 14. For both sample types, a gradient in temperature was demonstrated, corresponding to the increase in surface coverage of gold nanorods. After 50 s NIR irradiation, the temperature difference between the low (top) and high (bottom) surface coverage part of the gradients was 2-4 °C. Notably, the 0.15 mm min^{-1} sample reached an overall higher temperature compared to the 0.30 mm min^{-1}, reflecting the difference in surface coverage between the two sample types.

In **Paper III**, the heating of the solid-supported AuNRs on titanium and glass was studied with thermal imaging, conducted with the samples on agar plates to simulate the setup used in the antibacterial activity evaluation. Images were acquired before and after 30 s NIR irradiation and the temperature increase was determined as the difference in temperature at the centre of the samples before and after irradiation. Starting temperatures ranged between 24-25 °C. The average temperature increase (n = 2) of the titanium and glass samples is shown in Figure 15A and 15B, respectively. For the gold nanorods on titanium (Ti-AuNR) a comparable temperature increase to the bare titanium (Ti) was observed, both increasing approximately 28 °C after 30

s irradiation at 20 W cm^{-2}. In contrast, with the gold nanorods on glass (Glass-AuNR), a difference in the temperature increase compared to the bare glass (Glass) was noted. The Glass-AuNR increased approximately 17 °C after 30 s irradiation at 20 W cm^{-2}, compared to barely 3 °C for the Glass. The findings from the thermal imaging hence showed that the photothermal heating of the AuNRs was discernible with the particles supported on glass, but not on titanium.

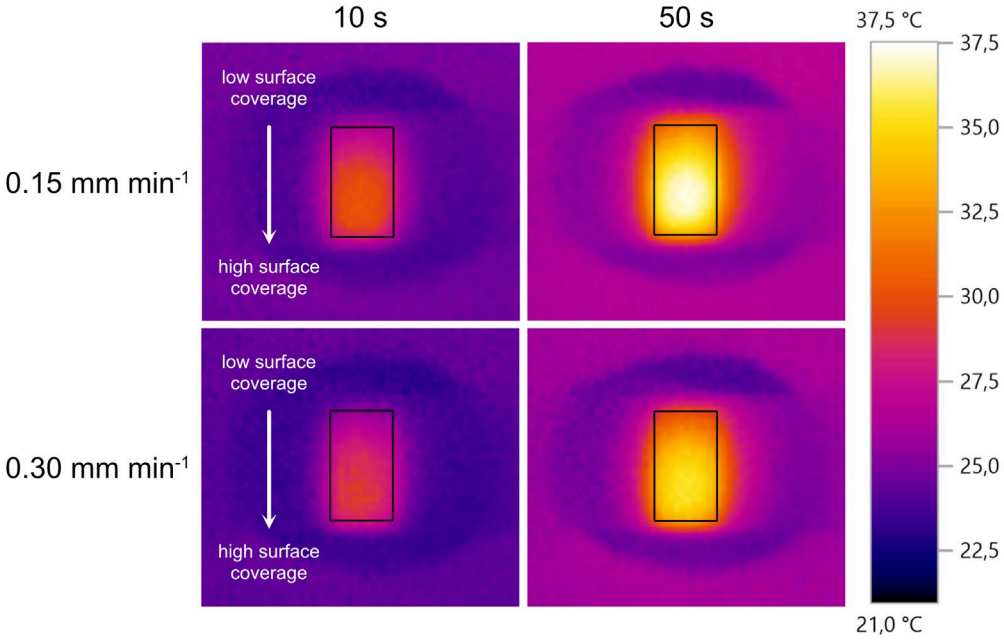


Figure 14. Thermal images of gold nanorod gradient surfaces prepared with a withdrawal rate of 0.15 mm min^{-1} (top) and 0.30 mm min^{-1} (bottom) during NIR irradiation at an intensity of 0.6 W cm^{-2}. The black rectangular outlines indicate the gradient samples, oriented so that the surface coverage of gold nanorod increases from top to bottom.

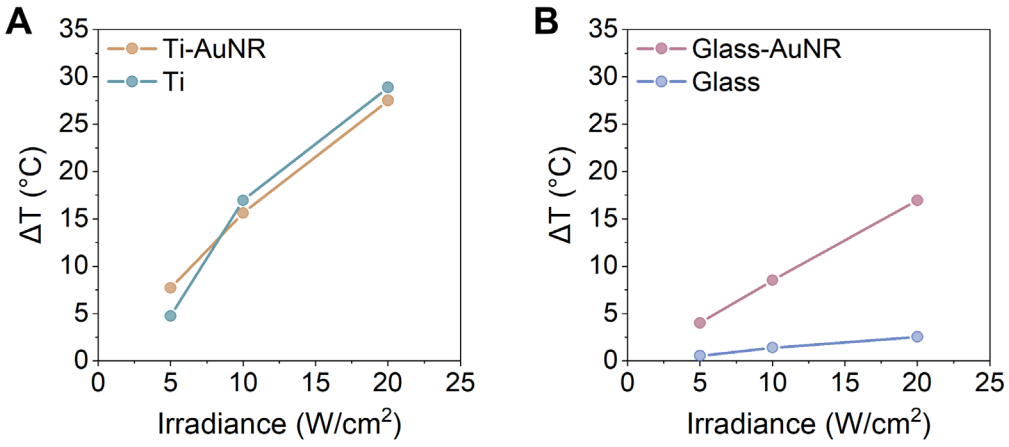


Figure 15. Temperature increase as a function of NIR laser intensity determined from thermal imaging for (A) Ti and Ti-AuNR, and (B) Glass and Glass-AuNR. Thermal imaging was conducted with the samples placed on agar plates and the temperature increase was determined as the difference in temperature at the centre of the samples before and after 30 s irradiation. Reused with permission from reference (102), licensed under CC-BY 4.0.

4.2.2 *In situ* X-ray diffraction

In **Paper I**, two different populations of gold nanorods were studied, with average aspect ratios of 3.9 (AuNR 3.9) and 4.4 (AuNR 4.4). To investigate the influence of both AuNR morphology and collective heating effects on the photothermal properties, three different sample types of solid-supported AuNRs on glass were prepared: (i) AuNR 3.9 at a surface coverage of 11% (AuNR 3.9 11%), (ii) AuNR 3.9 at a surface coverage of 13% (AuNR 3.9 13%), and (iii) AuNR 4.4 at a surface coverage of 11% (AuNR 4.4 11%). In **Paper II**, the photothermal properties of the gold nanorod gradient surfaces were studied with *in situ* XRD, investigating how the heating of the nanorods was influenced by the surface coverage.

4.2.2.1 Furnace heating and texture analysis

In the Bragg-Brentano scans of the flat-mounted solid-supported AuNR samples, shown in Figure 16, a broad (200) diffraction peak was observed. The absence of a (111) peak in the diffraction patterns demonstrates the strong orientation of the supported AuNRs. Detailed texture analysis performed using an Eulerian cradle stage revealed that the majority of the nanorods were single crystals with the (200) plane parallel to the long axis, which corroborated the findings from TEM characterisation (Figure 9), and that they were oriented with the long axis towards the glass support. This orientation was also confirmed in SEM micrographs of the solid-supported AuNRs (Figure 10).

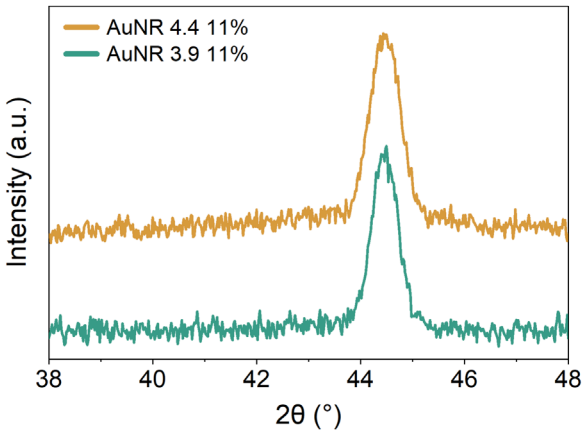


Figure 16. XRD patterns of untreated, flat-mounted AuNR 3.9 11% and AuNR 4.4 11%, with broad (200) peaks from the supported, single crystal gold nanorods. Adapted with permission from reference (95), licensed under CC-BY 4.0.

A series of furnace heating experiments was performed to determine the thermal expansion coefficient of the supported AuNRs, and to study how the nanoparticle morphology was affected by conventional heating. In Figure 17A, the evolution of the (200) diffraction peak during the furnace heating for AuNR 4.4 11% is shown, where a peak shift towards lower 2θ-angles with increasing temperature can be noted, caused by the thermal expansion of the AuNRs. From the position of the (200) peak, the lattice parameter as a function of temperature was determined for AuNR 3.9 11% and AuNR 4.4 11%, shown in Figure 17B. The bulk lattice parameter was calculated using the thermal expansion coefficient for gold (Equation 5).[103] In

the considered temperature range, the thermal expansion coefficient of the AuNRs appeared to be like those reported in literature for bulk gold, within the limits of instrumental resolution.

$$\alpha_{gold}(T) \times 10^6 = 12.00269 + 0.00953T - (8.4 \times 10^{-6})T^2 + (5.43 \times 10^{-9})T^2 \qquad (5)$$

The evolution of the full width at half-maximum (FWHM) of the (200) peak for AuNR 4.4 11% is also shown in Figure 17B. The FWHM was used as a probe for morphological changes in the supported AuNRs, wherein a decrease in FWHM marks the onset of morphology transformations. Until around 120°C, the evolution of the (200) diffraction peak during heating corresponded purely to thermal expansion of the AuNRs. At temperatures above 120 °C, morphological transformations were observed, manifesting as irreversible modification of the diffraction peak's shape, with a sharp decrease in the FWHM. In the complementary series furnace heating measurements performed with a Linkam heating cell, the evolution of the diffraction peak shapes was noted to continue until at least 250 °C.

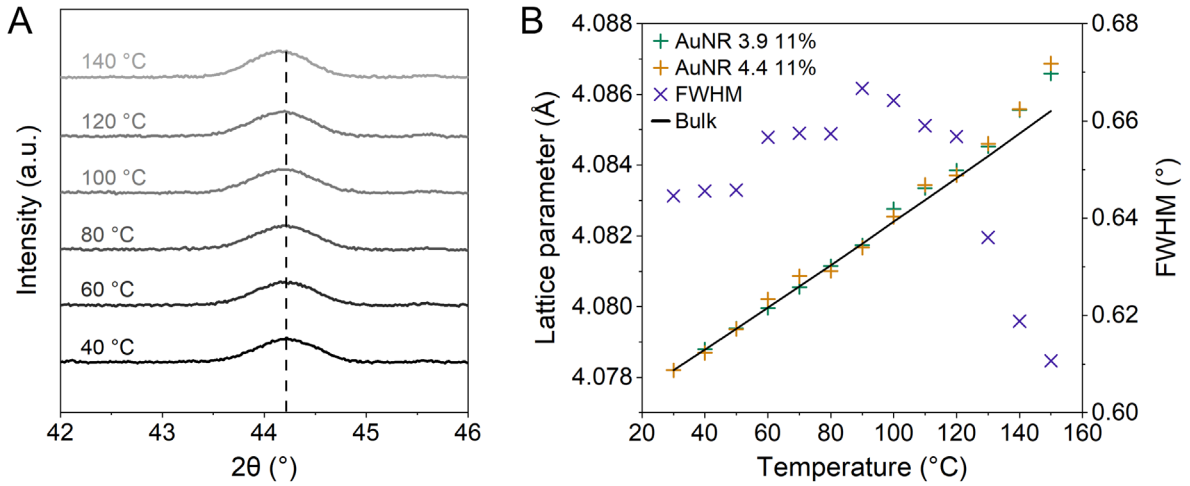


Figure 17. (A) Evolution of the (200) diffraction peak during furnace heating for AuNR 4.4 11%. (B) Lattice parameter of the gold cubic structure for AuNR 3.9 11% and AuNR 4.4 11%, along with the full width at half-maximum (FWHM) for AuNR 4.4 11%, as a function of temperature. The solid black line represents the thermal expansion of bulk gold. Reused with permission from reference (95), licensed under CC-BY 4.0.

Post-experiment characterisation of the samples heated to 250 °C, shown for AuNR 3.9 11% in Figure 19, revealed an aspect ratio decrease of individual nanorods and a coalescence of AuNR clusters into rounded structures. Pronounced changes in the optical properties accompanied the morphological transformations, inducing a blue-shift of the longitudinal resonance peak. A continued absence of the (111) diffraction peak after furnace heating to 250 °C showed that the crystallite orientation of the solid-supported AuNRs was not affected by the heating-induced morphology transformations. This suggests that the crystalline core of the nanorods was conserved, serving as a nucleus for reorganisation of outer layers, as demonstrated in a molecular dynamics study of similar systems.[104]

4.2.2.2 Near-infrared laser heating

During the *in situ* NIR laser heating experiments in **Paper I**, the solid-supported AuNR samples were irradiated with continuous NIR light at varying power levels up to 24 W, and the thermal expansion of the AuNRs, causing a shift of the (200) diffraction peak to lower angles, was monitored. From comparing the measured lattice expansion for the nanorods to literature values for bulk gold (Figure 17B), a relationship between the NIR laser intensity and the temperature of the nanoparticles for the AuNR 3.9 11%, AuNR 3.9 13%, and AuNR 4.4 11%, was established (Figure 18A). A linear temperature increase with laser power was noted for the supported AuNRs, aligning with the model for heating of plasmonic nanoparticle arrays (Equation 2), until the onset of morphological transformation around 120 °C. The slope of the temperature-power plots in Figure 18A increased with the surface coverage of AuNRs, wherein a 1.4-fold augmentation of the attained temperature at a given power level was attained upon increasing the surface coverage of AuNR 3.9 from 11% to 13%. No significant differences were discerned regarding the temperature reached for a set power between the two AuNR populations studied. By estimating the relative contribution of the self-temperature increase of a nanoparticle to the external temperature increase from the surrounding nanoparticles in the dimensionless parameter ζ_2 (Equation 1), it was revealed that collective heating effects were predicted to dominate the temperature increase for the solid-supported AuNR systems studied. This aligns with the observation that an increased surface coverage resulted in a higher AuNR temperature, and could be part of the reason as to why no differences between the AuNR 3.9 11% and AuNR 4.4 11% samples were noted.

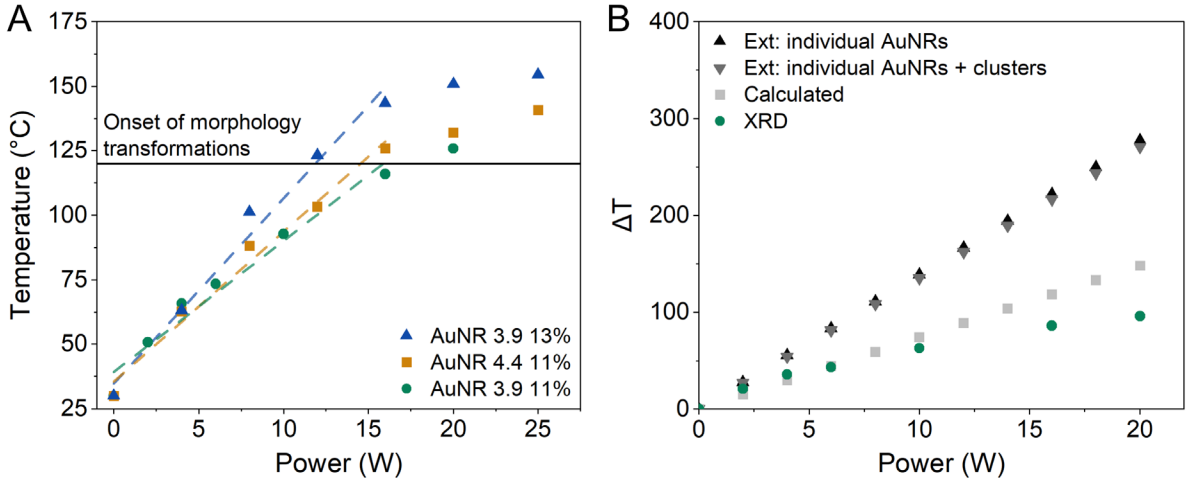


Figure 18. (A) Temperature of the solid-supported gold nanorods as a function of NIR laser power, determined by comparing the measured lattice parameters with the thermal expansion of gold, for samples AuNR 3.9 11%, AuNR 4.4 11%, and AuNR 3.9 13%. Dashed lines indicate linear trends up to 120 °C. (B) Experimentally determined and theoretically modelled (Equation 2) temperature increase as a function of laser power for AuNR 3.9 11%. The absorption cross sections used in the theoretical predictions were determined from calculations based on the AuNR dimensions ("Calculated") or based on extinction spectroscopy measurements assuming either that individual and clustered AuNRs (Ext: individual AuNRs + clusters"), or that only individual AuNRs contribute to the extinction at 808 nm. Reused with permission from reference (95), licensed under CC-BY 4.0.

The findings in Figure 18A show that the employed methodology of monitoring the lattice thermal expansion with XRD not only allows for direct assessment of the gold nanorods' temperature, but also to detect the onset of nanoparticle morphology transformation during NIR light-induced heating. For the supported AuNRs studied in **Paper I**, this onset occurred around 120 °C, noticeable as deviations from the linear temperature-power relationship, and it was accompanied by changes in the nanoparticles' optical properties, shown in the post-experiment Vis-NIR spectroscopy characterisation (Figure 19). The blue-shift of the longitudinal resonance peak, owing to a decrease in nanorod aspect ratio, causes the absorption efficiency at 808 nm to be reduced, eventually preventing further heating of the sample by increasing NIR laser power.

To compare the experimental findings with the model for plasmonic heating of nanoparticle arrays described by Equation 2, an estimation of the absorption cross sections of the AuNRs was needed. This was achieved by (1) calculations based on the nanoparticles' average dimensions, and (2) extinction spectroscopy measurements. From extinction spectroscopy data, cross sections were determined assuming that both individual and clustered AuNRs contribute to the extinction at 808 nm, or that only individual AuNRs contribute. A comparison of the experimentally determined temperature increase with the theoretically predicted (based on Equation 2) for AuNR 3.9 11% is shown in Figure 18B. In the linear temperature-power region, the experimental data aligned with the theoretical predictions using the absorption cross section calculated from the nanorods average dimensions. However, the theoretical predictions using cross sections determined from extinction spectroscopy showed an overestimate of the temperature increase compared to the experimental findings. This discrepancy was attributed to the scattering contribution to the extinction cross sections being greater than what was estimated from the theoretical calculations. Because the theoretical model assumes that the properties of the system are temperature independent, greater deviations from the experimental data were observed upon the onset of morphological transformations in the nanorods.

By comparing the *in situ* XRD data with theoretical predictions, the importance of experimental evaluation of the photothermal properties of solid-supported gold nanorods was emphasised. The systems studied in this thesis, consisting of a size distribution of randomly arranged gold nanorods that exhibit temperature induced morphology transformations, give rise to a complexity that is overlooked by the assumptions made in the theoretical model. In studying the photothermal properties of the supported AuNRs by monitoring the lattice thermal expansion with *in situ* XRD, and corroborating the *in situ* data with SEM and Vis-NIR spectroscopy characterisation, a correlation between the NIR laser power, temperature of the AuNRs, and the onset of morphology transformation could be established.

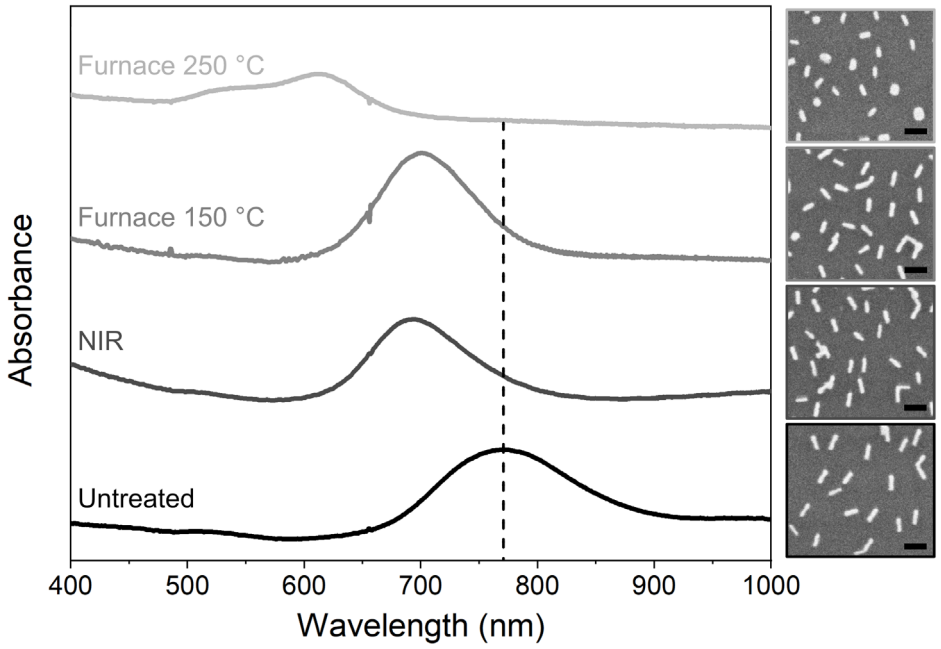


Figure 19. Post-experiment Vis-NIR absorption spectroscopy and SEM characterisation of AuNR 3.9 11%, showing the morphology transformations of the supported AuNRs and the resulting LSPR peak shifts induced by furnace heating or NIR laser irradiation. Scale bars in SEM micrographs are 100 nm. Reused with permission from reference (95), licensed under CC-BY 4.0.

As shown by the findings from **Paper I**, the photothermal properties of the solid-supported AuNRs are governed by collective heating effects, wherein an increased surface coverage of nanoparticles resulted in a higher AuNR temperature for a set laser power (Figure 18A). To further investigate how the AuNR surface coverage influenced the plasmonic heating of these materials, *in situ* XRD studies were also conducted with the gold nanorod gradient surfaces in **Paper II**. In this experimental setup, the X-ray beam probed an area of 2 mm along the length and 5.3 mm along the width of the gradient, and the NIR laser beam had a diameter of approximately 2 mm. As such, at each position a range of ±1 mm along the length of the gradient was probed. For a sample prepared with a withdrawal rate of 0.15 mm min^{-1} (Figure 12) irradiation experiments were conducted at four positions along the gradient: 9, 12, 15 and 18 mm. At each position, diffraction patterns were acquired at room temperature and under consecutive NIR irradiation at 28, 56, 84 and 112 W cm^{-2}.

The shifts of the (200) diffraction peak were used to determine the temperature of the AuNRs, using the methodology developed in **Paper I**. By knowing the surface coverage of nanoparticles at each position along the gradient (Figure 12C), a relationship between the temperature of the nanorods and the surface coverage, at four different laser intensities, were established, shown in Figure 20. An increase in the AuNR temperature along the gradient was demonstrated, highlighting how the heating is governed by the surface coverage, and aligning with the findings from **Paper I**. Under irradiation at 56 W cm^{-2}, the temperature difference between of the nanorods at the lowest probed surface coverage (~ 6%) and the highest (~ 10%) was 50 °C, reaching around 100 °C and 150 °C, respectively.

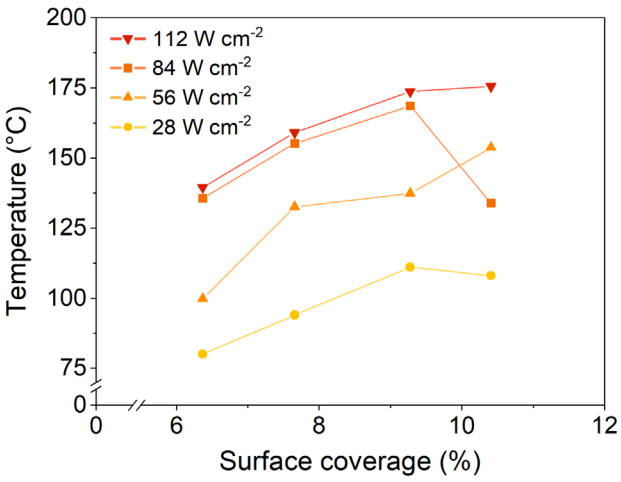


Figure 20. Gold nanorod temperature as a function of surface coverage for a gold nanorod gradient surface prepared with a withdrawal rate of 0.15 mm min^{-1}, at four different NIR laser intensities, determined by *in situ* XRD.

As observed in **Paper I**, the AuNRs undergo morphology transformations (reduced aspect ratio, coalescence of clusters) at elevated temperatures, with an onset around 120 °C. These heating-induced morphological changes were also observed for the gold nanorod gradient surfaces, resulting in a blue-shift of the longitudinal resonance peak after NIR irradiation, shown by post-experiment extinction spectroscopy characterisation (Figure 21). Regions with higher surface coverage of AuNRs reached higher temperatures, which in turn results in more prominent morphology transformations and larger blue-shifts. Since each position was consecutively irradiated with increasing laser intensity, temperatures exceeding the onset of morphology transformations (> 120 °C) were attained already during the 56 W cm^{-2} irradiation at all probed positions, except the lowest coverage (~ 6%). When proceeding the measurements at higher laser intensities, the optical properties of the AuNRs had started to change, and the resonance peak would gradually blue-shift away from the 808 nm excitation, leading to less efficient light absorption and consequently less efficient heating. The positions with 9% and 10% surface coverage reached higher temperatures early in the irradiation sequence, causing the nanorods in these areas to undergo more prominent morphology changes, with larger blue-shifts as a result, validated by the post-experiment characterisation (Figure 21). This explains the deviations from the expected trend of increasing temperature with surface coverage noticeable in Figure 20, wherein the temperature of the higher surface coverage regions instead plateaus or decreased.

Through *in situ* XRD investigations of the plasmonic heating of the gold nanorod gradient surfaces, we demonstrated that the temperature of the nanorods increased with the surface coverage. Owing to the tuneable photothermal properties of the gold nanorod gradient surfaces, these materials show potential as a platform for further studies of plasmonic heating as a function of nanoparticle surface density, which is of particular interest for plasmonic nanoparticle arrays where the temperature is governed by collective heating effects.

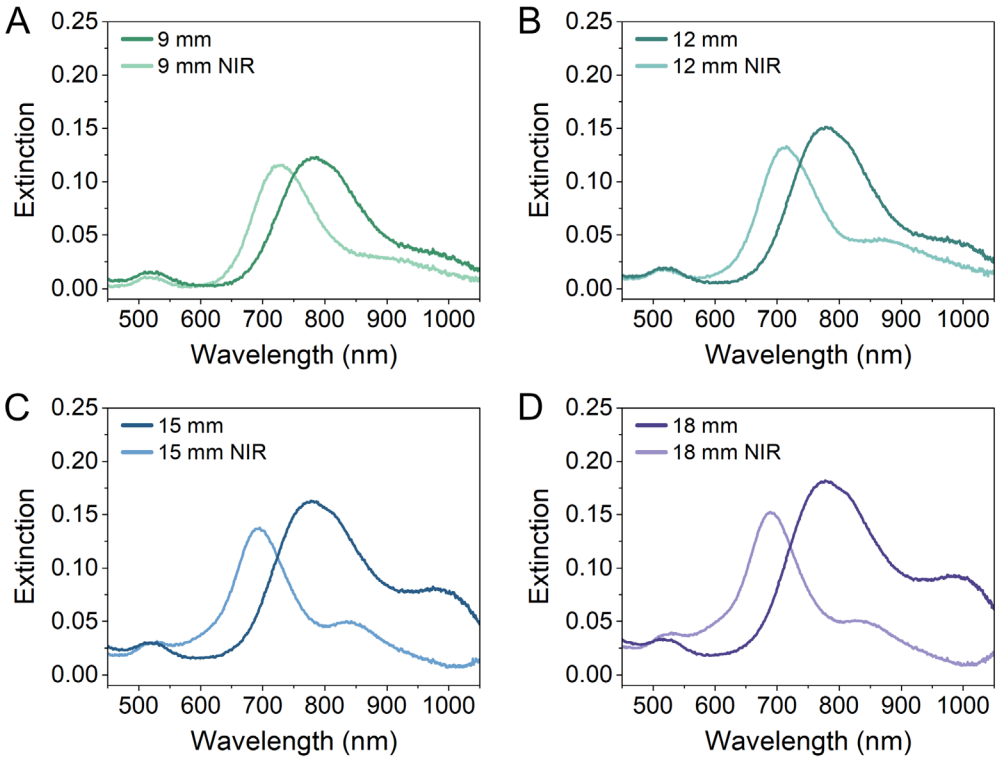


Figure 21. Extinction spectroscopy characterisation of a gold nanorod gradient surface prepared with a withdrawal rate of 0.15 mm min^{-1} post *in situ* XRD measurements. Extinction spectra were recorded of non-irradiated and NIR irradiated areas, at the four different positions probed during XRD: (A) 9 mm (~ 6% surface coverage), (B) 12 mm (~ 8%), (C) 15 mm (~ 9%), and (D) 18 mm (~ 10%).

From the *in situ* XRD studies performed in **Paper I** and **Paper II,** we could construct a detailed picture of the temperature evolution of the gold nanorods and shed light on temperature-induced morphology transformations, which set a threshold on what temperature can be utilised for therapeutic purposes without permanently altering the material properties. Altogether, the findings give valuable insight into the photothermal characteristics of the solid-supported gold nanorods and how they are influenced by NIR light intensity and nanoparticle surface density, critical for their implementation in PPTT applications.

4.3 *In vitro* antibacterial activity

In **Paper III**, the antibacterial activity of the solid-supported gold nanorods on glass and titanium (Glass-AuNR, Ti-AuNR), as a function of NIR light intensity for 30 s irradiation time, was investigated. The average surface coverage of AuNRs on the glass samples was 14%, and on the titanium samples it was 12%. The *in vitro* antibacterial activity was evaluated using an agar plate model, with bare glass and titanium substrates used as controls (Glass, Ti). For the AuNRs on titanium, the antibacterial activity was evaluated against *S. aureus* using two laser intensities: 5 and 10 W cm^{-2}. For AuNRs on glass, the antibacterial activity was evaluated against *S. aureus* using three laser intensities: 5, 10, and 20 W cm^{-2}, and against *E. coli* using an intensity of 20 W cm^{-2}.

At a NIR laser intensity of 10 W cm^{-2}, a significant antibacterial activity against *S. aureus* was demonstrated for both Ti-AuNR and Ti, compared to all other sample groups (Figure 22). The Ti-AuNR and Ti irradiated at 10 W cm^{-2} for 30 s exhibited antibacterial efficacies of 79% and 71%, respectively, compared to the non-irradiated Ti control. However, no significant difference was observed between the NIR irradiated Ti-AuNR and Ti, indicating that with titanium as support, no effect from the photothermal heating of the AuNRs was obtained. As no antibacterial activity was demonstrated for the lower laser intensity evaluated (5 W cm^{-2}), but at a sufficient intensity (10 W cm^{-2}) a significant effect occurred both in the presence and absence of AuNRs, the antibacterial effect could be correlated with the NIR light intensity. The observed antibacterial activity was therefore attributed to heating of the substrate, owing to light absorption by the titanium, which has a high optical extinction coefficient at 808 nm.[105] These findings align with the thermal imaging (Figure 15A), where no obvious difference in temperature increase was noted, and are furthermore supported by the fact that titanium is known to induce plasmon damping.[106] The disruption of the plasmon resonance stems from titanium's dielectric function, as explained in section 2.1.2.1, which, in addition to introducing absorption and influencing the local refractive index, can cause phenomena like substrate-induced damping.

The findings in **Paper III** contrast previous work studying the antibacterial activity of AuNRs on titanium, wherein a significant antibacterial activity from the nanorods was demonstrated upon NIR irradiation.[64] The contradicting results were ascribed to the difference in nanorod density on the materials, where our study evaluated titanium substrates functionalised with discrete AuNRs in a sub-monolayer (~ 12% surface coverage), the referenced work used complete multilayer coatings of AuNRs. By employing a multilayer coating of AuNRs the plasmon damping influence from the titanium substrate can be circumvented, however, disadvantages arise such as entirely changing the surface chemistry of the support and influencing the nanorods' optical properties by introducing plasmon coupling. Importantly, our findings furthermore showed no significant antibacterial effect from the Ti-AuNR in the absence of NIR light.

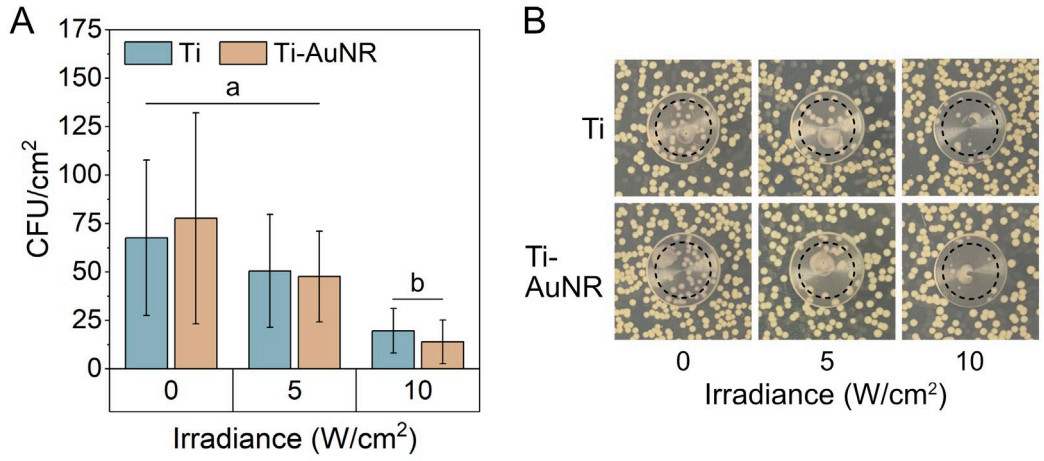


Figure 22. Antibacterial activity against *S. aureus* of Ti-AuNR irradiated with NIR light at different intensities for 30 s (0 = non-irradiated, 5 and 10 W cm^{-2}). (A) Data expressed as average CFU cm^{-2} (n = 9), error bars indicate standard deviations. $p < 0.05$. (B) Example images of samples from the agar plate model, with bacterial colonies appearing as yellow dots and the black dashed circles encircle the sampling area. Reused with permission from reference (102), licensed under CC-BY 4.0.

From the *in vitro* evaluation against *S. aureus*, the solid-supported gold nanorods on glass (Glass-AuNR) demonstrated a significant antibacterial activity upon NIR irradiation at 20 W cm^{-2} for 30 s, compared to all other sample groups (Figure 23A and 23C). The Glass-AuNR irradiated at 20 W cm^{-2} exhibited a 99% antibacterial efficacy compared to the non-irradiated Glass-AuNR and to the Glass irradiated at the same intensity. At the lower laser intensities evaluated, 5 and 10 W cm^{-2}, no significant effect was demonstrated. The antibacterial activity of the Glass-AuNR irradiated at 20 W cm^{-2} was also evaluated against *E. coli* (Figure 23B and 23D), where a significant effect was demonstrated compared to all other sample groups. Against *E. coli*, the antibacterial efficacy was 93% compared to the non-irradiated Glass-AuNR and to the Glass irradiated at the same intensity. The high antibacterial efficacy against both *S. aureus* and *E. coli* shows promise for harnessing the plasmonic heating of AuNRs to obtain a broad-spectrum, light-activated antibacterial surface modification. Additionally, no significant antibacterial activity from the Glass-AuNR in the absence of NIR light was demonstrated against either bacterial strain, aligning with the results from the titanium studies, and indicating that the solid-supported AuNRs did not influence bacterial viability.

With glass as support material, which is transparent to NIR light, a photothermal antibacterial activity originating from plasmonic heating of the AuNRs was established, aligning with the thermal imaging where the Glass-AuNR had a steeper temperature increase with laser intensity compared to the Glass (Figure 15B). The divergence of the origin of the antibacterial activity between glass and titanium as support shows the critical influence of the substrate properties on the bactericidal effect of materials based on solid-supported AuNRs. For utilising the plasmonic heating of the nanoparticles, the modification strategy thus shows greater potential on biomaterials with low optical extinction in the NIR region.

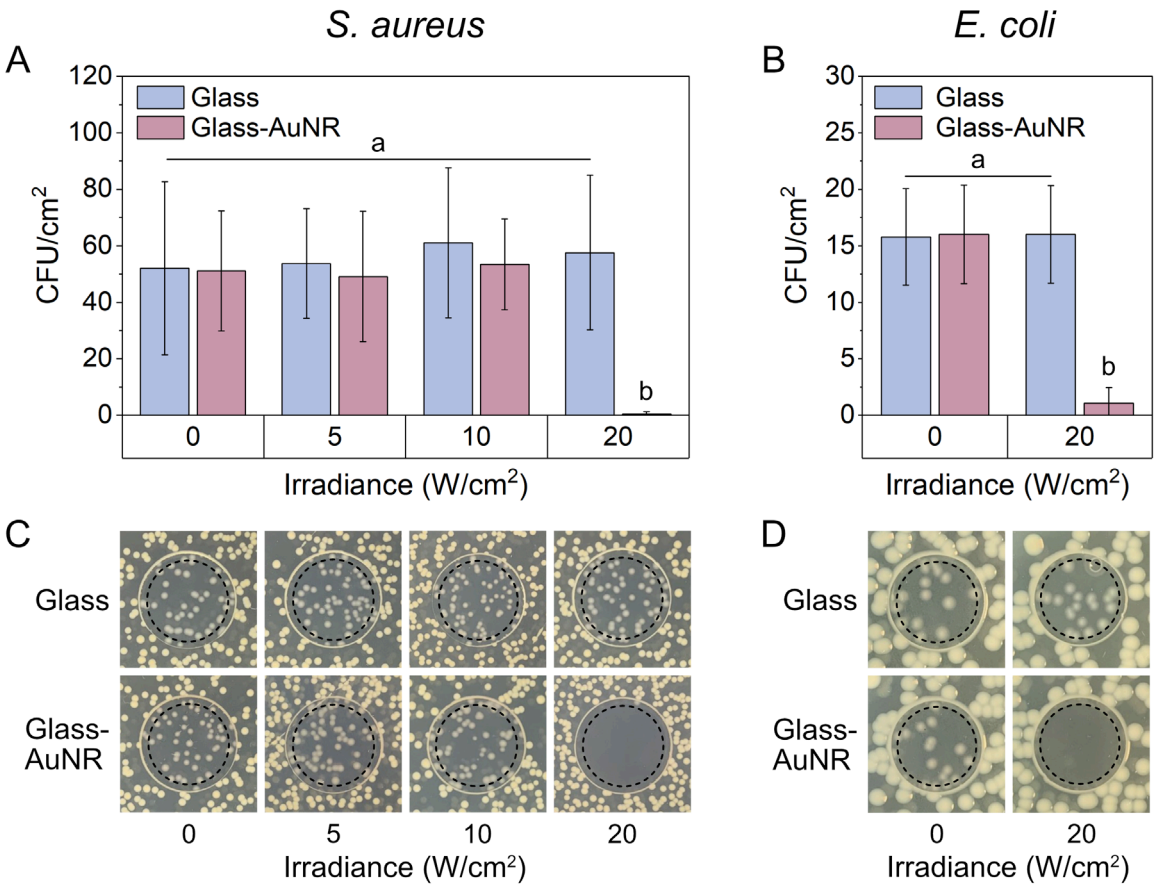


Figure 23. Antibacterial activity of Glass-AuNR irradiates with NIR light for 30 s. (A) and (C) showing the activity against *S. aureus* for intensities 0 (non-irradiated), 5, 10 and 20 W cm^{-2}. (B) and (D) showing the activity against *E. coli* for intensities 0 (non-irradiated) and 20 W cm^{-2}. Data in (A) and (B) is expressed as average CFU cm^{-2} (n = 9), error bars indicate standard deviations. $p < 0.001$. (C) and (D) show example images from the agar plate model for *S. aureus* and *E. coli*, respectively, with bacterial colonies appearing as yellow dots and the black dashed circles encircle the sampling area. Reused with permission from reference (102), licensed under CC-BY 4.0.

For the short irradiation time studied in **Paper I** (30 s), a high laser intensity was required to effectively eradicate bacteria for the supported AuNRs on glass. However, the laser intensity did not influence bacterial viability in the absence of AuNRs (Figure 23) and the bare Glass only increased around 3 °C after irradiation (Figure 15B), highlighting the local photothermal antibacterial activity of the solid-supported AuNRs. The modification strategy thus shows promise for minimising negative influence on surrounding tissue in a biomaterial application. Still, essential *in vitro* studies are needed to assess the effects of the NIR light, solid-supported AuNRs, and their photothermal heating on eukaryotic cells.

As biomaterials commonly are designed to interact favourably with the biological environment in which they will be utilised, it is essential that any potential antibacterial modification strategy does not impede the biomaterials' innate characteristics. For the solid-supported AuNRs studied in this thesis, this becomes relevant in the consideration of the nanorod surface coverage required to achieve an antibacterial effect. For the supported AuNRs on glass, we demonstrated a significant antibacterial activity against both *S. aureus* and *E. coli* with a surface

coverage around 14%, corresponding to approximately 100 nanoparticles per μm^2. This is comparatively low in relation to previous studies with similar systems, where the AuNR loadings vary from a few hundred nanoparticles per μm^2 to multilayer coatings.[62–64,66] The well-defined surface-attachment achieved in this thesis allowed the gold nanorods to retain their optical properties with little influence from plasmon coupling, retaining high photothermal efficiency, and demonstrating significant antibacterial activity under NIR irradiation at adequate intensity.

4.3.1 Antibacterial activity in combination with an antimicrobial peptide

In **Paper IV**, the antibacterial activity of the solid-supported gold nanorods on glass was further explored by studying the effect in combination with the AMP RRP9W4N (Figure 3). In this paper, two different populations of AuNRs were studied, with longitudinal resonance peaks at 840 nm and 870 nm, which are referred to as AuNR840 and AuNR870, respectively. The surface coverage of the AuNR840 samples was 13% and the surface coverage of AuNR870 was 15%. The antibacterial activity was evaluated against *S. aureus*, using the same agar plate model as in **Paper III**, with the addition of 3.125 µM RRP9W4N AMP to the bacterial suspension that was streaked onto the agar plates for half of the samples. The antibacterial activity of AuNR840 and AuNR870 supported on glass, NIR irradiated for 30 s at 4.7 W cm^{-2} and 5.4 W cm^{-2}, respectively, in the absence and presence of AMP, is shown in Figure 24. The two different NIR laser intensities used for the solid-supported AuNR840 and AuNR870 were tuned to obtain similar antibacterial efficacies for both sample types, wherein a higher laser intensity was utilised for the AuNR870, which had lower absorption at the 808 nm excitation wavelength.

The minimum inhibitory concentration (MIC) for the RRP9W4N AMP has previously been established in the range of 6-12 µM.[84,107] In **Paper IV**, a sub-MIC concentration was used, resulting in a significant antibacterial activity without complete inhibition of bacterial growth, corresponding to a 68% reduction in bacterial viability compared to the untreated control. A significant antibacterial activity was demonstrated for both the AuNR840 and AuNR870 samples irradiated with NIR light, resulting in antibacterial efficacies of 89% and 88%, respectively, relative to the untreated control. In line with the findings from **Paper III**, the bacterial viability was not affected by the solid-supported AuNRs in the absence of NIR light, nor by the NIR light in the absence of the AuNRs. Moreover, when comparing the antibacterial activity of the AMP alone to that of the AMP combined with NIR irradiation, no significant differences were observed. Details are available in the Supporting Information to **Paper IV**.

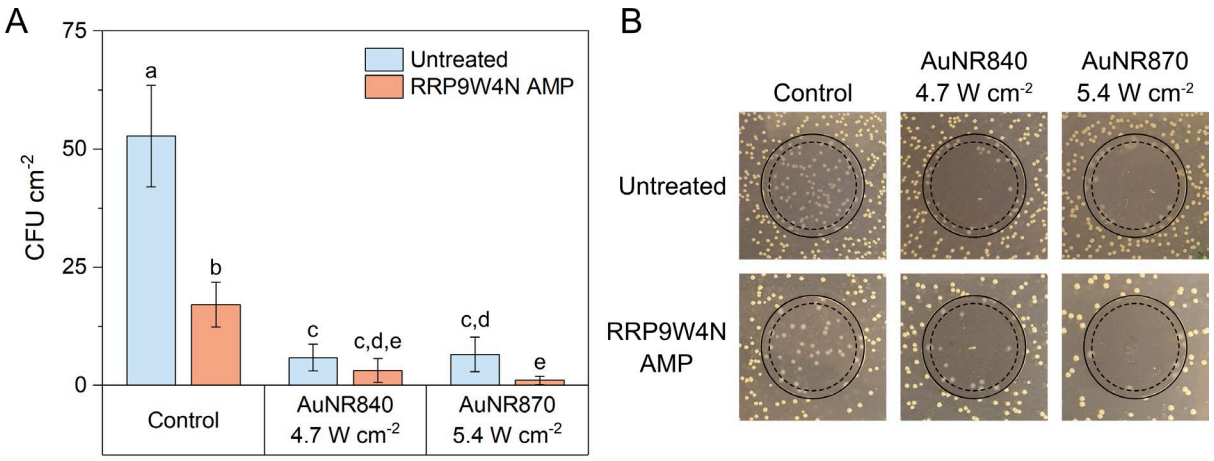


Figure 24. (A) Antibacterial activity against *S. aureus* of AuNR840 and AuNR870 supported on glass, irradiated with NIR light for 30 s at 4.7 W cm^{-2} and 5.4 W cm^{-2}, respectively. The blue bars represent untreated bacterial suspension, and the orange bars results with the addition of 3.125 µM RRP9W4N AMP. Data are presented as average CFU cm^{-2} for nine samples (n = 9) and the error bars denote the standard deviation. $p < 0.05$. (B) Example images of the samples from the agar plate model. The black solid lines indicate the samples, and the dashed lines encircle the sampling area.

Interestingly, when assessing the combined antibacterial activity of the NIR irradiated solid-supported AuNRs and the AMP, diverging results were observed for the AuNR840 and AuNR870 samples. When combining the AuNR840 samples irradiated at 4.7 W cm^{-2} with the RRP9W4N AMP, no significant enhancement of the antibacterial activity compared to the NIR-irradiated AuNR840 alone was demonstrated (Figure 24A). However, combining the AuNR870 samples irradiated at 5.4 W cm^{-2} with the AMP resulted in a significant enhancement of the antibacterial activity compared to the NIR-irradiated AuNR870 alone. The addition of 3.125 µM of RRP9W4N, increased the antibacterial efficacy of the irradiated AuNR870 from 88% to 98%. Based on the findings of **Paper IV**, it appears that combining the antibacterial activity of the RRP9W4N AMP and the photothermal heating from the solid-supported AuNRs can give an enhanced effect, similarly to what has been observed for AMP-functionalised AuNRs in suspension.[78,79,108,109] However, the specific material properties and NIR irradiation parameters, governing the photothermal heating, are crucial for the antibacterial activity of the combined system.

4.3.2 Solid-supported gold nanorod – bacteria interaction

In **Paper IV**, electron microscopy was used to study the interaction between the solid-supported gold nanorods and *S. aureus*. For this study, AuNR870 was supported on titanium, owing to the superior conductivity compared to glass, and the samples had a surface coverage of approximately 10%. In Figure 25A, a SEM micrograph visualising two *S. aureus* cells on the solid-supported AuNRs is shown. TEM micrographs showing cross sections of the interaction between the gold nanorods and *S. aureus*, at different magnifications, are shown in Figure 25B-D. The dark layer on top of the bacterial cells indicates the 100 nm chromium layer sputtered onto the samples to protect them during the TEM specimen preparation. The irregularities visible in the centre of the bacterial cells are likely artefacts induced by the high-voltage electron beam, and no cell-internal structures are visualised since no contrast agents

were used in the TEM specimen preparation. From the TEM investigation, a limited contact area between the *S. aureus* cells and the material surface was demonstrated, estimated at a few hundred nanometres in diameter. Owing to the well-dispersed and relatively low surface coverage of AuNRs, it could be noted that each bacterial cell was in direct contact with only a few nanoparticles, and most of the attachment was to the underlying support. It should be noted that the contact area between the material surface and bacteria might not be fully captured in all cases owing to the thin nature of the TEM specimen, and it may have been damaged by the ion beam during specimen preparation. Despite the limited contact area between the bacteria and the AuNRs, the solid-supported AuNRs demonstrated significant antibacterial activity upon NIR irradiation (Figure 24).

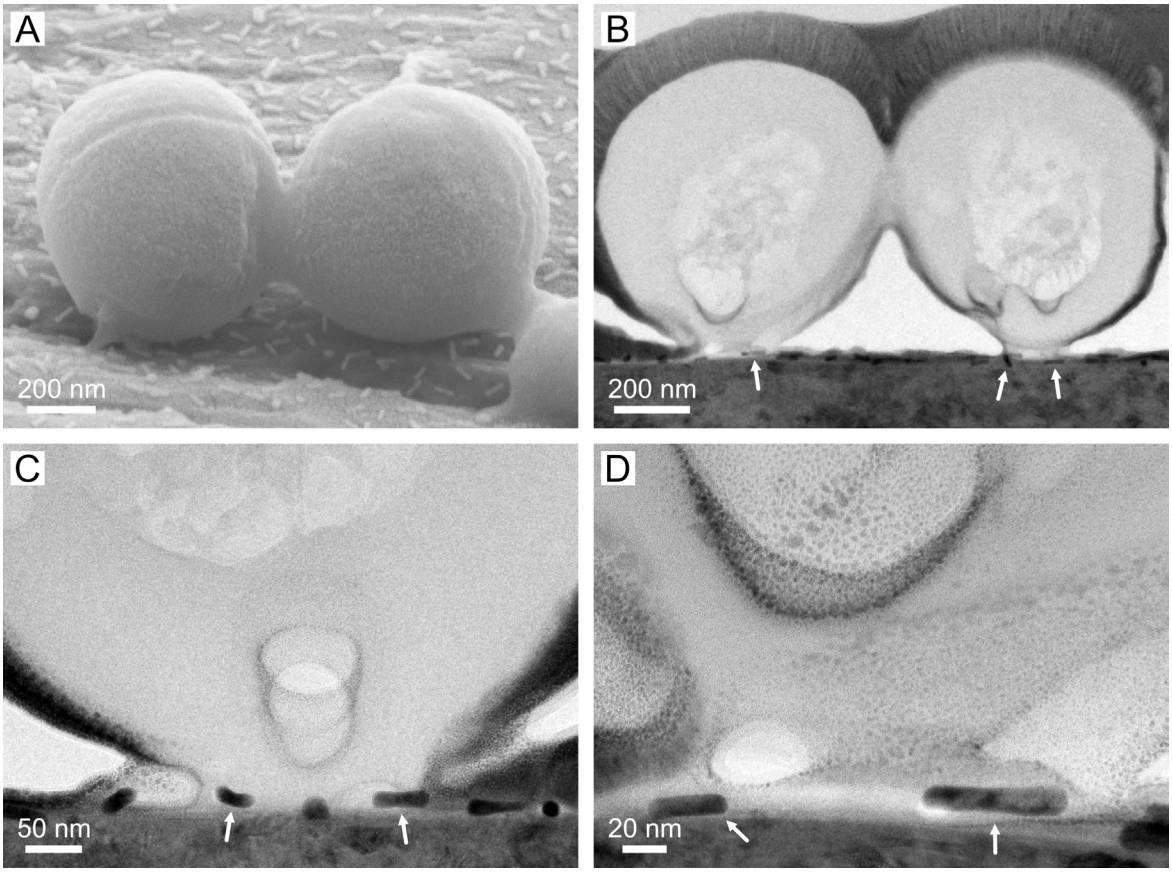


Figure 25. Electron microscopy investigation of the interaction between gold nanorods supported on titanium and *S. aureus*. (A) SEM micrograph of two *S. aureus* cells. (B)-(D) TEM micrographs at different magnifications showing the interaction between the bacterial cells and the gold nanorods, with (D) showing higher magnification of the interface of the leftmost bacterial cell in (B). The dark top layer showing the sputtered 100 nm chromium coating and the lighter circular structures the bacterial cells in cross section. The dark ellipsoids beneath the bacteria show the supported gold nanorods, indicated by white arrows at selected locations.

4.4 Bacterial cytological profiling

In **Paper IV**, bacterial cytological profiling (BCP) was employed to gain insight into the mode of action of the solid-supported gold nanorods in combination with the RRP9W4N AMP. These investigations utilised the AuNR840 supported on glass and NIR irradiation at an intensity of 4.7 W cm^{-2} for 30 s. BCP is a phenotypic analysis method that facilitates evaluation of several cell parameters in a single assay. In **Paper IV**, four fluorescent dyes were used: DAPI to visualise DNA, SytoxGreen to evaluate membrane integrity, FM4-64 to study changes in membrane morphology, and $DiSC_35$ to assess membrane potential.[85,93]

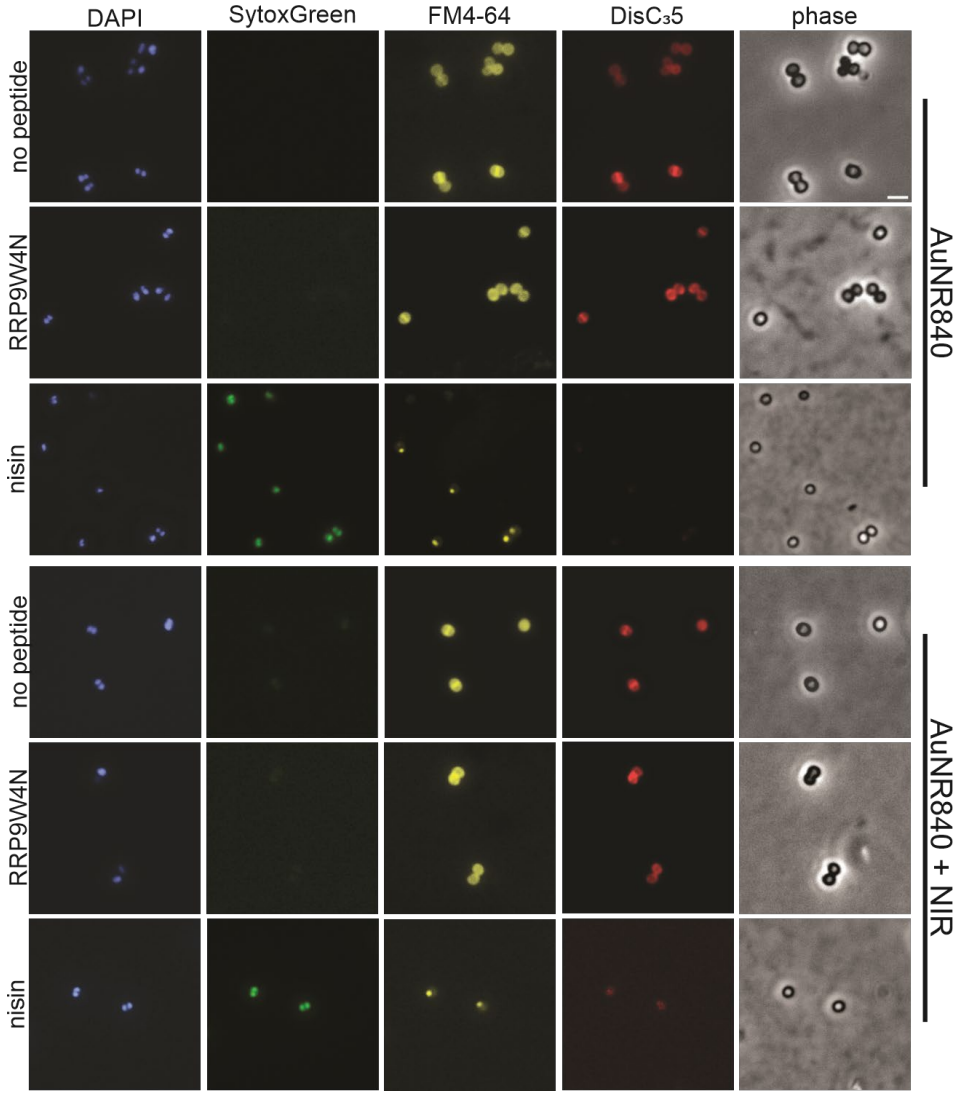


Figure 26. Bacterial cytological profiling of *S. aureus* treated with solid-supported gold nanorods on glass (AuNR840), AuNR840 and RRP9W4N, or AuNR840 and nisin, with and without NIR irradiation at an intensity of 4.7 W cm^{-2} for 30 s. Treated bacterial cells were transferred to agarose patches with DAPI for staining DNA, SytoxGreen which is taken up by large membrane pores, FM4-64 for staining the cell membrane and visualising membrane morphology changes, and $DiSC_35$ to monitor membrane potential. Scale bar is 2 µm.

S. aureus was exposed to AuNR840 alone, in combination with RRP9W4N, or in combination with nisin (positive control), and thereafter irradiated with NIR light or left untreated as controls. Microscopy images from the BCP study are shown in Figure 26 and quantification of the fluorescence intensity of $DiSC_35$ and SytoxGreen in Figure 27. Quantification of DAPI intensity, phase density, and cell area is available in the Supporting Information to **Paper IV**.

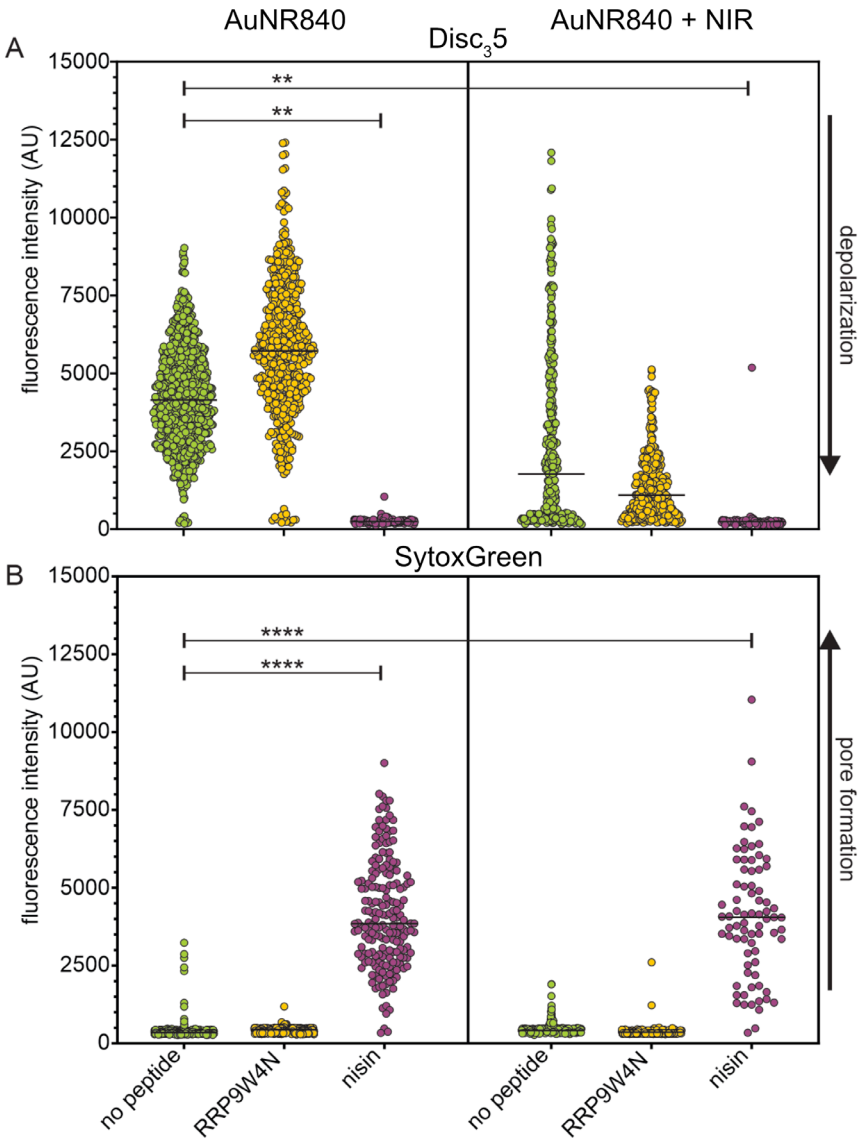


Figure 27. (A) Quantification of $DiSC_35$ fluorescence intensity from microscopy images. $DiSC_35$ accumulates in cell membranes with intact membrane potential and upon depolarisation the dye dissociates from the membrane, resulting in an increase in fluorescence intensity.[110] Pooled data from three biological replicates is shown (two for nisin). Black lines indicate the median. Statistical significance was determined with a one-way nested ANOVA. (B) Quantification of SytoxGreen uptake from microscopy images. SytoxGreen is a DNA-binding dye that does not penetrate intact membranes, but upon formation of membrane pores large enough to let the bulky molecule pass through it diffuses into the cells, leading to a bright DNA stain.[111,112] Pooled data from three biological replicates is shown (two for nisin). Black lines indicate the median. Statistical significance was determined with a one-way nested ANOVA. ** $p < 0.01$, **** $p < 0.0001$.

All samples treated with nisin demonstrated phenotypes indicative of membrane pore formation: in phase contrast the cells appear smaller and less phase dense (Figure 26), FM4-64 foci representative of membrane domain formation are noticeable (Figure 26), greatly reduced DiSC35 fluorescence intensity indicates membrane depolarization (Figure 26, Figure 27A), and clear uptake of SytoxGreen confirms the existence of large membrane pores (Figure 26, Figure 27B). In comparison, the bacterial cells exposed to AuNR840 alone or in combination with RRP9W4N showed no evidence of major membrane disruption, neither with nor without NIR irradiation. In phase contrast the cells appear similar in size and phase density compared to cells exposed to AuNR840 alone without NIR exposure (the negative control), and as such, no indication of cell lysis was present. Consistently, no uptake of SytoxGreen or membrane morphology anomalies in the FM4-64 staining was noticeable.

Contrasting these findings, in previous studies of RRP9W4N membrane disruption has been demonstrated, although at a significantly higher concentration of 30 μM (2.5 to 5-fold the MIC of RRP9W4N).[113] As such, it was hypothesized that lower concentrations of RRP9W4N, like the 3.125 μM utilised here, do not induce membrane pore formation and that the bactericidal effect is attained through a different mechanism. Interestingly, cells treated with RRP9W4N, with and without NIR irradiation, showed a significant reduction in DAPI fluorescence intensity (quantification available in Supporting Information to Paper IV). This phenotype is typically associated with DNA damage and nucleoid fragmentation,[114,115] making it conceivable that the MoA of the RRP9W4N AMP includes a DNA-damaging component, although this remains to be further evaluated in future studies.

For the NIR-irradiated samples, exposed to AuNR840 alone and in combination with RRP9W4N, a heterogeneous membrane depolarising effect was observed, although not statistically significant owing to the high variation between replicates. This trend could suggest that the photothermal heating of the solid-supported gold nanorods, with and without RRP9W4N, impacts the cell membrane to some extent, without inducing large membrane pores. This observation is supported by previous studies wherein membrane disruptive effects caused by the photothermal heating of solid-supported gold nanorods,[64,65] and of nanorods in suspension,[59,60,109] have been shown. However, further investigations are required to validate and specify the impact on the cell membrane.

5. Concluding remarks

This thesis focused on the development and evaluation of materials based on solid-supported gold nanorods and explored how their photothermal characteristics can be utilised for antibacterial applications. Material preparation protocols were developed, achieving gold nanorod surface-attachment primarily through electrostatic interaction between the cationic nanoparticles and an anionic support surface. The developed protocols facilitated reproducible surface-attachment of gold nanorods to glass and titanium in a well-dispersed manner, without utilising additional linking-molecules between the particles and the support.

Through extensive material characterisation using Vis-NIR spectroscopy, electron microscopy, and X-ray diffraction, the characteristics of the supported gold nanorods on glass were evaluated. The single-crystalline gold nanorods retained their plasmon resonance properties once supported on glass, and exhibited a strong orientation on the support wherein most of the particles were attached with the long axis towards the surface. Additionally, a protocol for the preparation of gold nanorod gradient surfaces was developed, producing materials where the gold nanorod surface coverage increased linearly with the distance along the support. By characterising these materials, valuable insight into how the gold nanorods' optical and photothermal properties were influenced by the surface coverage was obtained.

The photothermal properties of the solid-supported gold nanorods were evaluated by monitoring the thermal lattice expansion of the nanoparticles with *in situ* X-ray diffraction. By corroborating XRD data with Vis-NIR spectroscopy and electron microscopy characterisation, a relationship between the NIR laser power, the gold nanorods' temperature and the onset of morphological transformations was established. The importance of experimental evaluation of the photothermal properties of materials like the ones studied in this thesis was highlighted,

where the use of a size distribution of randomly arranged particles with temperature-sensitive morphologies creates a complexity that is non-trivial to predict by theoretical models. Furthermore, by extending the *in situ* XRD methodology to study the gold nanorod gradient surfaces, the nanoparticle temperature as a function of surface coverage was evaluated, showing the significant influence of collective heating effects on these systems.

An experimental protocol was developed for evaluating the antibacterial characteristics of the solid-supported gold nanorods. Utilising this protocol to study the antibacterial activity of the supported gold nanorods on titanium and glass upon NIR excitation revealed the critical role of the support material for the bactericidal effect. On titanium, no effect from the plasmonic heating of the gold nanorods was demonstrated, an observation that was attributed to the dielectric characteristics of the titanium support. However, on glass, a NIR light intensity dependent antibacterial activity from the plasmonic heating of the gold nanorods was attained. Owing to the high antibacterial efficacy demonstrated on glass for a gold nanorod surface coverage of 10-15% and only minor alterations to the surface chemistry of the support, the modification strategy shows promise for exerting a potent antibacterial effect while retaining the biomaterial's innate characteristics.

As a potential multifunctional strategy, the antibacterial activity of the supported gold nanorods on glass in combination with the antimicrobial peptide RRP9W4N was studied. The findings revealed that an enhanced antibacterial efficacy could be obtained when combining the photothermal heating from the solid-supported gold nanorods with the AMP. However, the specific material characteristics and NIR irradiation parameters, which govern the photothermal heating, had a critical influence on the antibacterial activity of the combined system. Bacterial cytological profiling showed that the photothermal heating of the solid-supported gold nanorods, the RRP9W4N AMP, or a combination of both, did not cause major membrane disruption. Rather, indications of DNA-damage were shown for the RRP9W4N AMP, and a non-significant trend towards a heterogeneous membrane depolarising effect was noticeable for the NIR-irradiated solid-supported gold nanorods, both findings motivating further investigations.

Altogether, this thesis provides insight into the characteristics of materials based on solid-supported gold nanorods, with focus on their photothermal behaviour, and emphasises ways of controlling the material properties. Additionally, this work explores how the photothermal properties of the materials can by utilised for antibacterial applications, in the context of addressing the challenge of combatting biomaterial-associated infections.

5.1 Future perspectives

As demonstrated in this thesis, the solid-supported gold nanorods undergo morphology transformations at elevated temperature, including a reduction in aspect ratio of individual particles and coalescence of particle clusters. Thus, it would be of interest to deepen the understanding of the materials by investigating the transformations in more detail, for example by evaluating how the morphological changes evolve at higher temperatures. Furthermore,

assessing the photothermal properties in a more application relevant, aqueous environment would facilitate correlating the *in situ* XRD data with the findings from the *in vitro* antibacterial activity studies. The work in this thesis also showed that the temperature of the gold nanorods is influenced by their surface coverage. As such, studying how the antibacterial activity varies with the surface coverage could provide knowledge of the minimum coverage needed to attain a bactericidal effect for a set laser intensity. Here, the gold nanorod gradient surfaces could serve as a suitable platform for performing such optimisation studies.

The studies in this thesis primarily employed glass as the support for the gold nanorods, owing to its suitable optical properties which facilitated material characterisation. As shown when studying the gold nanorods supported on titanium, the substrate can greatly influence the plasmonic characteristics and thereby the antibacterial activity of the nanoparticles. Extending the modification strategy to more application relevant materials with dielectric properties like glass could be one step towards finding a suitable biomaterial application wherein the photothermal properties of the solid-supported gold nanorods could be harnessed. Here, polymeric biomaterials such as polyetheretherketone or polydimethylsiloxane would be potential options. Additionally, the initial findings from the MoA studies of the solid-supported gold nanorods and the RRP9W4N AMP motivate further investigations on this topic, to elucidate the antibacterial mechanisms in detail. Ultimately, to enable the use of the solid-supported gold nanorods in a biomaterial application, essential cytotoxicity and biocompatibility evaluations are needed, as well as assessment of the *in vivo* antibacterial activity using an animal infection model.

Acknowledgements

This work was funded by the Knut and Alice Wallenberg Foundation through the Wallenberg Academy Fellow program and the Area of Advance in Materials Science at Chalmers University of Technology.

I would like to start by expressing my gratitude to my supervisors. To my main supervisor Martin and my co-supervisor Mats, your unwavering support and seemingly endless supply of ideas have been invaluable during the ups and downs of this project. Thank you for helping me grow over these past few years.

To my examiner Andreas, for your interest in my work and for taking the time to help whenever I needed it.

A big thank you to all the members in MA research group. With a special thanks to Annija, Edvin, Gustav and Elin. I have thoroughly enjoyed undertaking my PhD studies alongside you, and I am immensely grateful for your amazing company and willingness to help.

To all my co-authors, Michal, Alva, John, Ann-Britt, Michaela, and Tetiana. Thank you for all your contributions, it has been a pleasure working with you.

To everyone at the Applied Chemistry division. Thank you for creating a welcoming atmosphere and for being wonderful colleagues. To Frida, Smaragda and Sevil, thank you for being such kind and encouraging office mates. To Jakob, Leo and Giovanni. This journey would have been a whole lot less fun without you; your company has been the best mood booster I could have asked for.

To my family and friends. Thank you for always celebrating even the small achievements, and for giving me the energy needed to get through the more challenging periods.

Finally, to my husband David. Thank you for being my person, for your love and for always supporting me.

Maja Lidström Uusitalo
Gothenburg, November 2025

References

(1) Ghasemi-Mobarakeh, L.; Kolahreez, D.; Ramakrishna, S.; Williams, D. Key Terminology in Biomaterials and Biocompatibility. *Curr Opin Biomed Eng* **2019**, *10*, 45–50. https://doi.org/10.1016/j.cobme.2019.02.004.

(2) United Nations; Department of Economics and Social Affairs; Population Division (2024). *World Population Prospects 2024: Summary of Results*; 2024.

(3) World Health Organization. *World Health Statistics 2025: Monitoring Health for the SDGs, Sustainable Development Goals*; Geneva, 2025.

(4) Pabinger, C.; Lothaller, H.; Portner, N.; Geissler, A. Projections of Hip Arthroplasty in OECD Countries up to 2050. *HIP International* **2018**, *28* (5), 498–506. https://doi.org/10.1177/1120700018757940.

(5) Matharu, G. S.; Culliford, D. J.; Blom, A. W.; Judge, A. Projections for Primary Hip and Knee Replacement Surgery up to the Year 2060: An Analysis Based on Data from The National Joint Registry for England, Wales, Northern Ireland and the Isle of Man. *Ann R Coll Surg Engl* **2022**, *104* (6), 443–448. https://doi.org/10.1308/rcsann.2021.0206.

(6) Elani, H. W.; Starr, J. R.; Da Silva, J. D.; Gallucci, G. O. Trends in Dental Implant Use in the U.S., 1999–2016, and Projections to 2026. *J Dent Res* **2018**, *97* (13), 1424–1430. https://doi.org/10.1177/0022034518792567.

(7) Høiby, N.; Bjarnsholt, T.; Givskov, M.; Molin, S.; Ciofu, O. Antibiotic Resistance of Bacterial Biofilms. *Int J Antimicrob Agents* **2010**, *35* (4), 322–332. https://doi.org/10.1016/j.ijantimicag.2009.12.011.

(8) World Health Organization. *2023 Antibacterial Agents in Clinical and Preclinical Development: An Overview and Analysis*; Geneva, 2024.

(9) World Health Organization. *Global Antibiotic Resistance Surveillance Report 2025: WHO Global Antimicrobial Resistance and Use Surveillance System (GLASS)*; Geneva, 2025.

(10) Murray, C. J.; Ikuta, K. S.; Sharara, F.; ... ; Naghavi, M. Global Burden of Bacterial Antimicrobial Resistance in 2019: A Systematic Analysis. *The Lancet* **2022**, *399* (10325), 629–655. https://doi.org/10.1016/S0140-6736(21)02724-0.

(11) Campoccia, D.; Montanaro, L.; Arciola, C. R. A Review of the Biomaterials Technologies for Infection-Resistant Surfaces. *Biomaterials* **2013**, *34* (34), 8533–8554. https://doi.org/10.1016/j.biomaterials.2013.07.089.

(12) Butler, J.; Handy, R. D.; Upton, M.; Besinis, A. Review of Antimicrobial Nanocoatings in Medicine and Dentistry: Mechanisms of Action, Biocompatibility Performance, Safety, and Benefits Compared to Antibiotics. *ACS Nano* **2023**, *17* (8), 7064–7092. https://doi.org/10.1021/acsnano.2c12488.

(13) Faraday, M. The Bakerian Lecture: Experimental Relations of Gold (and Other Metals) to Light. *Philos Trans R Soc Lond* **1857**, *147*, 145–181.

(14) Amendola, V.; Pilot, R.; Frasconi, M.; Maragò, O. M.; Iatì, M. A. Surface Plasmon Resonance in Gold Nanoparticles: A Review. *Journal of Physics Condensed Matter*. Institute of Physics Publishing April 20, 2017. https://doi.org/10.1088/1361-648X/aa60f3.

(15) Jain, P. K.; Huang, X.; El-Sayed, I. H.; El-Sayed, M. A. Noble Metals on the Nanoscale: Optical and Photothermal Properties and Some Applications in Imaging, Sensing, Biology, and Medicine. *Acc Chem Res* **2008**, *41* (12), 1578–1586. https://doi.org/10.1021/ar7002804.

(16) Huang, X.; Neretina, S.; El-Sayed, M. A. Gold Nanorods: From Synthesis and Properties to Biological and Biomedical Applications. *Advanced Materials* **2009**, *21* (48), 4880–4910. https://doi.org/10.1002/adma.200802789.

(17) Weissleder, R. A Clearer Vision for in Vivo Imaging. *Nat Biotechnol* **2001**, *19*, 316–317.

(18) Feng, Z.; Tang, T.; Wu, T.; Yu, X.; Zhang, Y.; Wang, M.; Zheng, J.; Ying, Y.; Chen, S.; Zhou, J.; Fan, X.; Zhang, D.; Li, S.; Zhang, M.; Qian, J. Perfecting and Extending the Near-Infrared Imaging Window. *Light Sci Appl* **2021**, *10*, 197. https://doi.org/10.1038/s41377-021-00628-0.

(19) Turkevic, J.; Cooper Stevenson, P.; Hillier, J. A Study of the Nucleation and Growth Processes in the Synthesis of Colloidal Gold. *Discuss Faraday Soc* **1941**, *11*, 55–75.

(20) Kimling, J.; Maier, M.; Okenve, B.; Kotaidis, V.; Ballot, H.; Plech, A. Turkevich Method for Gold Nanoparticle Synthesis Revisited. *Journal of Physical Chemistry B* **2006**, *110* (32), 15700–15707. https://doi.org/10.1021/jp061667w.

(21) Jana, N. R.; Gearheart, L.; Murphy, C. J. Seed-Mediated Growth Approach for Shape-Controlled Synthesis of Spheroidal and Rod-like Gold Nanoparticles Using a Surfactant Template. *Advanced Materials* **2001**, *13* (18), 1389–1393. https://doi.org/10.1002/1521-4095(200109)13:18<1389::AID-ADMA1389>3.0.CO;2-F.

(22) Nikoobakht, B.; El-Sayed, M. A. Preparation and Growth Mechanism of Gold Nanorods (NRs) Using Seed-Mediated Growth Method. *Chemistry of Materials* **2003**, *15* (10), 1957–1962. https://doi.org/10.1021/cm0207321.

(23) Scarabelli, L.; Sánchez-Iglesias, A.; Pérez-Juste, J.; Liz-Marzán, L. M. A "Tips and Tricks" Practical Guide to the Synthesis of Gold Nanorods. *Journal of Physical Chemistry Letters* **2015**, *6* (21), 4270–4279. https://doi.org/10.1021/acs.jpclett.5b02123.

(24) Saha, K.; Agasti, S. S.; Kim, C.; Li, X.; Rotello, V. M. Gold Nanoparticles in Chemical and Biological Sensing. *Chem Rev* **2012**, *112* (5), 2739–2779. https://doi.org/10.1021/cr2001178.

(25) Ndolomingo, M. J.; Bingwa, N.; Meijboom, R. Review of Supported Metal Nanoparticles: Synthesis Methodologies, Advantages and Application as Catalysts. *J Mater Sci* **2020**, *55*, 6195–6241. https://doi.org/10.1007/s10853-020-04415-x.

(26) Arnold, M.; Schwieder, M.; Blümmel, J.; Cavalcanti-Adam, E. A.; López-Garcia, M.; Kessler, H.; Geiger, B.; Spatz, J. P. Cell Interactions with Hierarchically Structured Nano-Patterned Adhesive Surfaces. *Soft Matter* **2009**, *5* (1), 72–77. https://doi.org/10.1039/b815634d.

(27) Zhao, Y. Q.; Sun, Y.; Zhang, Y.; Ding, X.; Zhao, N.; Yu, B.; Zhao, H.; Duan, S.; Xu, F. J. Well-Defined Gold Nanorod/Polymer Hybrid Coating with Inherent Antifouling and Photothermal Bactericidal Properties for Treating an Infected Hernia. *ACS Nano* **2020**, *14* (2), 2265–2275. https://doi.org/10.1021/acsnano.9b09282.

(28) Ben Haddada, M.; Blanchard, J.; Casale, S.; Krafft, J.-M.; Vallée, A.; Méthivier, C.; Boujday, S. Optimizing the Immobilization of Gold Nanoparticles on Functionalized

Silicon Surfaces: Amine- vs Thiol-Terminated Silane. *Gold Bull* **2013**, *46* (4), 335–341. https://doi.org/10.1007/s13404-013-0120-y.

(29) Kyaw, H. H.; Al-Harthi, S. H.; Sellai, A.; Dutta, J. Self-Organization of Gold Nanoparticles on Silanated Surfaces. *Beilstein Journal of Nanotechnology* **2015**, *6*, 2345–2353. https://doi.org/10.3762/bjnano.6.242.

(30) Ferhan, A. R.; Guo, L.; Kim, D. H. Influence of Ionic Strength and Surfactant Concentration on Electrostatic Surfacial Assembly of Cetyltrimethylammonium Bromide-Capped Gold Nanorods on Fully Immersed Glass. *Langmuir* **2010**, *26* (14), 12433–12442. https://doi.org/10.1021/la101105t.

(31) Fennell Evans, D.; Wennerström, H. *The Colloidal Domain: Where Physics, Chemistry, Biology, and Technology Meet*, 2nd ed.; Wiley-VCH: New York, 1999.

(32) Funston, A. M.; Novo, C.; Davis, T. J.; Mulvaney, P. Plasmon Coupling of Gold Nanorods at Short Distances and in Different Geometries. *Nano Lett* **2009**, *9* (4), 1651–1658. https://doi.org/10.1021/nl900034v.

(33) Baffou, G.; Berto, P.; Bermúdez Ureña, E.; Quidant, R.; Monneret, S.; Polleux, J.; Rigneault, H. Photoinduced Heating of Nanoparticle Arrays. *ACS Nano* **2013**, *7* (8), 6478–6488. https://doi.org/10.1021/nn401924n.

(34) Lundgren, A.; Munktell, S.; Lacey, M.; Berglin, M.; Björefors, F. Formation of Gold Nanoparticle Size and Density Gradients via Bipolar Electrochemistry. *ChemElectroChem* **2016**, *3* (3), 378–382. https://doi.org/10.1002/celc.201500413.

(35) Bhat, R. R.; Fischer, D. A.; Genzer, J. Fabricating Planar Nanoparticle Assemblies with Number Density Gradients. *Langmuir* **2002**, *18* (15), 5640–5643. https://doi.org/10.1021/la025524m.

(36) Goreham, R. V.; Short, R. D.; Vasilev, K. Method for the Generation of Surface-Bound Nanoparticle Density Gradients. *Journal of Physical Chemistry C* **2011**, *115* (8), 3429–3433. https://doi.org/10.1021/jp111221g.

(37) Lundgren, A.; Hulander, M.; Brorsson, J.; Hermansson, M.; Elwing, H.; Andersson, O.; Liedberg, B.; Berglin, M. Gold-Nanoparticle-Assisted Self-Assembly of Chemical Gradients with Tunable Sub-50 Nm Molecular Domains. *Particle and Particle Systems Characterization* **2014**, *31* (2), 209–218. https://doi.org/10.1002/ppsc.201300154.

(38) Huwiler, C.; Kunzler, T. P.; Textor, M.; Vörös, J.; Spencer, N. D. Functionalizable Nanomorphology Gradients via Colloidal Self-Assembly. *Langmuir* **2007**, *23* (11), 5929–5935. https://doi.org/10.1021/la0700422.

(39) Baffou, G.; Cichos, F.; Quidant, R. Applications and Challenges of Thermoplasmonics. *Nat Mater* **2020**, *19* (9), 946–958. https://doi.org/10.1038/s41563-020-0740-6.

(40) Huang, X.; Jain, P. K.; El-Sayed, I. H.; El-Sayed, M. A. Plasmonic Photothermal Therapy (PPTT) Using Gold Nanoparticles. *Lasers Med Sci* **2008**, *23* (3), 217–228. https://doi.org/10.1007/s10103-007-0470-x.

(41) Jauffred, L.; Samadi, A.; Klingberg, H.; Bendix, P. M.; Oddershede, L. B. Plasmonic Heating of Nanostructures. *Chem Rev* **2019**, *119* (13), 8087–8130. https://doi.org/10.1021/acs.chemrev.8b00738.

(42) Baffou, G.; Bon, P.; Savatier, J.; Polleux, J.; Zhu, M.; Merlin, M.; Rigneault, H.; Monneret, S. Thermal Imaging of Nanostructures by Quantitative Optical Phase Analysis. *ACS Nano* **2012**, *6* (3), 2452–2458. https://doi.org/10.1021/nn2047586.

(43) Andrén, D.; Shao, L.; Odebo Länk, N.; Aćimović, S. S.; Johansson, P.; Käll, M. Probing Photothermal Effects on Optically Trapped Gold Nanorods by Simultaneous Plasmon Spectroscopy and Brownian Dynamics Analysis. *ACS Nano* **2017**, *11* (10), 10053–10061. https://doi.org/10.1021/acsnano.7b04302.

(44) Baffou, G.; Kreuzer, M. P.; Kulzer, F.; Quidant, R. Temperature Mapping near Plasmonic Nanostructures Using Fluorescence Polarization Anisotropy. *Opt Express* **2009**, *7* (5), 3291–3298. https://doi.org/https://doi.org/10.1364/OE.17.003291.

(45) Freddi, S.; Sironi, L.; D'Antuono, R.; Morone, D.; Donà, A.; Cabrini, E.; D'Alfonso, L.; Collini, M.; Pallavicini, P.; Baldi, G.; Maggioni, D.; Chirico, G. A Molecular Thermometer for Nanoparticles for Optical Hyperthermia. *Nano Lett* **2013**, *13* (5), 2004–2010. https://doi.org/10.1021/nl400129v.

(46) Rohani, S.; Quintanilla, M.; Tuccio, S.; De Angelis, F.; Cantelar, E.; Govorov, A. O.; Razzari, L.; Vetrone, F. Enhanced Luminescence, Collective Heating, and Nanothermometry in an Ensemble System Composed of Lanthanide-Doped Upconverting Nanoparticles and Gold Nanorods. *Adv Opt Mater* **2015**, *3* (11), 1606–1613. https://doi.org/10.1002/adom.201500380.

(47) Ma, H.; Bendix, P. M.; Oddershede, L. B. Large-Scale Orientation Dependent Heating from a Single Irradiated Gold Nanorod. *Nano Lett* **2012**, *12* (8), 3954–3960. https://doi.org/10.1021/nl3010918.

(48) Bendix, P. M.; Reihani, S. N. S.; Oddershede, L. B. Direct Measurements of Heating by Electromagnetically Trapped Gold Nanoparticles on Supported Lipid Bilayers. *ACS Nano* **2010**, *4* (4), 2256–2262. https://doi.org/10.1021/nn901751w.

(49) Plech, A.; Kotaidis, V.; Grésillon, S.; Dahmen, C.; Von Plessen, G. Laser-Induced Heating and Melting of Gold Nanoparticles Studied by Time-Resolved x-Ray Scattering. *Phys Rev B Condens Matter Mater Phys* **2004**, *70* (19), 195423. https://doi.org/10.1103/PhysRevB.70.195423.

(50) Wong, D. F.; Young, K.; Ng, Y. S.; Plech, A.; Kürbitz, S.; Berg, K.-J.; Graener, H.; Berg, G.; Grésillon, S.; Kaempfe, M.; Feldmann, J.; Wulff, M.; Von Plessen, G. Time-Resolved X-Ray Diffraction on Laser-Excited Metal Nanoparticles. *Europhys. Lett* **2003**, *61* (6), 762–768.

(51) Vines, J. B.; Yoon, J. H.; Ryu, N. E.; Lim, D. J.; Park, H. Gold Nanoparticles for Photothermal Cancer Therapy. *Front Chem* **2019**, *7*, 167. https://doi.org/10.3389/fchem.2019.00167.

(52) Connor, E. E.; Mwamuka, J.; Gole, A.; Murphy, C. J.; Wyatt, M. D. Gold Nanoparticles Are Taken up by Human Cells but Do Not Cause Acute Cytotoxicity. *Small* **2005**, *1* (3), 325–327. https://doi.org/10.1002/smll.200400093.

(53) Asharani, P. V.; Lianwu, Y.; Gong, Z.; Valiyaveettil, S. Comparison of the Toxicity of Silver, Gold and Platinum Nanoparticles in Developing Zebrafish Embryos. *Nanotoxicology* **2011**, *5* (1), 43–54. https://doi.org/10.3109/17435390.2010.489207.

(54) Bar-Ilan, O.; Albrecht, R. M.; Fako, V. E.; Furgeson, D. Y. Toxicity Assessments of Multisized Gold and Silver Nanoparticles in Zebrafish Embryos. *Small* **2009**, *5* (16), 1897–1910. https://doi.org/10.1002/smll.200801716.

(55) Alkilany, A. M.; Nagaria, P. K.; Hexel, C. R.; Shaw, T. J.; Murphy, C. J.; Wyatt, M. D. Cellular Uptake and Cytotoxicity of Gold Nanorods: Molecular Origin of Cytotoxicity

and Surface Effects. *Small* **2009**, *5* (6), 701–708. https://doi.org/10.1002/smll.200801546.

(56) Alkilany, A. M.; Murphy, C. J. Toxicity and Cellular Uptake of Gold Nanoparticles: What We Have Learned so Far? *Journal of Nanoparticle Research* **2010**, *12* (7), 2313–2333. https://doi.org/10.1007/s11051-010-9911-8.

(57) Dickerson, E. B.; Dreaden, E. C.; Huang, X.; El-Sayed, I. H.; Chu, H.; Pushpanketh, S.; McDonald, J. F.; El-Sayed, M. A. Gold Nanorod Assisted Near-Infrared Plasmonic Photothermal Therapy (PPTT) of Squamous Cell Carcinoma in Mice. *Cancer Lett* **2008**, *269* (1), 57–66. https://doi.org/10.1016/j.canlet.2008.04.026.

(58) Huang, X.; El-Sayed, I. H.; Qian, W.; El-Sayed, M. A. Cancer Cell Imaging and Photothermal Therapy in the Near-Infrared Region by Using Gold Nanorods. *J Am Chem Soc* **2006**, *128* (6), 2115–2120. https://doi.org/10.1021/ja057254a.

(59) Sean Norman, R.; Stone, J. W.; Gole, A.; Murphy, C. J.; Sabo-Attwood, T. L. Targeted Photothermal Lysis of the Pathogenic Bacteria, Pseudomonas Aeruginosa, with Gold Nanorods. *Nano Lett* **2008**, *8* (1), 302–306. https://doi.org/10.1021/nl0727056.

(60) Zhao, Y.; Guo, Q.; Dai, X.; Wei, X.; Yu, Y.; Chen, X.; Li, C.; Cao, Z.; Zhang, X. A Biomimetic Non-Antibiotic Approach to Eradicate Drug-Resistant Infections. *Advanced Materials* **2019**, *31* (7), 1806024. https://doi.org/10.1002/adma.201806024.

(61) Busscher, H. J.; Van Der Mei, H. C.; Subbiahdoss, G.; Jutte, P. C.; Van Den Dungen, J. J. A. M.; Zaat, S. A. J.; Schultz, M. J.; Grainger, D. W. Biomaterial-Associated Infection: Locating the Finish Line in the Race for the Surface. *Sci Transl Med* **2012**, *4* (153), 153rv10. https://doi.org/10.1126/scitranslmed.3004528.

(62) Zhu, Y.; Ramasamy, M.; Yi, D. K. Antibacterial Activity of Ordered Gold Nanorod Arrays. *ACS Appl Mater Interfaces* **2014**, *6* (17), 15078–15085. https://doi.org/10.1021/am503153v.

(63) Pihl, M.; Bruzell, E.; Andersson, M. Bacterial Biofilm Elimination Using Gold Nanorod Localised Surface Plasmon Resonance Generated Heat. *Materials Science and Engineering C* **2017**, *80*, 54–58. https://doi.org/10.1016/j.msec.2017.05.067.

(64) Yang, T.; Wang, D.; Liu, X. Assembled Gold Nanorods for the Photothermal Killing of Bacteria. *Colloids Surf B Biointerfaces* **2019**, *173*, 833–841. https://doi.org/10.1016/j.colsurfb.2018.10.060.

(65) Zhao, Y.-Q.; Xiu, Z.; Wu, R.; Zhang, L.; Ding, X.; Zhao, N.; Duan, S.; Xu, F.-J. A Near-Infrared-Responsive Quaternary Ammonium/Gold Nanorod Hybrid Coating with Enhanced Antibacterial Properties. *Adv Nanobiomed Res* **2022**, *2* (11). https://doi.org/10.1002/anbr.202200111.

(66) De Miguel, I.; Prieto, I.; Albornoz, A.; Sanz, V.; Weis, C.; Turon, P.; Quidant, R. Plasmon-Based Biofilm Inhibition on Surgical Implants. *Nano Lett* **2019**, *19* (4), 2524–2529. https://doi.org/10.1021/acs.nanolett.9b00187.

(67) Haghighat Bayan, M. A.; Rinoldi, C.; Rybak, D.; Zargarian, S. S.; Zakrzewska, A.; Cegielska, O.; Põhako-Palu, K.; Zhang, S.; Stobnicka-Kupiec, A.; Górny, R. L.; Nakielski, P.; Kogermann, K.; De Sio, L.; Ding, B.; Pierini, F. Engineering Surgical Face Masks with Photothermal and Photodynamic Plasmonic Nanostructures for Enhancing Filtration and On-Demand Pathogen Eradication. *Biomater Sci* **2024**, *12* (4), 949–963. https://doi.org/10.1039/d3bm01125a.

(68) Glinel, K.; Jonas, A. M.; Jouenne, T.; Leprince, J.; Galas, L.; Huck, W. T. S. Antibacterial and Antifouling Polymer Brushes Incorporating Antimicrobial Peptide. *Bioconjug Chem* **2009**, *20* (1), 71–77. https://doi.org/10.1021/bc800280u.

(69) Gao, G.; Lange, D.; Hilpert, K.; Kindrachuk, J.; Zou, Y.; Cheng, J. T. J.; Kazemzadeh-Narbat, M.; Yu, K.; Wang, R.; Straus, S. K.; Brooks, D. E.; Chew, B. H.; Hancock, R. E. W.; Kizhakkedathu, J. N. The Biocompatibility and Biofilm Resistance of Implant Coatings Based on Hydrophilic Polymer Brushes Conjugated with Antimicrobial Peptides. *Biomaterials* **2011**, *32* (16), 3899–3909. https://doi.org/10.1016/j.biomaterials.2011.02.013.

(70) Zimmerli, W. Clinical Presentation and Treatment of Orthopaedic Implant-Associated Infection. *J Intern Med* **2014**, *276* (2), 111–119. https://doi.org/10.1111/joim.12233.

(71) Zimmerli, W.; Trampuz, A.; Ochsner, P. E. Prosthetic-Joint Infections. *N Engl J Med* **2004**, *351* (16), 1645–1654.

(72) Ziesmer, J.; Venckute Larsson, J.; Sotiriou, G. A. Hybrid Microneedle Arrays for Antibiotic and Near-IR Photothermal Synergistic Antimicrobial Effect against Methicillin-Resistant Staphylococcus Aureus. *Chemical Engineering Journal* **2023**, *462*. https://doi.org/10.1016/j.cej.2023.142127.

(73) Moorcroft, S. C. T.; Roach, L.; Jayne, D. G.; Ong, Z. Y.; Ong, Z. Y.; Evans, S. D. Nanoparticle-Loaded Hydrogel for the Light-Activated Release and Photothermal Enhancement of Antimicrobial Peptides. *ACS Appl Mater Interfaces* **2020**, *12* (22), 24544–24554. https://doi.org/10.1021/acsami.9b22587.

(74) He, D.; Yang, T.; Qian, W.; Qi, C.; Mao, L.; Yu, X.; Zhu, H.; Luo, G.; Deng, J. Combined Photothermal and Antibiotic Therapy for Bacterial Infection via Acidity-Sensitive Nanocarriers with Enhanced Antimicrobial Performance. *Appl Mater Today* **2018**, *12*, 415–429. https://doi.org/10.1016/j.apmt.2018.07.006.

(75) Yeung, A. T. Y.; Gellatly, S. L.; Hancock, R. E. W. Multifunctional Cationic Host Defence Peptides and Their Clinical Applications. *Cellular and Molecular Life Sciences* **2011**, *68* (13), 2161–2176. https://doi.org/10.1007/s00018-011-0710-x.

(76) Shai, Y. Mode of Action of Membrane Active Antimicrobial Peptides. *Biopolymers (Peptide Science)* **2002**, *66*, 236–248. https://doi.org/10.1002/bip.10260.

(77) Chen, Q.; Zhang, L.; Feng, Y.; Shi, F.; Wang, Y.; Wang, P.; Liu, L. Dual-Functional Peptide Conjugated Gold Nanorods for the Detection and Photothermal Ablation of Pathogenic Bacteria. *J Mater Chem B* **2018**, *6* (46), 7643–7651. https://doi.org/10.1039/c8tb01835a.

(78) Chen, J.; Dai, T.; Yu, J.; Dai, X.; Chen, R.; Wu, J.; Li, N.; Fan, L.; Mao, Z.; Sheng, G.; Li, L. Integration of Antimicrobial Peptides and Gold Nanorods for Bimodal Antibacterial Applications. *Biomater Sci* **2020**, *8* (16), 4447–4457. https://doi.org/10.1039/d0bm00782j.

(79) Xu, X.; Ding, Y.; Hadianamrei, R.; Lv, S.; You, R.; Pan, F.; Zhang, P.; Wang, N.; Zhao, X. Antimicrobial Peptide Functionalized Gold Nanorods Combining Near-Infrared Photothermal Therapy for Effective Wound Healing. *Colloids Surf B Biointerfaces* **2022**, *220*. https://doi.org/10.1016/j.colsurfb.2022.112887.

(80) Atefyekta, S.; Blomstrand, E.; Rajasekharan, A. K.; Svensson, S.; Trobos, M.; Hong, J.; Webster, T. J.; Thomsen, P.; Andersson, M. Antimicrobial Peptide-Functionalized

Mesoporous Hydrogels. *ACS Biomater Sci Eng* **2021**, *7* (4), 1693–1702. https://doi.org/10.1021/acsbiomaterials.1c00029.

(81) Blomstrand, E.; Atefyekta, S.; Rajasekharan, A. K.; Andersson, M. Clinical Investigation of Use of an Antimicrobial Peptide Hydrogel Wound Dressing on Intact Skin. *J Wound Care* **2023**, *32* (6), 368–375. https://doi.org/10.12968/jowc.2023.32.6.368.

(82) Blomstrand, E.; Rajasekharan, A. K.; Atefyekta, S.; Andersson, M. Cross-Linked Lyotropic Liquid Crystal Particles Functionalized with Antimicrobial Peptides. *Int J Pharm* **2022**, *627*. https://doi.org/10.1016/j.ijpharm.2022.122215.

(83) Stepulane, A.; Rajasekharan, A. K.; Andersson, M. Multifunctional Surface Modification of PDMS for Antibacterial Contact Killing and Drug-Delivery of Polar, Nonpolar, and Amphiphilic Drugs. *ACS Appl Bio Mater* **2022**, *5* (11), 5289–5301. https://doi.org/10.1021/acsabm.2c00705.

(84) Stepulane, A.; Rajasekharan, A. K.; Andersson, M. Antibacterial Efficacy of Antimicrobial Peptide-Functionalized Hydrogel Particles Combined with Vancomycin and Oxacillin Antibiotics. *Int J Pharm* **2024**, *664*. https://doi.org/10.1016/j.ijpharm.2024.124630.

(85) Nonejuie, P.; Burkart, M.; Pogliano, K.; Pogliano, J. Bacterial Cytological Profiling Rapidly Identifies the Cellular Pathways Targeted by Antibacterial Molecules. *Proceedings of the National Academy of Sciences* **2013**, *110* (40), 16169–16174. https://doi.org/10.1073/pnas.1311066110.

(86) Schäfer, A.-B.; Wenzel, M. A How-To Guide for Mode of Action Analysis of Antimicrobial Peptides. *Front Cell Infect Microbiol* **2020**, *10*. https://doi.org/10.3389/fcimb.2020.540898.

(87) Xu, R. *Particle Characterization: Light Scattering Methods*, 1st ed.; Springer Netherlands: Dordrecht, 2002.

(88) Williams, D. B.; Carter, C. B. *Transmission Electron Microscopy: A Textbook for Materials Science*, 2nd ed.; Springer US: New York, 2009.

(89) Schindelin, J.; Arganda-Carreras, I.; Frise, E.; Kaynig, V.; Longair, M.; Pietzsch, T.; Preibisch, S.; Rueden, C.; Saalfeld, S.; Schmid, B.; Tinevez, J.-Y.; White, D. J.; Hartenstein, V.; Eliceiri, K.; Tomancak, P.; Cardona, A. Fiji: An Open-Source Platform for Biological-Image Analysis. *Nat Methods* **2012**, *9* (7), 676–682. https://doi.org/10.1038/nmeth.2019.

(90) Langford, R. M.; Clinton, C. In Situ Lift-out Using a FIB-SEM System. *Micron* **2004**, *35* (7), 607–611. https://doi.org/10.1016/j.micron.2004.03.002.

(91) Goldstein, J. I.; Newbury, D. E.; Michael, J. R.; Ritchie, N. W. M.; Scott, J. H. J.; Joy, D. C. *Scanning Electron Microscopy and X-Ray Microanalysis*, 4th ed.; Springer New York: New York, 2018.

(92) Stevie, F. A.; Donley, C. L. Introduction to X-Ray Photoelectron Spectroscopy. *Journal of Vacuum Science & Technology A: Vacuum, Surfaces, and Films* **2020**, *38*, 063204. https://doi.org/10.1116/6.0000412.

(93) Schäfer, A.-B.; Sidarta, M.; Abdelmesseh Nekhala, I.; Marinho Righetto, G.; Arshad, A.; Wenzel, M. Dissecting Antibiotic Effects on the Cell Envelope Using Bacterial

Cytological Profiling: A Phenotypic Analysis Starter Kit. *Microbiol Spectr* **2024**, *12* (3). https://doi.org/10.1128/spectrum.03275-23.

(94) Smart, L. E.; Moore, E. A. *Solid State Chemistry: An Introduction*, 3rd ed.; CRC Press: Boca Raton, 2005.

(95) Uusitalo, M.; Strach, M.; Eriksson, G.; Dmytrenko, T.; Andersson, J.; Dahlin, A.; Hulander, M.; Andersson, M. Photothermal Properties of Solid-Supported Gold Nanorods. *Nano Lett* **2024**, *24* (40), 12529–12535. https://doi.org/10.1021/acs.nanolett.4c03472.

(96) Arciola, C. R.; Campoccia, D.; Speziale, P.; Montanaro, L.; Costerton, J. W. Biofilm Formation in Staphylococcus Implant Infections. A Review of Molecular Mechanisms and Implications for Biofilm-Resistant Materials. *Biomaterials* **2012**, *33* (26), 5967–5982. https://doi.org/10.1016/j.biomaterials.2012.05.031.

(97) Nicolle, L. E. Catheter Associated Urinary Tract Infections. *Antimicrob Resist Infect Control* **2014**, *3* (1), 23. https://doi.org/10.1186/2047-2994-3-23.

(98) Ducret, A.; Quardokus, E. M.; Brun, Y. V. MicrobeJ, a Tool for High Throughput Bacterial Cell Detection and Quantitative Analysis. *Nat Microbiol* **2016**, *1* (7), 16077. https://doi.org/10.1038/nmicrobiol.2016.77.

(99) Jana, N. R. Gram-Scale Synthesis of Soluble, near-Monodisperse Gold Nanorods and Other Anisotropic Nanoparticles. *Small* **2005**, *1* (8–9), 875–882. https://doi.org/10.1002/smll.200500014.

(100) Park, K.; Drummy, L. F.; Wadams, R. C.; Koerner, H.; Nepal, D.; Fabris, L.; Vaia, R. A. Growth Mechanism of Gold Nanorods. *Chemistry of Materials* **2013**, *25* (4), 555–563. https://doi.org/10.1021/cm303659q.

(101) Liu, M.; Guyot-Sionnest, P. Mechanism of Silver(I)-Assisted Growth of Gold Nanorods and Bipyramids. *Journal of Physical Chemistry B* **2005**, *109* (47), 22192–22200. https://doi.org/10.1021/jp054808n.

(102) Uusitalo, M.; Eriksson, G.; Hulander, M.; Andersson, M. Gold Nanorods as Photothermal Antibacterial Materials. *ACS Appl Nano Mater* **2025**, *8* (7), 3661–3670. https://doi.org/10.1021/acsanm.5c00324.

(103) Touloukian, Y. S.; Kirby, Y. B.; Taylor, R. E.; Desai, P. D. Thermal Expansion: Metallic Elements and Alloys. In *Thermophysical Properties of Matter*; IFI/Plenum: New York, 1975; Vol. 12.

(104) Wang, Y.; Dellago, C. Structural and Morphological Transitions in Gold Nanorods: A Computer Simulation Study. *Journal of Physical Chemistry B* **2003**, *107* (35), 9214–9219. https://doi.org/10.1021/jp034445w.

(105) Johnson, P. B.; Christy, R. W. Optical Constants of Transition Metals: Ti, V, Cr, Mn, Fe, Co, Ni, and Pd. *Phys Rev B* **1974**, *9* (12), 5056–5070.

(106) Habteyes, T. G.; Dhuey, S.; Wood, E.; Gargas, D.; Cabrini, S.; Schuck, P. J.; Alivisatos, A. P.; Leone, S. R. Metallic Adhesion Layer Induced Plasmon Damping and Molecular Linker as a Nondamping Alternative. *ACS Nano* **2012**, *6* (6), 5702–5709. https://doi.org/10.1021/nn301885u.

(107) Blomstrand, E.; Posch, E.; Stepulane, A.; Rajasekharan, A. K.; Andersson, M. Antibacterial and Hemolytic Activity of Antimicrobial Hydrogels Utilizing Immobilized

Antimicrobial Peptides. *Int J Mol Sci* **2024**, *25* (8), 4200. https://doi.org/10.3390/ijms25084200.

(108) Huang, X.; Xu, L.; Yu, X.; Li, Y.; Huang, Z.; Xu, R.; Zeng, W.; Zhang, Z.; Li, W.; Deng, F. Near-Infrared Light-Responsive Multifunctional Hydrogel Releasing Peptide-Functionalized Gold Nanorods Sequentially for Diabetic Wound Healing. *J Colloid Interface Sci* **2023**, *639*, 369–384. https://doi.org/10.1016/j.jcis.2023.02.078.

(109) Sankari, S. S.; Dahms, H. U.; Tsai, M. F.; Lo, Y. L.; Wang, L. F. Comparative Study of an Antimicrobial Peptide and a Neuropeptide Conjugated with Gold Nanorods for the Targeted Photothermal Killing of Bacteria. *Colloids Surf B Biointerfaces* **2021**, *208*, 112117. https://doi.org/10.1016/j.colsurfb.2021.112117.

(110) Te Winkel, J. D.; Gray, D. A.; Seistrup, K. H.; Hamoen, L. W.; Strahl, H. Analysis of Antimicrobial-Triggered Membrane Depolarization Using Voltage Sensitive Dyes. *Front Cell Dev Biol* **2016**, *4*. https://doi.org/10.3389/fcell.2016.00029.

(111) Hover, B. M.; Kim, S.-H.; Katz, M.; Charlop-Powers, Z.; Owen, J. G.; Ternei, M. A.; Maniko, J.; Estrela, A. B.; Molina, H.; Park, S.; Perlin, D. S.; Brady, S. F. Culture-Independent Discovery of the Malacidins as Calcium-Dependent Antibiotics with Activity against Multidrug-Resistant Gram-Positive Pathogens. *Nat Microbiol* **2018**, *3* (4), 415–422. https://doi.org/10.1038/s41564-018-0110-1.

(112) Pogliano, J.; Pogliano, N.; Silverman, J. A. Daptomycin-Mediated Reorganization of Membrane Architecture Causes Mislocalization of Essential Cell Division Proteins. *J Bacteriol* **2012**, *194* (17), 4494–4504. https://doi.org/10.1128/JB.00011-12.

(113) Malmsten, M.; Kasetty, G.; Pasupuleti, M.; Alenfall, J.; Schmidtchen, A. Highly Selective End-Tagged Antimicrobial Peptides Derived from PRELP. *PLoS One* **2011**, *6* (1), e16400. https://doi.org/10.1371/journal.pone.0016400.

(114) Schäfer, A.-B.; Steenhuis, M.; Jim, K. K.; Neef, J.; O'Keefe, S.; Whitehead, R. C.; Swanton, E.; Wang, B.; Halbedel, S.; High, S.; van Dijl, J. M.; Luirink, J.; Wenzel, M. Dual Action of Eeyarestatin 24 on Sec-Dependent Protein Secretion and Bacterial DNA. *ACS Infect Dis* **2023**, *9* (2), 253–269. https://doi.org/10.1021/acsinfecdis.2c00404.

(115) Özsan, Ç.; Schäfer, A.-B.; Akhir, A.; Aning, O. A.; Fulgencio, S.; Maitra, R.; Rani, R.; Saxena, D.; Westerlund, F.; Chopra, S.; Wenzel, M.; Frei, A. A Platinum Butterfly Effect: Small Changes Turn an Anticancer Drug into a Non-Toxic Metalloantibiotic with In Vivo Efficacy. *bioRxiv* **2025**, 657029. https://doi.org/10.1101/2025.05.30.657029.